Fragmentation of 400 MeV/u ^{12}C on a thin graphite target

Fragmentierung von 400 MeV/u ^{12}C an einem dünnen Graphittarget
Zur Erlangung des Grades eines Doktors der Naturwissenschaften (Dr. rer. nat.)
vom Fachbereich Physik genehmigte Dissertation von Christoph Schuy Dipl.-Phys aus Hadamar
1. Gutachten: Prof. Dr. Marco Durante
2. Gutachten: Prof. Dr. Joachim Enders
Tag der Einreichung: 12.02.2014, Tag der Prüfung: 19.05.2014
Darmstadt 2015 — D 17

TECHNISCHE
UNIVERSITÄT
DARMSTADT

Fachbereich Physik
Institut für Festkörperphysik
Gesellschaft für Schwerionenforschung

Fragmentation of 400 MeV/u ^{12}C on a thin graphite target
Fragmentierung von 400 MeV/u ^{12}C an einem dünnen Graphittarget

Vom Fachbereich Physik genehmigte Dissertation von Christoph Schuy Dipl.-Phys aus Hadamar

1. Gutachten: Prof. Dr. Marco Durante
2. Gutachten: Prof. Dr. Joachim Enders

Tag der Einreichung: 12.02.2014
Tag der Prüfung: 19.05.2014

Darmstadt — D 17

Erklärung zur Dissertation

Hiermit versichere ich, die vorliegende Dissertation ohne Hilfe Dritter nur mit den angegebenen Quellen und Hilfsmitteln angefertigt zu haben. Alle Stellen, die aus Quellen entnommen wurden, sind als solche kenntlich gemacht. Diese Arbeit hat in gleicher oder ähnlicher Form noch keiner Prüfungsbehörde vorgelegen.

Darmstadt, den 11.02.2014

(Christoph Schuy)

Abstract

Detailed understanding of high energetic heavy ions interacting with matter is of great interest in basic research and applied physics especially in radiotherapy and space radioprotection. Radiotherapy with carbon ions showed great success especially in the treatment of deep seated tumors due to the favorable depth-dose profile and increased biological effectiveness compared to photons or protons. Due to nuclear interactions between the primary beam and the patient's body, usually only 50% of the carbon ions will reach the target location. Thus, a detailed knowledge of the changes in the radiation field is required for delivering a successful treatment. The radiation environment in space is composed of high energy charged particles and can lead to serious health risks for astronauts. The assessment and mitigation of radiation-induced health complications cannot be accomplished without a good understanding of the interaction of the mixed radiation field with e.g. the hull of the spaceship or lunar soil.

In this work the fragmentation of 400 MeV/u ^{12}C on a thin graphite target was investigated. The resulting angular yield distributions and differential energy spectra of charged and uncharged particles are presented and compared to two different Monte Carlo codes (PHITS and GEANT4).

Zusammenfassung

In der physikalischen Grundlagenforschung sowie der angewandten Physik insbesondere im Bereich der Strahlentherapie und des Strahlenschutzes ist das detaillierte Verständnis der Interaktion hochenergetischer Schwerionen mit Materie von großem Interesse. Strahlentherapie mit Kohlenstoff zeigte vielversprechende Ergebnisse im klinischen Einsatz. Vor allem bei tiefsitzenden Tumoren im Kopf und Hals Bereich wirkt sich das inverse Tiefendosisprofil und die erhöhte biologische Wirksamkeit im Vergleich zu Photonen und Protonen positiv aus. Auf Grund von Wechselwirkungsprozessen im Körper des Patienten erreichen üblicherweise nur ca. 50% der ursprünglichen Kohlenstoffionen das geplante Ziel. Demzufolge ist für eine erfolgreiche Behandlung detailliertes Wissen über die Änderung des Strahlungsfeldes durch Interaktion von Kohlenstoff mit Materie erforderlich.

Weiterhin ist die aus hochenergetischen geladenen Teilchen bestehende kosmische Strahlung ein ernstzunehmendes Gesundheitsrisiko für Astronauten. Eine Abschätzung der Gesundheitsrisiken sowie eine Verminderung jener lassen sich nur über die genaue Kenntnis des Strahlungsfeldes nach Interaktion, z.B. mit der Hülle eines Raumschiffes, durchführen.

Diese Arbeit untersucht die Fragmentierung von 400 MeV/u ^{12}C an einem dünnen Graphittarget. Die gemessenen Winkelverteilungen der Fragmente, deren Energiespektren, sowie ein Vergleich mit den gängigen Monte Carlo Codes (PHITS und GEANT4) werden präsentiert.

Contents

List of Tables

List of Figures

Motivation

A detailed knowledge of the transport of high energy ions through matter is of great interest in basic research and applied physics especially in radiotherapy and space radiation protection.

Radiotherapy is among the most frequently used treatment modalities. In particular, the therapy with carbon ions showed tremendous success for deep seated tumors located in the head and neck region [73]. The main goal of radiotherapy is to deliver a planned dose to a certain area, effectively killing all cancerous cells while sparing the surrounding normal tissue or possible radiation sensitive organs close to the tumor site. One of the major advantages of using heavy charged particles in cancer treatment is their favorable depth-dose profile ("Bragg curve", shown in figure 1.5) and, especially for carbon ions, their increased Relative Biological Effectiveness (RBE) compared to standard photons or protons treatment. Furthermore, the carbon beam offers an optimal compromise between the enhanced biological effect in the tumor region and the dose deposited at the entrance channel due to the RBE dependency on the Linear Energy Transfer (LET), defined as the energy deposited in matter by a slowing down particle per path unit. Depending on the specific clinical case, only 50% of the primary ions will reach deep seated tumors because of the frequent interactions with the healthy tissue in front of the tumor location. This implies that the quality of the radiation field changes continuously while passing through a patients body and must be taken into account for achieving a successful treatment. Typical Treatment Planning Systems (TPS), like TRiP98 [44] developed at GSI, are based on experimental data and unidimensional physical models to estimate the radiation field changes and thus to optimize the dose distribution for each patient applying the Local Effect Model (LEM) [18] to calculate an RBE-weighted dose. The measurement of new data like total charge-changing cross sections or angular distributions of secondary fragments allow a more precise assessment of the radiation field along the tumor path and thus improve the accuracy of the treatment planning. Recent interest in Monte Carlo-based treatment planning to simulate directly the full physical behavior of an ion beam passing through tissue-like materials show significant deviations compared to experiments [8]. Therefore, new data for verification and benchmarking of existing physical models are needed.

Even before entering the patients body, the beam composition might be altered significantly depending on the delivery system. A fully passive modality with scattering devices, modulators and range-shifters, relies on the interaction of charged particles with matter to shape the monoenergetic primary beam in such a way as to deliver a planned optimized dose. On the other hand, a fully active system uses magnetic scanning and fast energy changes from the accelerator to complete the treatment. The creation of secondary charged and uncharged fragments will be heavily influenced by the delivery technique [41]. Thus, a correct understanding of the therapeutic beam interactions with different target materials present in the delivery line is a key point for comparing and optimizing different treatment modalities.

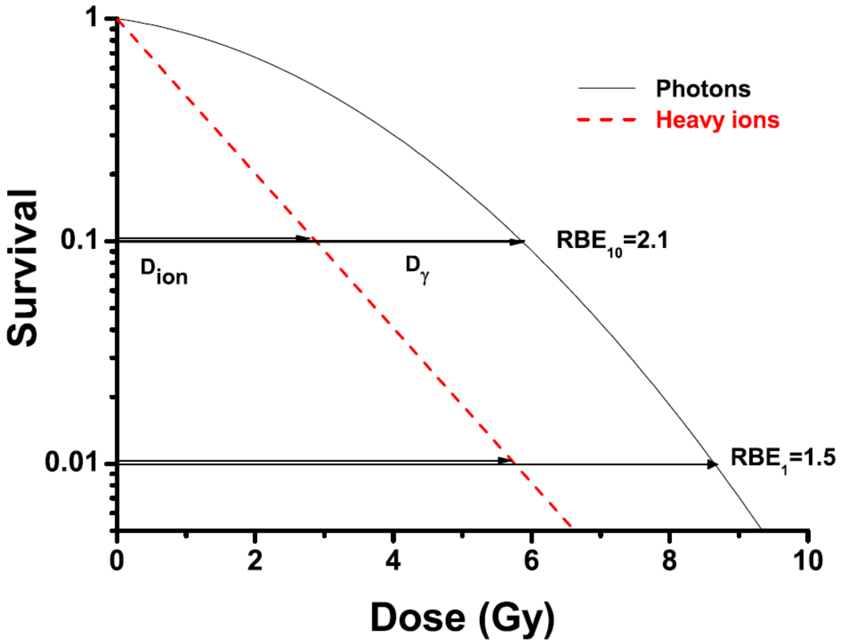

Determination of the Relative Biological Effectivness (RBE) using cell inactivation curves. The RBE is defined as the ratio of X-ray to ion dose to induce the same biological effect. The figure is taken from [71].

While the main goal of cancer therapy is using radiation for killing the malignant cells, space radiation protection aims at the direct opposite, assessing the radiation induced health risks in space missions and improving the prevention of unacceptable exposure to high radiation doses. The protection from the radiation environment in space, which consists of high energy protons from Solar Particle Events (SPE), fast heavy ions coming from Galactic Cosmic Rays (GCR) and trapped particles in the Earth magnetic field, is one of the most serious challenges its exploration [17]. The composition of GCR, which dominates the radiation environment in deep space, is well known [76]. It covers an energy range up to 10^{20} eV and consists mainly of protons, helium and a low amount of heavier particles. Since the effect of charged particles on the human body is, as a first approximation, proportional to the square of their charge even a small yield of heavy ions represents a serious health risk for the crew members. Estimates of an astronauts risk for radiation induced cancer and noncancer diseases during different mission scenarios show high uncertainties due to the radiation quality changes caused by e.g. the interaction of fast charged particles with the spacecraft hull.

Even if the experimental characterization of all possible projectile-target combinations in the energy range of interest is not feasible, some sets of measurements are needed for model development and benchmarking of the theoretical models. Therefore, the National Aeronautics and Space Administration (NASA) concluded recently that experimental fragmentation data for ^{12}C ions at intermediate energies between 100 MeV/u and 500 MeV/u are missing [55]. A detailed knowledge of the space radiation environment in conjunction with accurate measurements of the radiation quality changes induced by the interaction with matter are needed to properly estimate the health risk as well as to find and optimize countermeasures such as appropriate shielding.

The aim of this work is to investigate the fragmentation of 400 MeV/u ^{12}C impinging on a thin graphite target. Yield, angular distributions and kinetic energy spectra of all produced charged and uncharged particles are presented. The thesis is subdivided in four chapters. Chapter 1 gives a short introduction to the physical processes relevant for the measurements. Chapter 2 presents the experimental setup and analysis techniques. The results are discussed in chapter 3 while the conclusions and future outlook are reported in chapter 4. Additional information on the used detectors, Monte Carlo simulations and error calculations can be found in the Appendixes A, B, C and D.

1 Radiation interaction with matter

The aim of the present chapter is to give an overview of all relevant physical processes involved in the investigation of nuclear fragmentation. The understanding of certain types of radiation interaction with matter is crucial for the detection of fragmentation products and thus for the design of experiments aiming to characterize this phenomenon. A detailed description of the processes mentioned here can be found for example in [43] and [47]. When discussing the interaction with matter, radiation has to be subdivided in two distinct kinds: charged and uncharged. The former, like heavy ions, in general interact continuously with the electric field of the absorber, changing its properties with each reaction. Uncharged radiation, like photons and neutrons, is not affected by the Coulomb force and can travel a long way in most materials without undergoing any interaction. When a reaction occurs, the physical properties of the radiation are altered radically. One of the basic parameters to describe interaction processes is the cross section σ. In the differential form it is defined as

$$\frac{d\sigma}{d\Omega}(E,\Omega) = \frac{1}{F}\frac{dN_i}{d\Omega}\ [b\ sr^{-1}] \tag{1.1}$$

with F the number of incident particles, N_i the average number of particles which undergo an interaction and Ω the solid angle with respect to the point of interaction. Figuratively, the cross section $d\sigma/d\Omega$ represents the fraction of particles impinging on the target which interact with the area $d\sigma$ and are measured at the solid angle $d\Omega$.

The total cross section for a given interaction to occur, is defined as

$$\sigma(E) = \int d\Omega \frac{d\sigma}{d\Omega} \tag{1.2}$$

, has the dimension of an area and its unit is the barn:

$$1\ barn = 10^{-28}\ m^2 \tag{1.3}$$

1.1 Neutrons

Neutrons, as uncharged particles, are not affected by the Coulomb field of the absorber atom and interact primarily with the nuclei of the medium via the strong force. The low range of the latter reduces the interaction frequency and thus increases the neutron penetration through matter. The probability of each type of interaction mechanism depends on the neutron energy. Fast neutrons (energy ranging from hundreds of keV to hundreds of MeV) mainly interact with the target nuclei via elastic or, if their energy is sufficiently high to excite the target nuclei, via inelastic scattering. The many-body-problem of a fast neutron traversing a thick absorber can be described as several scattering processes of two free particles [34]: each step lowers the energy of the neutron and slows it down according to a process called moderation. The best moderators are proton-rich or light nuclei materials because, having a mass similar to neutrons, they offer the highest energy transfer in a single reaction. Other processes, as neutron capture $n + (A, Z) = y + (A + 1, Z)$, where the neutron is absorbed by the target nucleus and charged particles are emitted, are possible for neutron energies below some keV and become predominant if the neutron is in thermal equilibrium with the absorber atoms.

1.2 Photons

Due the production of high energy photons during the occurrence of nuclear fragmentation and their usefulness especially for time-of-flight measurements the energy loss mechanisms of photons are of special interest for nuclear fragmentation experiments. The three main energy loss mechanisms for photons that lead to their partial or total energy transfer to a bound electron of the target atom are the photoelectric absorption, the Compton scattering and the pair production. The occurrence of the different interaction mechanisms with respect to the absorber atomic number and the energy of the impinging photons is illustrated in figure 1.1. Photon radiation is typically categorized by its origin. Photons emitted by the rearrangement of the electron shells of an atom are typically referred to as X-rays while photons emitted by energy level transitions of the nucleus itself are named γ-rays.

Photoelectric absorption

In photoelectric absorption, a photon interacts with a bound electron of the absorber nucleus and transfers its full energy (figure 1.2). This leads to the ejection of a so called photoelectron with an energy defined as

$$E_e = h\upsilon - E_b \tag{1.4}$$

where E_b is the binding energy of the electron in its original shell, h the Planck constant and υ the frequency of the impinging photon. Due to the loss of an electron, the atom is left in an ionized state and deexcites either by the capture of a free electron or by the rearrangement of the shell electrons. In these processes further photons or electrons might be emitted.

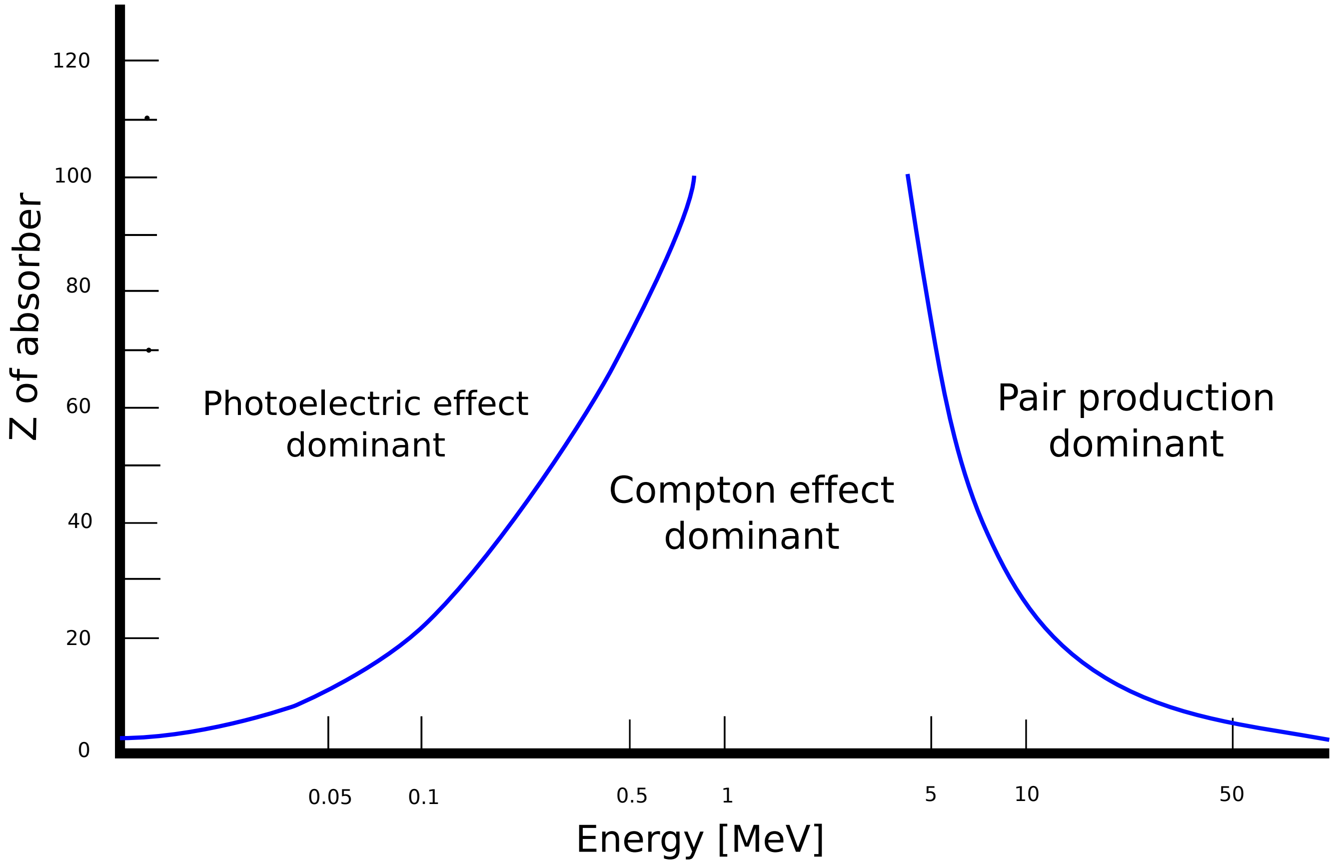

Figure 1.1.: Probability of the three main interaction mechanisms of photons with matter (reproduced from [43]) as a function of their energy. At low photon energies and for absorbers with high atomic numbers photoelectric absorption is predominant. Intermediate energies up to some MeV are dominated by Compton scattering. At higher energies the probability for pair production increases for a given photon energy approximately with the square of the atomic number of the absorber and for a given absorber it increases with increasing photon energy.

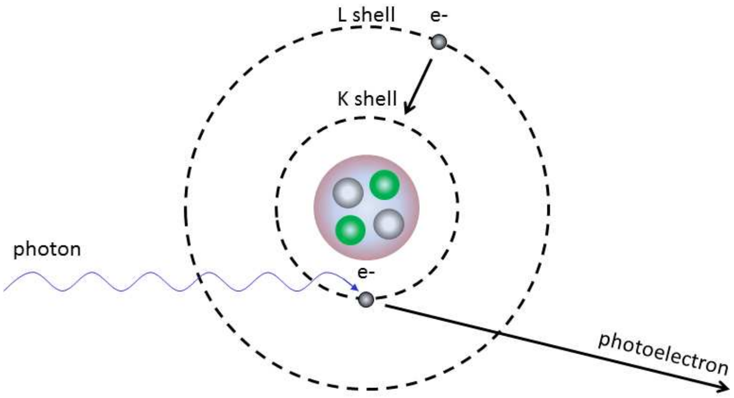

Figure 1.2.: Schematic of the photoelectric effect. The impinging photon transfers its energy to a bound electron of the absorber. The so called photoelectron is ejected by the atom with the energy of the impinging photon minus the binding energy.

The probability of photoelectric absorption, τ, can be approximated to

$$\tau \propto \frac{Z^n}{(hv)^3} \tag{1.5}$$

with Z being the atomic number of the target material, n a number varying between 4 and 5 and $(hv)^3$ the energy to the power of 3 of the impinging photon. Photoelectric absorption is the predominant energy loss process for low energetic photons and high-Z absorbers.

Compton scattering

The process of a photon scattering on a bound electron and transferring part of its energy to the latter is known as Compton scattering (figure 1.3). All scattering angles are possible and therefore the energy transferred to the electron can vary up to a large fraction of the initial photon energy.

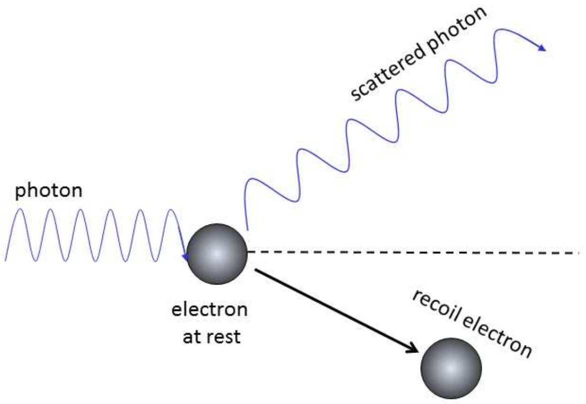

Figure 1.3.: Scheme of the Compton scattering mechanism. The impinging photon is scattered inelastically on an electron and transfers parts of its energy, depending on the scattering angle.

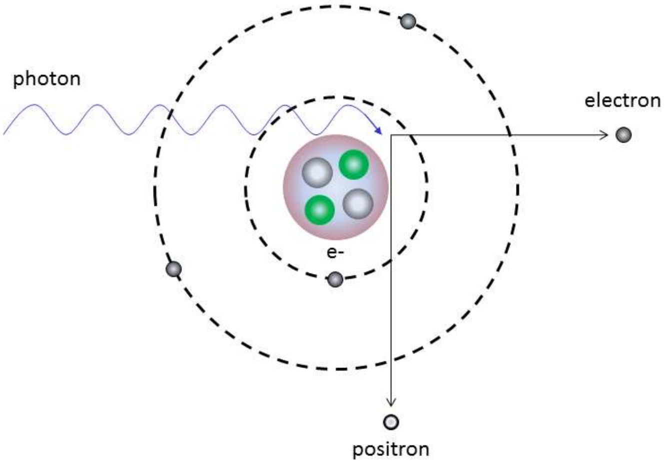

Figure 1.4.: Scheme of the pair production process. A photon of sufficient energy (E≥1.022 MeV) impinging on a nucleus vanishes and produce an electron-positron pair. The positron will later annihilate with an electron by emitting two 511 keV photons at opposite directions to each other.

Pair production

A photon passing the Coulomb field of a nucleus can undergo pair production if its energy exceeds two times the rest mass of the electron (1.022 MeV). The photon vanishes and is replaced by a newly created electron-positron pair, whose energy is defined as

$$E_{e+} + E_{e-} = h\nu - 1.022\,MeV \tag{1.6}$$

The probability κ related to the pair production process for a given absorber increases with increasing photon energy and for a given photon energy increases approximately with the Z^2 of the absorbing material (figure 1.1).

1.3 Charged particles

When an ion traverses a medium, it continuously interacts with the electrons of the absorber atoms via Coulomb interactions. The energy transfer can lead to excitation (a bound electron is raised to a higher shell), ionization (a bound electron is removed completely) of the absorber atoms or, close to the stopping point of the ion, to changes in the charge state of the ion itself [25]. Electrons receiving enough kinetic energy to cause further ionization are called δ-rays.

Specific energy loss

The amount of energy loss dE per path length dx is called linear stopping power S and is defined as

$$S = -\frac{dE}{dx} \tag{1.7}$$

The quantum mechanical description of S is known as the Bethe-Bloch formula [43]:

$$-\frac{dE}{dx} = 2\pi N_a r_e^2 m_e c^2 \rho \frac{Z}{A}\frac{z^2}{\beta^2}\left[ln\left(\frac{2m_e\gamma^2 v^2 W_{max}}{I^2}\right) - 2\beta^2\right] \tag{1.8}$$

with

N_a	Avogadro number
r_e	electron radius
m_e	electron mass
c	speed of light
ρ	absorber density
Z	absorber charge
A	absorber atomic weight
z	incident ion charge
β	v/c
γ	$\frac{1}{\sqrt{1-\beta^2}}$
I	mean excitation potential
W_{max}	maximum energy transfer per collision

For particles with $m_{particle} \gg m_e$, the quantity W_{max} can be approximated to

$$W_{max} = 2m_e c^2 \beta^2 \gamma^2 \tag{1.9}$$

As shown in equation (1.8) the Bethe-Bloch formula varies with $1/\beta^2$ for nonrelativistic particles and decreases with increasing velocity. For different particle species with the same kinetic energy, the Bethe-Bloch formula can be simplified to

$$-\frac{dE}{dx} \propto z^2 \tag{1.10}$$

A common way to present the energy loss of radiation in matter is by plotting it versus the penetration depth in the so called Bragg curve. An example for the energy loss of carbon ions, protons and photons is shown in figure 1.5. In radiotherapy, the absorbed dose D is commonly used instead of the stopping power as a measure of the energy deposited in a target medium per unit mass. It is defined as

$$D = \frac{dE}{dm} = \frac{1}{\rho}\frac{dE}{dV} \tag{1.11}$$

with m and V the mass and volume of the absorber. The fast charged particle traversing the absorbing medium interacts mainly with the electrons and for each interaction only a small energy fraction is transferred (the maximum amount per collision is $\approx 1/500$ of the ion kinetic energy [43]). As described by equation (1.8), the interaction frequency increases with decreasing ion energy. At the end of their path the low energetic ions start picking up electrons, resulting in a sharp fall off. The region where the energy loss reaches its highest value is called Bragg peak.

The energy loss behavior for photons is plotted too in figure 1.5 for comparison; its trend can be described with an exponential decay. The region of highest energy transfer is shifted away from the surface to the inside of the absorbing medium due to a build-up effect of the created electrons. Furthermore, figure 1.5 illustrates several other important characteristics typical of charged particles passing through matter, like the fragmentation tail behind the Bragg peak for carbon ions or the finite width of the Bragg peak region. The energy loss of charged particles is a statistical process and hence slightly different for each single interaction (energy straggling). This is translated into a broadening of the Bragg peak which is more prominent for lighter ions and at lower energies [65].

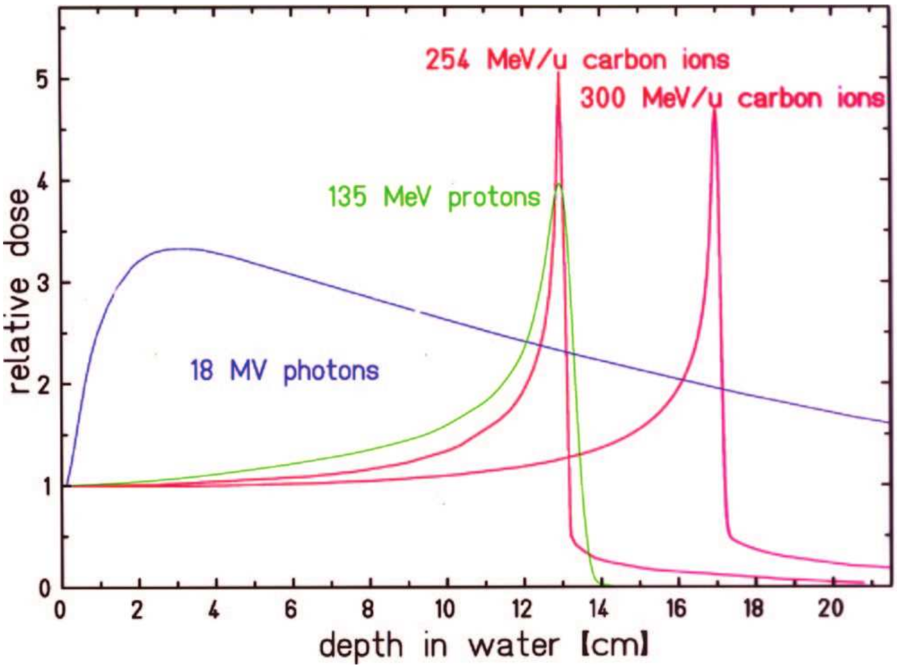

Figure 1.5.: Comparison of the relative energy loss (Bragg curve) of 18 MeV photons, 135 MeV protons, 254 MeV/u and 300 MeV/u carbon ions in water [81] .

1.4 Nuclear fragmentation

Fragmentation, i.e. the creation of new, lighter particles due to nucleus—nucleus collision, can alter the composition of the radiation field inside the absorber and influences further interaction processes. The basic parameter for describing nucleus—nucleus collisions is the impact factor b which represents the distance between the center of mass of the impinging projectile nucleus and the stationary absorber nucleus (figure 1.6). Depending on the value of b, nucleus-nucleus collisions can be subdivided in two different kinds. Small impact factors will lead to more direct collisions while large impact factors can lead to peripheral collisions and electromagnetic dissociation. For light systems ($Z \approx\leq 56$) and intermediate energies ($E \approx\leq$ some GeV/u)

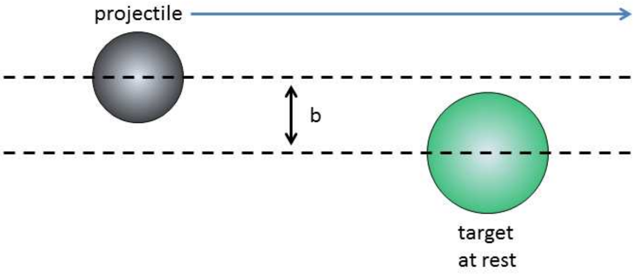

Figure 1.6.: Geometrical definition of the impact factor b as the distance between the projectile and the target center of mass. A value of b is considered small if a geometrical overlap exists.

typical in ion radiotherapy and space radioprotection it has been shown that electromagnetic dissociation only plays a minor role [24] and thus will be covered only briefly in this work.

The process of nuclear fragmentation can be described geometrically by the abrasion-ablation model [9], which provides an accurate prediction of existing experimental data and has been used as a basis for developing new fragmentation models [46]. In a first step (abrasion stage) part of the projectile and/or the target are sheared off and a prefragment is created. In the second step (ablation-stage) the highly excited prefragment is either thermalized or disintegrates emitting photons, neutrons or charged particles. A schematic of the model dynamics is shown in figure 1.7.

Abrasion stage

The projectile nucleus P collides with the stationary absorber nucleus T and the overlapping portion, defined by the impact factor, is sheared off and forms the partipant. The remaining pieces of P and T are called prefragments and are assumed to continue with precollision velocity. A momentum transfer from the projectile nucleus P_P occurs in both longitudinal and transverse direction resulting in the momentum P_{PF} of the prefragment and of the target nucleus P_T, which depend on the projectile energy, impact parameter and the combination of projectile and target.

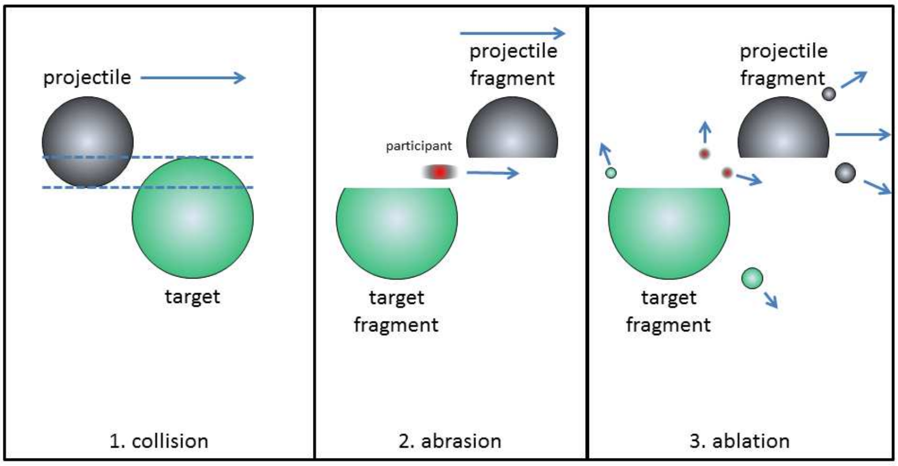

Figure 1.7.: Scheme of the ablation-abration model. A projectile nucleus P collides with the stationary target nucleus T. Parts of the projectile and/or target nucleus are sheared off and an exited prefragment is created. The prefragment is then either thermalized or collapses by emitting photons or particles.

The prefragments are usually left in an excited state due to the gain in surface energy after the removal of the overlap volume. The participant gains the translational energy loss as heat.

Ablation stage

The excited prefragments will either lose their excessive energy by thermalizing or by the evaporation of nucleons until reaching their ground state. This means that a fragment with a given charge can be created by different pathways, but thermalization is the more probable case in light systems [57].

Electromagnetic dissociation

For larger impact factors, where no nuclear interaction is possible, electromagnetic dissociation can take place. It is described by the two step deflection-excitation model shown in figure 1.8. The projectile nucleus is deflected by the target nucleus electric field and excited by the exchange of virtual photons. The excited projectile can deexcite emitting either photons or particles.

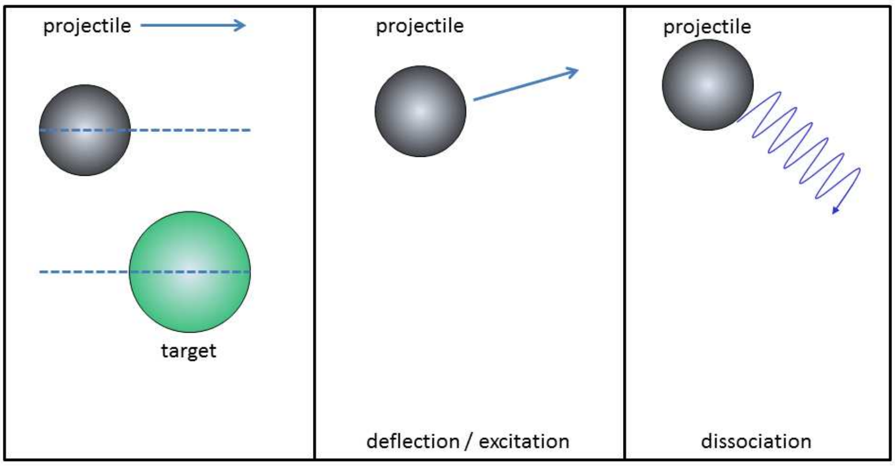

Figure 1.8.: Scheme of the two step electromagnetic dissociation process.

2 Setup and experimental technique

Nuclear fragmentation of a 400 MeV/u $^{12}C^{6+}$ beam impinging on a thin graphite target was investigated in 2011 and 2012 at the experimental site Cave A in the GSI accelerator facility (Darmstadt, Germany). The aim of the experiment was to obtain angular yield distributions of charged and uncharged fragmentation products as well as their kinetic energy spectra. Information on the measured angles and target characteristics are reported in table 2.1.

The experimental setup and techniques are described in this chapter while the measurement results are discussed in chapter 3.

2.1 Experimental setup

A scheme of the experimental setup is shown in figure 2.1.

Once exiting the vacuum window (Material: Aluminum, Thickness: 100μm), the particles traverse a thin plastic scintillator (further referred to as START) before impinging on the target. The produced fragments are detected by a telescope consisting of a thick plastic scintillator (further referred to as VETO) and a thick Barium Fluoride crystal scintillator (further referred to as BaF_2). A detailed description of the detector properties is reported in section 2.1.1. The analog signals of the detectors are split to form a TIME- and an ENERGY-line, as shown in figure 2.2.

The ENERGY-line is directly acquired using Charge-to-Digital converter (QDC) modules whereas the TIME-line is used for creating triggering- and gating-signals as well as for collecting time information. The detector alignment on target center was accomplished with a laser cross and all distances were measured with a standard measuring tape. An extensive discussion on the electronics and data acquisition is reported in section 2.2. The recorded files are evaluated using the ROOT data analysis framework [10]. The analysis methodology is presented in section 2.3.

Measured angles [degrees]	0, 2(1.3), 4(0.7), 6(0.4), 8(0.4), 15(0.2)
Target material	graphite
Target areal density [g/cm^2]	1.84±0.002
Target thickness [cm]	0.5±0.01

Table 2.1.: List of the target characteristics and of the angles at which the yield and kinetic energy of the fragments were measured.

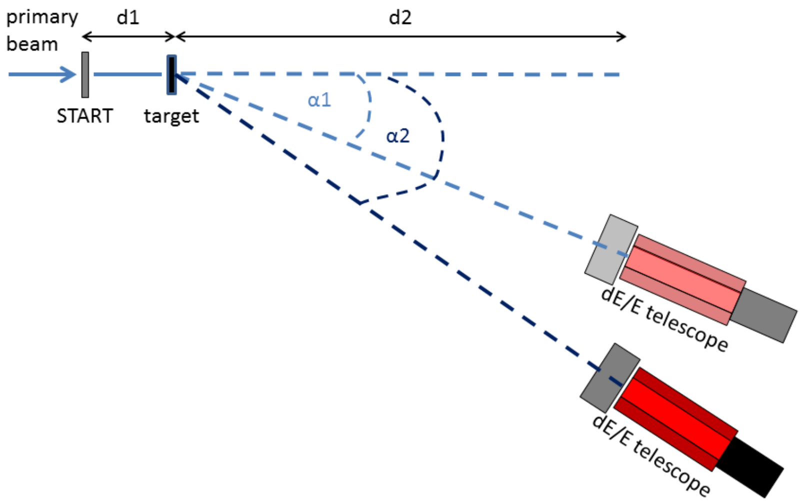

Figure 2.1.: Scheme of the experimental setup. The distances between START and target (further referred to as d1) and between target and BaF_2 (further referred to as d2) positioned at 0 degrees were kept constant at 4±0.1 cm and 224±0.1 cm, respectively. Information on the measured angles and target characteristics are reported in table 2.1.

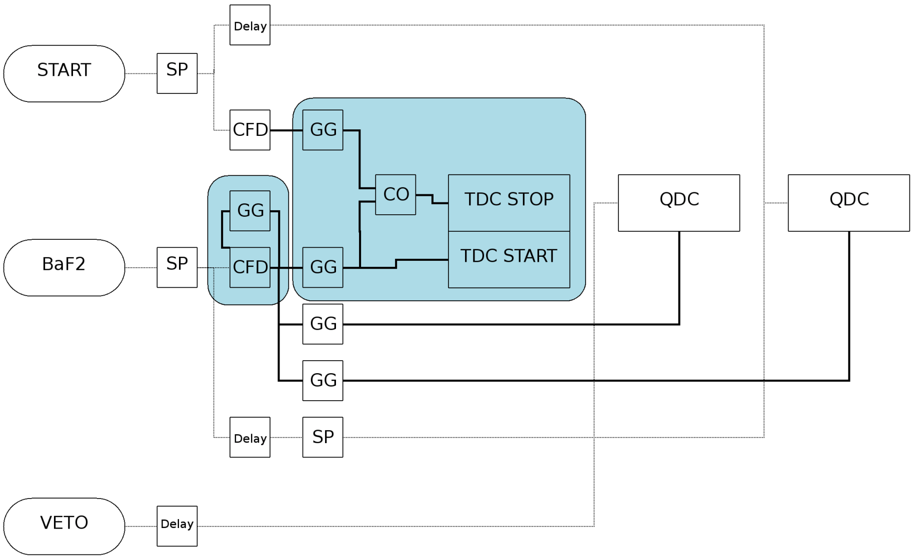

Figure 2.2.: Simplified scheme of the electronics setup. Dotted lines show the flow of the analog anode signals while solid lines are related to the logic pulses. The colored areas mark the most critical points in the setup namely the gating of the constant fraction discriminator and the inverse time-of-flight logic.

The described setup was, up to now, mainly used for measuring the fragmentation of carbon ions with therapeutic energies ($90 \leq E \leq 400$ MeV/u) impinging on thick targets [31, 35, 67]. The experimental methodology presented in this chapter has the following main disadvantages:

- lack of real-time monitoring of the primary beam position;
- limited single-ion-counting capabilities of the START detector;
- limited rate of the CAMAC-based Data AQuisition (DAQ);
- limited to leading-charge analysis for events with high multiplicity, where several particles hit the detector telescope at once and can not be fully separated.

A detailed description of the setup limitations together with planned and already applied solutions is the topic of appendix C.

2.1.1 Detectors

START and VETO share the same general structure and detection principles and differ only in active area, thickness and intended use of the output signals. Both detectors are made of BC400, a general purpose organic scintillation material which offers fast rise time (≈ 0.9 ns) required to obtain precise timing information and short decay time (≈ 2.4 ns) for fast single-ion-counting and low dead time. Further details on the BC400 material are given in appendix A.1. The scintillation material of both detectors is glued to a plastic light guide to maximize the illumination of the EMI 9954 QB photomultiplier (figure 2.3) .

The detectors are wrapped in an aluminum foil layer to reflect the scintillation light leaving the surface and to further increase the light output. The active area of the detectors, the light guide and the interface to the multiplier are covered with a layer of thin black tape to shield from artificial light sources and reduce the background noise.

START

START is 2 mm thick and offers an active detection area of 10x10 cm^2. Its two main purposes are to count the amount of primary ions impinging on the target and generate timing signals for time-of-flight measurements. The thickness was chosen as a compromise for maximizing the light output for a variety of particle species in the energy range of interest and for minimizing the fragmentation of the primary ions inside the detector itself.

VETO

VETO is 9 mm thick and hexagonally shaped (inscribed radius 5.4 cm) to cover the complete surface of the BaF_2 (figure. 2.4). Its role is to discriminate between charged and uncharged

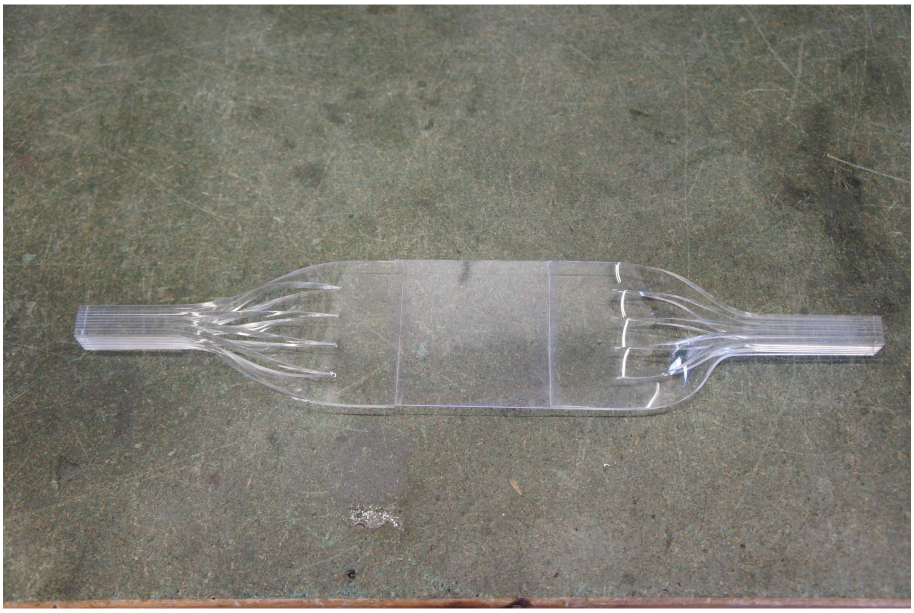

Figure 2.3.: Example of two light guides attached to a rectangular plastic scintillator. The light emitted by the scintillator travels through the spiral arms of the light guide and to its cube shaped end in order to cover as much area of the photomultiplier tube as possible.

particles as well as to separate different ion species. An example of the charge discrimination abilities of the VETO is shown in figure 2.6.

BaF_2

BaF_2 consists of a 14 cm long, hexagonally shaped, Barium Fluoride crystal with an inscribed radius of 4.5 cm directly coupled to a Thorn EMI 9821 QB photomultiplier. Due to the slight hygroscopic nature of the crystal, its mechanical fragility and to shield it from electrons, the crystal is covered by a 1 mm thick aluminum case. A thin layer of teflon acts as a reflector for the scintillation light escaping the crystal.

Barium Fluoride is an inorganic, dense ($\rho = 4.88$ g cm^{-3}) scintillation material with two emission lines: a short component with a decay time of $\approx$ 0.6 ns mainly excited by electrons and photons, and a long component with a decay time of $\approx$ 630 ns mainly excited by charged particles [51]. Neutrons create hadronic showers of light ions (mainly protons) inside the detector material and therefore can be measured too. The neutron detection efficiency of this crystal up to 50 MeV/u is reported in [45]. Neutron efficiency measurements acquired with the described setup for a wide energy range are reported in [31]. More details on the neutron detection efficiency are presented in 2.4.

The short and long component can be exploited to discriminate different particle species using pulse-shape-analysis [56]. Due to its sub nanosecond timing response, the high stopping power

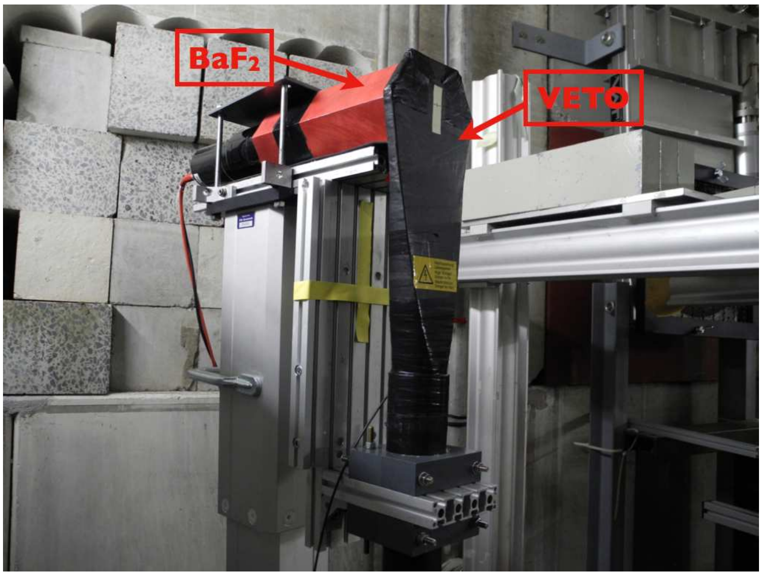

Figure 2.4.: $\triangle E/E$ - telescope consisting of a 9 mm plastic scintillator (VETO) and a 14 cm BaF_2 crystal detector.

for charged particles (protons up to ≈ 250 MeV/u) and the high neutron detection efficiency for fast neutrons [31], the Baf_2 has two main purposes: generating the timing signals for triggering the DAQ and TOF (detailed description in section 2.2) and providing information on the particle residual energy based on the light output. Further information on the Barium Fluoride detector is given in appendix A.2.

2.2 Electronics and DAQ

Figure 2.2 shows a simplified scheme of the electronics and the DAQ system used for the experiment. The CAMAC-based DAQ [19] is running the Multi Branch System (MBS) [20] and can handle a trigger rate of ≈ 500 Hz. It is equipped with a Time-to-Digital Converter (TDC) and two QDCs using different gates for the long and short component of the BaF_2. The total number of primary ions traversing the START detector, the free triggers sent to the DAQ and the accepted triggers were recorded with an additional NIM-scaler. The anode signal of each detector is transferred from the cave to the control room, where the electronics setup and the DAQ system are located, by using ≈ 80 m long highly shielded signal cables. Analog splitters subdivide the outputs of the START and the BaF_2 for the TIME- and ENERGY-lines. The VETO signal is only acquired through the ENERGY-line as it is not needed for triggering or timing purposes. All analog outputs are delayed appropriately and connected to the QDCs (short gate for START, VETO and BaF_2 and long gate for BaF_2). A Constant-Fraction Discriminator (CFD) transforms the analog signals into NIM-standard logic-pulses. The CFD outputs are the basis for all gates and triggers of the DAQ system as well as the inputs for the TDC. The DAQ readout was triggered solely by the CFD signal of the BaF_2 scintillator. Even if more prone to record the intrinsic noise of the BaF_2, the chosen trigger offers a higher neutron efficiency than a trigger based on the coincidence between VETO and BaF_2 (due to the low neutron efficiency of the plastic scintillator). The noise can be characterized by acquiring data without beam and then removing the background offline. The two highlighted areas in figure 2.1 identify the most crucial points of the electronic setup related to the CFD setting and TOF logic.

- CFD gating - The long decay-time of the BaF_2-signal makes a discriminator dead time of $\approx 2.5\ \mu s$ absolutely necessary to prevent multiple triggering on a single event. The discriminator output is connected to a gate generator to create a $2.5\ \mu s$ long pulse, which then inhibits further pulses of the CFD within the same event. Nevertheless, the rate of ions impinging on the BaF_2 needs to be monitored carefully to prevent double hits and thus to be sure to always acquire the complete length of a single signal.
- Inverse TOF logic - Instead of measuring the temporal difference between START and BaF_2 signals, the latter is chosen as the start of the TDC while the coincidence between the BaF_2 signal and the delayed START signal is used as stop. This technique is called inverse time-of-flight and offers several advantages. The yield of particles reaching the telescope, especially for large angles, is low compared to the amount of primary ions impinging on the target. Using the standard time-of-flight setup would lead to a high trigger rate in the TDC even when only few particles reach the telescope and thus to unnecessarily recorded events where no fragmentation occurred in the area monitored by the telescope. To prevent the the BaF_2 noise collection in the TDC, the coincidence window between START and BaF_2 is set to a range of ≈ 100 ns, depending on the used TOF distance.

2.3 Data analysis and techniques

To obtain the angular distribution and energy spectra of all fragment species several steps are necessary. The raw output files of the DAQ are converted into ROOT files to be analyzed. Background, detector noise and uncorrelated events are removed from the spectra and CFD walk correction is applied. Different particle species are identified and their energy spectra calibrated. Considertions on the error of the conducted analysis steps are given in appendix D.

Noise reduction

The main sources of unwanted noise in the recorded spectra are: settings of the discriminator thresholds, choice of the DAQ trigger and detector high voltage. Background subtraction is applied to all experimental files. The activation of the cave and of the detectors as well as intensity fluctuations of the beam are time-dependent and are corrected file-by-file. Figure 2.5 shows the comparison between raw (black line) and background-corrected (red line) DAQ outputs for all detectors after conversion to a ROOT tree.

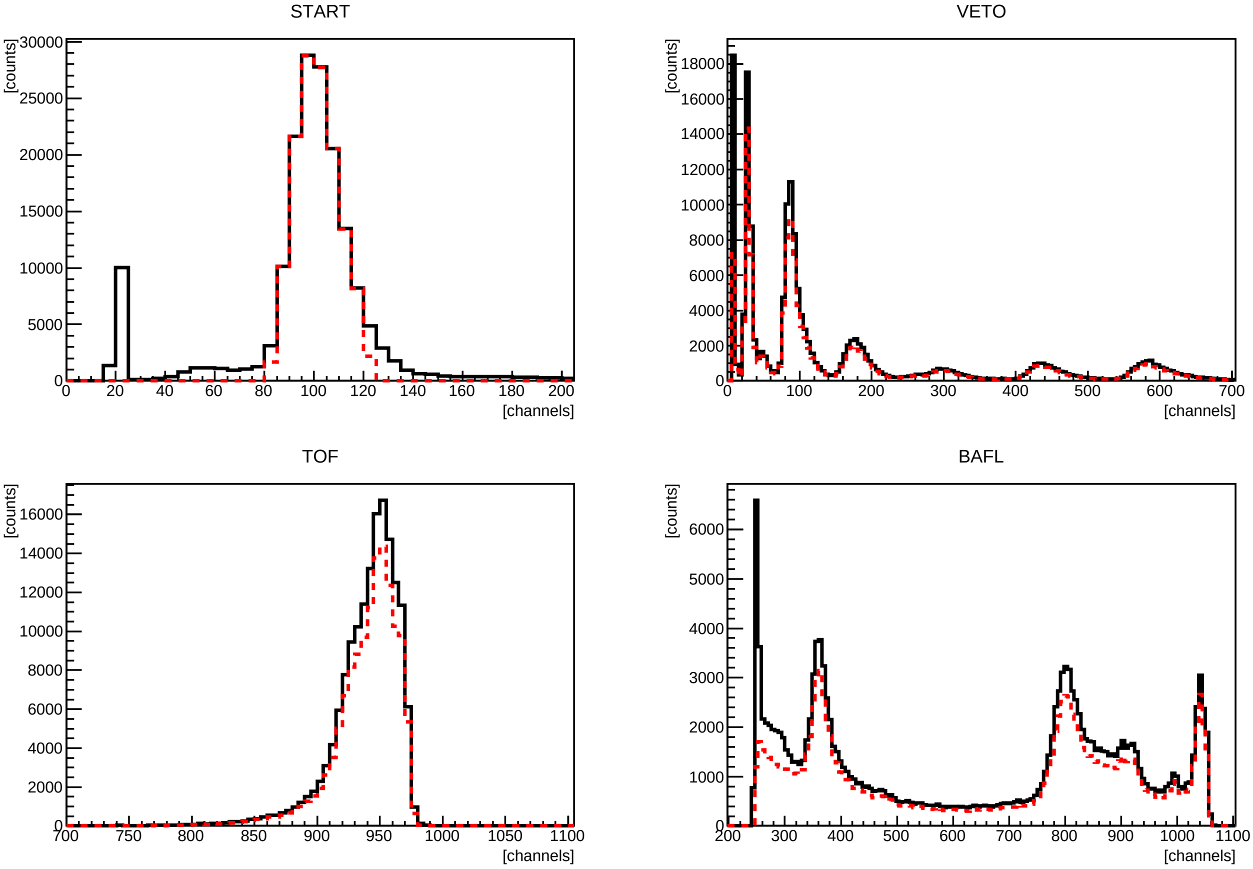

Figure 2.5.: Example of the raw spectra (black) and the spectra after noise subtraction (red) recorded with the QDCs for all detectors.

The START spectrum shows a clear peak of primary particles together with smaller peaks of pedestals (low channels), false triggers and double hits (high channels). Two 1-d cuts are applied, based on a Gaussian fit of the main peak with limits of $\pm 2\sigma$. These cuts are applied to the TOF spectra for over- and underflow as well as for pedestal removal in the BaF_2 spectra.

Charge identification

The VETO signal represents the energy loss ΔE of each particle in the scintillation material and hence is proportional to the square of the traversing particle charge (Eq. (1.10)), if e.g. quenching effects are neglected. A typical spectrum of the VETO is shown in figure 2.6.

Each peak represents a different ion type impinging on the detector, whereas the first peak is a combination of the signals from neutron, gammas and detector pedestal. The area of each distinct peak is a measure of the fragment yield but the shaded areas, marked in red and greeb, clearly show that the VETO alone is not sufficient for a full particle discrimination. To increase

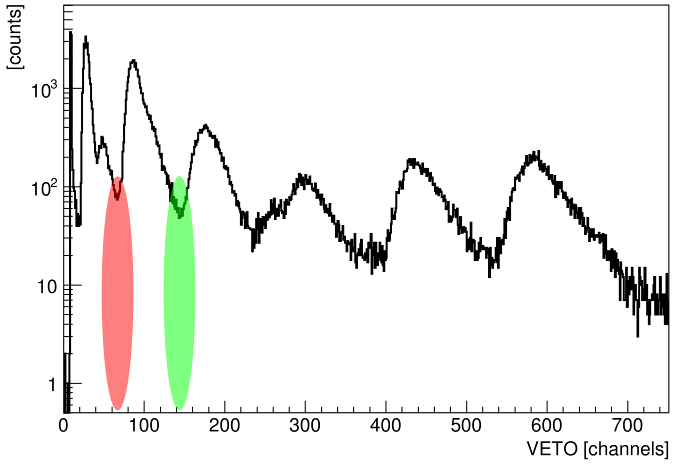

Figure 2.6.: Typical spectrum recorded by the VETO when placed close to the primary beam direction. The different peaks represent particles with charges from 1 to 6 (left to right). The leftmost peak is a combination of uncharged particles and pedestals of the detector. The marked areas (red and green) show the overlapping regions between two different charges where Particle IDentification (PID) based only on information from the VETO is not feasible.

the accuracy of the identification process it is necessary to correlate the information provided by the VETO with the residual energy (E_{tot}) or kinetic energy (E_{kin}) measured with the BaF_2 as shown in figure 2.7.

The correlation of the energy loss in the VETO with the residual energy or with the TOF provides a more accurate particle selection for charged and uncharged species using 2d-graphical cuts. An example of the PID performance for the 2 degrees measurement is presented in figure 2.8.

The identification and separation of uncharged particles, namely neutrons and photons, cannot be accomplished with the same methodology as used for charged particles because of their low interaction probability with the VETO detector. In most cases, an uncharged particle impinging on the telescope will deposit only a small amount of energy in the VETO, but might trigger the DAQ-readout due to the good efficiency of the BaF_2. Therefore, all triggered events within the pedestal peak of the VETO are either neutral particles or noise. Photons, which are moving with the speed of light, can be separated from the slower neutrons using their difference in time-of-flight. Neutrons that create recoil protons inside the 9 mm VETO detector will be misidentified as protons. For the VETO detector used in this setup Gunzert-Marx [31] reported a neutron efficiency of ≈1%, which decreases for increasing neutron energies, due to the decreasing probability of elastic scattering between neutrons and the hydrogen atoms of the scintillator. All 2d-cuts are performed independently on ΔE-E and ΔE-TOF spectra to test and compare the accuracy of the particle identification method and for error estimation.

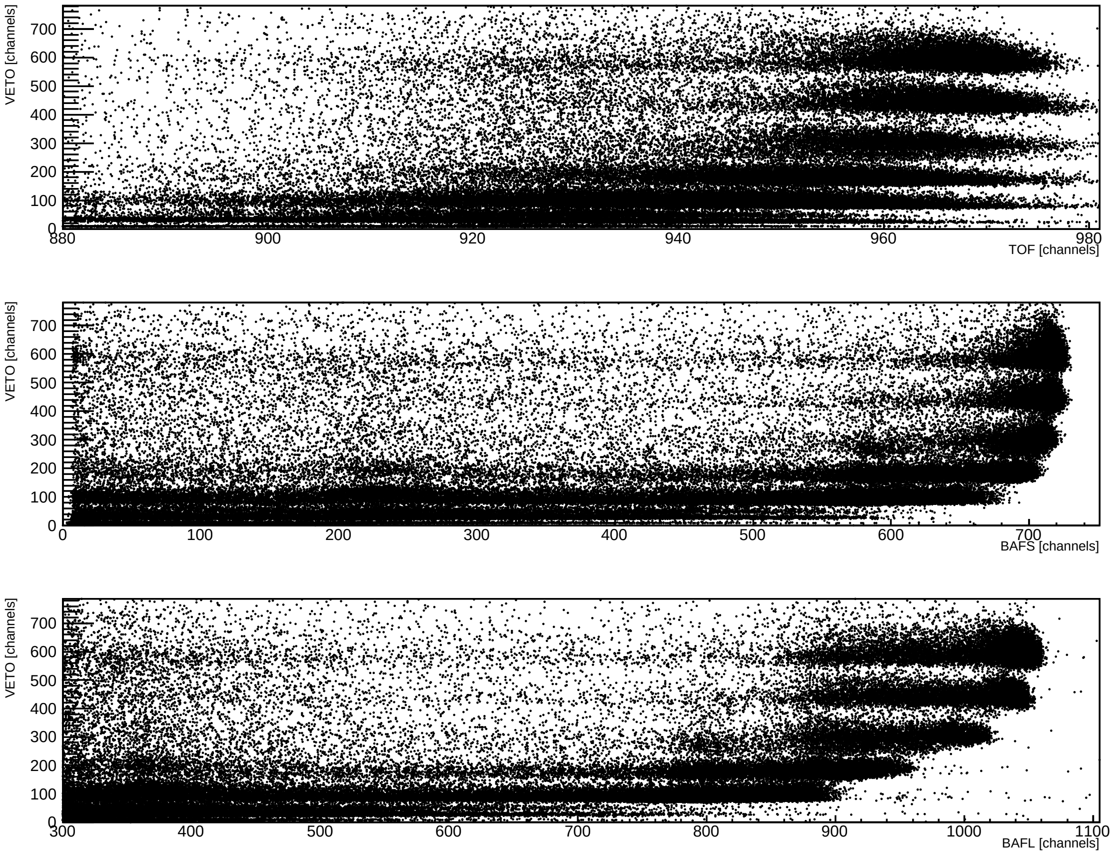

Figure 2.7.: Example of different 2d-plots for correlating the recorded information in order to improve the particle identification. The energy loss in the VETO is correlated either with time-of-flight, the short- or the long gate signal of the BaF_2 to increase the separation of the different charges.

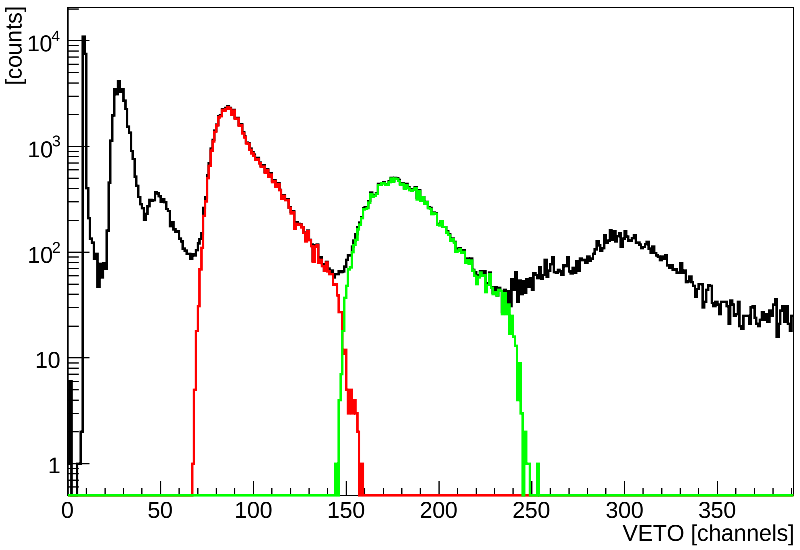

Figure 2.8.: Example of the PID performance when using 2d-cuts. The overlapping region between Z=2 (red) and Z=3 (green) ions can be resolved by using the correlation between VETO and TOF.

Walk correction

Due to the large dynamic range of the BaF_2 signal, a walk-correction is recommended for increasing the overall time resolution and balancing suboptimal discriminator settings [38] even when using a CFD. Raw spectra collected in this experiment show a significant walk (figure 2.9) and thus the correction is a crucial step to produce accurate data. To better understand the behavior of the used CFD and therefore the reason for the unexpectedly severe time walk, the module was tested with a fast arbitrary function generator (Agilent 81150A) simulating typical BaF_2 signals with varying rise times and amplitudes.

In order to perform an off-line walk-correction two sets of information are needed: the amplitude of the scintillator pulse on an event-by-event basis and a class of events covering the full range of amplitudes with known timing information. Gammas produced in the fragmentation process offer known timing information, but only cover the lower half of the short-gate QDC spectra. In order to get information on the full scale spectra a no-target measurement was performed placing the telescope at 0 degrees. The recorded primary particles have a well-defined and known kinetic energy and cover the missing high values in the short-gate QDC. To obtain a function for describing the discriminator walk trend, all recorded photons are selected and the mean TDC channel for a given QDC-range is calculated. Due to the assumption that fragmentation occurs in the center of the target and that a constant speed-of-light should lead to the same time-of-flight for all gammas, the differences between the mean values of the TDC in respect to

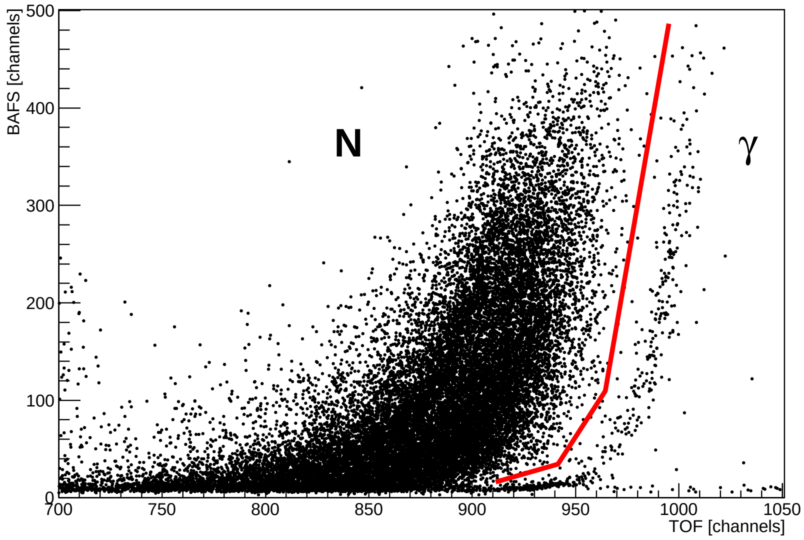

Figure 2.9.: Example of all neutral events recorded at 8 degrees. The neutron cluster (left) is well separated from the photon population (right). Instead of being distributed along a straight line as expected, the latter shows an amplitude-dependent bending due to the CFD walk.

their short-gate QDC values is a measure of the amplitude-based CFD walk. The same concept is applied to the no-target measurement at 0 degrees, where all primary ions impinging on the telescope are assumed to have the same energy and thus the same time-of-flight. The values so obtained are fitted with Eq. (2.1) [38] with T_{peak} as the mean TDC channel of a given QDC range, a_1 to a_3 as fit parameters and QDC_{mean} as the mean value of the selected QDC range.

$$T_{peak} = a_1 + a_2 \exp\left(\frac{a3}{\sqrt{QDC_{mean}}}\right) \tag{2.1}$$

The calculated correction values are applied event-by-event based on the short-gate QDC value and charge of the given event. The issue when applying the described method to this experiment is that the amplitude of the BaF_2 is not measured directly with a peak-sensing analog-to-digital converter (ADC), but with a QDC, and thus it has to be estimated with the short-gate QDC values. The detector response to differently charged and uncharged fragments (different peak-to-tail ratios) [56][77] leads to false amplitude predictions if the short gate does not only include the signal peak but also part of its tail. To minimize the possible impact of false amplitudes, the gamma-based walk correction is applied to neutral or Z<2 particles with QDC values below channel 500. For QDC values above channel 500 and particles with charged Z>2 the carbon-based correction is used. The effect of the walk correction is shown in figure 2.10. A detailed discussion on the uncertainty estimate for this correction is given in appendix D.3.

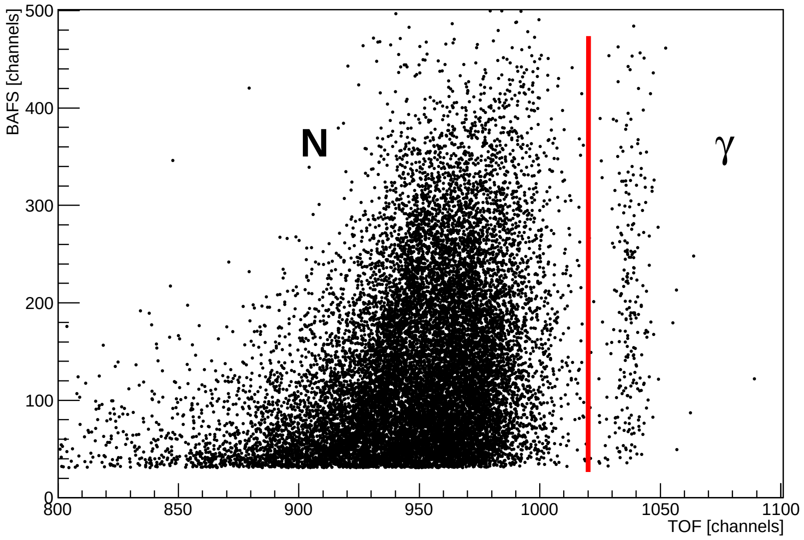

Figure 2.10.: Example of all neutral events recorded at 8 degrees with applied walk correction. The amplitude-based bending of the gamma-line (right) shown in figure 2.9 is nearly fully corrected.

Energy calibration

The TOF values are converted first into absolute time and then into kinetic energy either with a carbon-based calibration obtained at 0 degrees without the target or with the prompt photons calibration. In the former case, the walk-corrected TOF spectrum of the primary ions is fitted with a Gaussian function, whose mean represents the relative time in TDC channels needed to cover the distance between START and BaF_2 (figure 2.11).

Due to the application of the inverse-TOF technique, a longer time needed by a particle to reach the BaF_2 corresponds to lower channels in the TDC spectrum. Knowing the initial energy of the primary beam, its energy loss along the pathway (e.g. target, detectors, air gap...) between START and BaF_2 and the START-BaF_2 distance, it is possible to calculate the TDC channel representing the absolute TOF-zero. The TOF spectra are time-calibrated with a linear function whose intercept is the absolute TOF-zero value and slope the known resolution of the TDC. A similar approach is used for the calibration of the gamma-based walk-corrected events. The population of photons in the TDC histogram is selected and fitted with a Gaussian function. Using constant speed of light and known distance between START and target and between target and BaF_2 the absolute time a photon needs to travel from the target to the BaF_2 can be calculated. Based on this, the absolute TOF-zero is calculated and the spectra is calibrated using a linear fit.

The energy E of a particle is related to its absolute-calibrated time of flight t_{tof} as

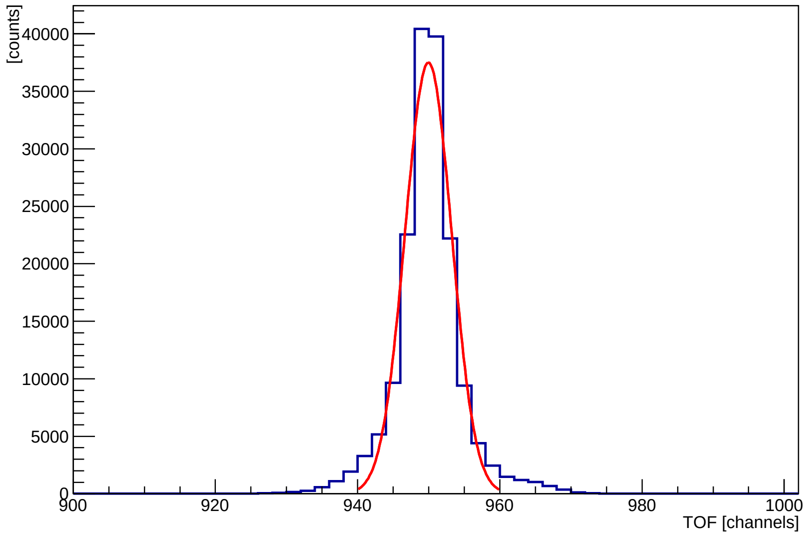

Figure 2.11.: Gaussian fit of the walk-corrected primary beam peak recorded with the TDC without target at 0 degrees. The mean value is used for the absolute time calibration of the TOF spectrum.

$$E = \left(\frac{1}{\sqrt{1 - (l/(t_{tof} \cdot c)^2)}} - 1 \right) m_0 c^2 \tag{2.2}$$

where l is the time-of-flight distance, c the speed of light and m_0 the mass at rest of the particle. The time-to-energy conversion is achieved using two approximations: the fragmentation of the primary projectile takes place exactly at the center of the target thickness and the velocity of the produced fragments is constant from the point of creation to the point of detection.

The relative uncertainty of the time-of-flight energy calibration is

$$\frac{\delta E}{E} = -\gamma * (\gamma + 1) * \frac{\delta t}{t}, \tag{2.3}$$

where γ is the Lorentz factor and $\delta t/t$ is the relative time resolution of the full system. As shown in Eq. (2.3), the relative energy error is increasing with decreasing time-of-flight because of the constant time-resolution δt. Therefore, an increase in the relative energy resolution can only be achieved by increasing the time-of-flight and thus the distance between the target and the telescope. The constant time resolution of the full system can be deduced by the FWHM of the walk-corrected gamma peak(≈0.2ñs). Details on the errors evaluation and the achieved time resolution can be found in appendix D.3. The energy-loss calculations used to calibrate this experiment were performed with LISE++(ATIMA) [78].

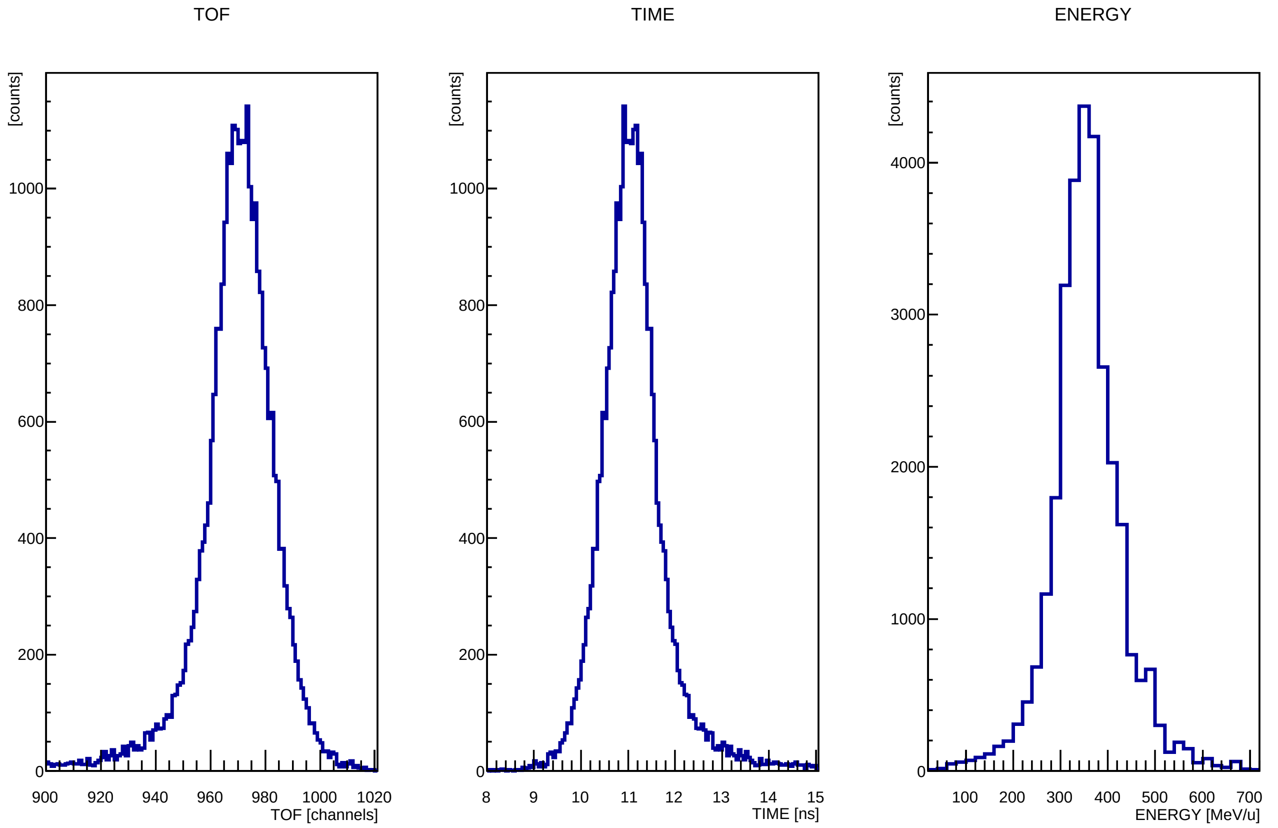

Figure 2.12.: Calibration of a raw TDC spectrum in channels (left) into an absolute time spectrum in ns (center) and finally in an energy spectrum in MeV/u (right).

2.4 BaF_2 neutron efficiency

Several studies investigated the BaF_2 scintillators response to fast neutrons [45, 79]. Gunzert-Marx et al. [31] reported that the neutron efficiency $\epsilon(E_n)$ can be parametrized as

$$\epsilon(E_n) = \epsilon_0(E_n) * e^{(-\lambda(E_n)*T)} \tag{2.4}$$

with $\epsilon_0(E_n)$ being the extrapolated efficiency at 0 MeV threshold, $\lambda(E_n)$ the slope dependent on the incident neutron energy and T the electronic detection threshold. The efficiency dependency on T can be understood by the way high energy neutrons interact with the detector material. As explained in chapter 1.1, the neutron energy loss can be described as several independent scattering processes where the deposited energy per interaction can vary over a wide range and neutrons can leave the active detector area. Hence, the pulse-height of the detector signal has no direct correlation to the energy of the impinging neutrons and a given energy threshold will not only affect specific energies but all recorded neutron events. As the detectors used in the present experiment are the same as in [31], the values for ϵ_0 and $\lambda(E_n)$ can be directly used to calculate the efficiencies for neutron energies up to 200 MeV/u. Values for higher energies are derived from data published in [79] after they have been corrected using a Monte Carlo simulation to take into account the different detector dimensions. Detailed information on this simulation are given in appendix B. The calculated conversion factors are presented in table B.4.

As reported in [33], neutron efficiencies based on the published data in [79] and rescaled to take into account different detector geometries seem to be lower compared to direct efficiency measurements. To minimize this discrepancy, the measured and recalculated efficiencies in the energy range between 100 and 200 MeV/u are averaged. Efficiency values for ≈100 MeV and ≈200 MeV available from both experiments are averaged, whereas values for neutron energies above 200 MeV are purely based on data published in [79]. The value measured at 147 MeV is not directly used for the fit to avoid an overestimate of the neutron efficiency in the energy range between 100 and 200 MeV/u. Figure 2.13 shows the neutron efficiency curve for an electronic threshold of 10 MeV_{PE}. The detection efficiency presents a clear maximum around 150 MeV/u, followed by a dip at intermediate energies in the range between 200 and 300 MeV. Above the latter value, the efficiency starts increasing again. The expected plateau region for neutron energies around 800 MeV is not visible. In order to obtain the efficiency curve over the energy range of interest, the values presented in [31] and the values derived from [79] are fitted with a function resulting from the sum of a Gaussian and an exponential functions. The parameters obtained from the fit are reported in table 2.2.

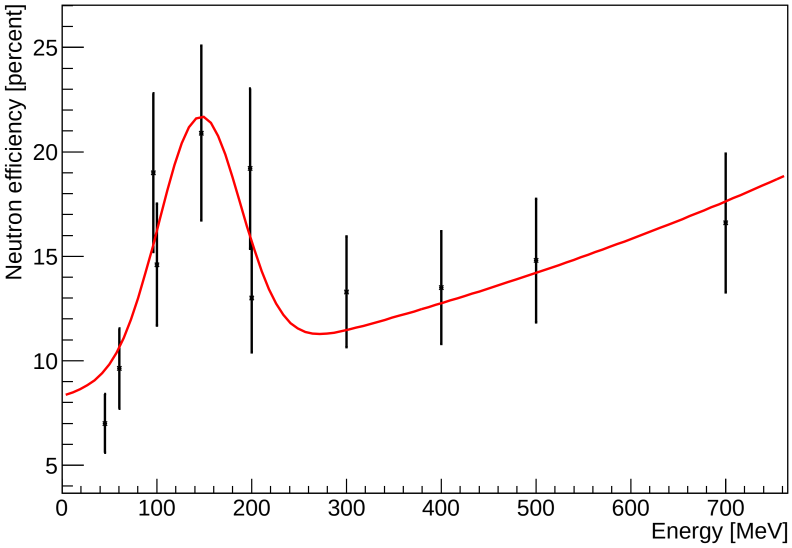

Figure 2.13.: Neutron efficiency curve used for this experiment.

p0	p1	p2	p3	p4
0.12(50.9)	145.21(4.2)	43.55(31.0)	-2.49(7.4)	$1.08*10^{-3}$(35.8)

Table 2.2.: Parameter values obtained by fitting the full scale neutron efficiency plotted in figure 2.13 with the sum of a Gaussian and an exponential function. The relative error is given in parentheses.

3 Results

3.1 Angular distributions

After identifying and selecting each particle species, the raw counts are corrected for the dead-time, defined as the time the DAQ is inhibited while processing a triggered event, and the fragmentation in the experimental setup itself. The results are normalized to the number of primary ions traversing the START detector in the specific run and to the telescope solid angle to obtain the yield:

$$yield = \frac{\Phi_{cor}}{\Phi_{0_{cor}} * \Omega} \tag{3.1}$$

where Φ_{cor} is the dead-time corrected number of events per incident ion, $\Phi_{0_{cor}}$ the fragmentation caused by the experimental setup estimated at 0 degrees without target and Ω the solid angle covered by the telescope. Neutron yields are further corrected by removing all gamma events and applying the energy-dependent efficiency factor discussed in section 2.4. A more detailed description of all applied corrections is reported in appendix D.1.

Experimental results

The yields of all particle species are reported in table 3.1 for all angles. For the data acquired at 0 degrees only the yield of carbon ions is reported because of the low occurrence for all fragment types which makes particle identification not feasible(total number of fragments < 5% compared to the amount of primary carbon). Furthermore, at this position the measurement uncertainty is large due to the leading-charge analysis, where the signal produced by light ($Z \leq Z_{\text{primary}}/2$) or uncharged fragments can be concealed by heavier ions, including the surviving primary beam particles, that hit the detector simultaneously. This behavior also occurs at all other measured positions but it is expected to be less severe with increasing angle due to the lower amount of heavy fragments as well as a smaller probability to have multiple particles impinging simultaneously on the detector. A possible solution to this problem is presented in appendix C. One of the main sources of error affecting the neutron yield are the recoil protons created in the VETO detector which lead to a misidentification of the particle species and thus to an underestimate of the produced neutrons and an overestimate of the produced protons [31].

The measured angular distributions are presented in figures 3.1,3.2 and 3.3. The angular distributions of all fragments peak in the forward direction, this behavior being more pronounced for the heavier particles. The main reason for this trend is related to the production mechanisms of the observed fragments. Particles created through abrasion or projectile ablation are mainly emitted at the same direction as the primary ions and thus have a strong forward momentum. Fragments produced by ablation of the target nuclei are mostly isotropic and thus contribute to a broadening of the angular distribution. Multiple interactions inside the target as well as the loss of heavier fragments stopped inside the absorber influence the angular distribution but in the present experiment their impact can be considered negligible due to the small thickness of the target and the high energy of the primary beam. As proposed by [27], the angular distribution of fragments with $Z \geq 2$ can be described accurately by the combination of two functions: a Gaussian function describing the fragmentation products created by projectile abrasion and ablation mainly in the forward direction and an exponential decay for the target evaporation products at larger angles. The angular behavior of hydrogen ions and neutrons differ from all other particles. The most suitable fitting function for the former is an exponential function as presented in [29], whereas the latter are well reproduced by two exponential functions as shown in [39]. The predicted trends of the angular distributions are well reproduced by the experimental values. Calculated fitting parameters are reported in table 3.2 for particles with $Z \geq 2$ and in table 3.3 for hydrogen fragments and neutrons. The relative difference between the angular distributions of hydrogen ions and neutrons normalized to the value at 2 degrees is shown in figure 3.4. Both particle types show a similar behavior, indicating that the influence of Coulomb scattering resulting in broader distributions for hydrogen fragments can be neglected for this experimental conditions. The lack of data at 0 degrees seriously hampers the comparison with the expected trend. Thus, the development of an experimental setup that provides an accurate yield measurement at 0 degrees is among the most important tasks for future experiments.

Monte Carlo simulations

The experimental results are compared to the predictions from two Monte Carlo codes: GEANT4 [2] v9.6 with QGSP_BIC_EMY physics list and PHITS [54] v2.24. Both codes used a simplified experimental geometry in order to decrease the calculation time without compromising the accuracy of the simulation. PHITS and GEANT4 are widely used for simulating light systems in the energy range of interest for carbon ion therapy [11] and overall showed a fair accuracy for thick tissue-equivalent targets [74, 75, 31, 15, 62]. A recent study on GEANT4 performances when reproducing a system similar to that used in this work (albeit at lower energy) can be found in [12]. The beam defined in the simulations is a 400 MeV/u ^{12}C Gaussian-shaped distribution with a diameter of 6 mm. The primary particles are transported to a 5x5x0.1 cm^3 volume of BC400 material reproducing the START detector before impinging on the 5x5x0.5

angle	charge		
[degrees]	neutron	1	2
2	$2.63 \cdot 10^{-3}$(4.5)	$1.72 \cdot 10^{-3}$(4.5)	$2.38 \cdot 10^{-3}$(4.5)
4	$1.41 \cdot 10^{-3}$(4.5)	$9.56 \cdot 10^{-4}$(4.5)	$6.92 \cdot 10^{-4}$(4.5)
6	$1.17 \cdot 10^{-3}$(4.5)	$7.69 \cdot 10^{-4}$(4.5)	$2.82 \cdot 10^{-4}$(4.5)
8	$8.18 \cdot 10^{-4}$(4.5)	$4.76 \cdot 10^{-4}$(4.5)	$9.87 \cdot 10^{-5}$(4.5)
15	$3.43 \cdot 10^{-4}$(4.5)	$1.02 \cdot 10^{-4}$(4.5)	$6.26 \cdot 10^{-7}$(7.2)

angle	charge			
[degrees]	3	4	5	6
0				$7.46 \cdot 10^{-1}$(4.5)
2	$8.66 \cdot 10^{-4}$(4.5)	$4.25 \cdot 10^{-4}$(4.6)	$5.68 \cdot 10^{-4}$(4.6)	$6.81 \cdot 10^{-4}$(4.5)
4	$9.21 \cdot 10^{-5}$(4.6)	$3.00 \cdot 10^{-5}$(5.0)	$1.16 \cdot 10^{-5}$(5.8)	$5.18 \cdot 10^{-6}$(7.2)
6	$1.71 \cdot 10^{-5}$(4.9)	$4.90 \cdot 10^{-6}$(5.7)	$1.13 \cdot 10^{-6}$(8.7)	
8	$3.62 \cdot 10^{-6}$(6.0)			

Table 3.1.: Experimental yields of neutrons and charged particles in msr^{-1} source^{-1}. The relative error is given in parentheses. The error given for the neutron yields does not include the error introduced by the efficiency calculations.

charge	g0	g2	e1	e2
2	$3.59 \cdot 10^{-3}$(0.1)	2.20(0.1)	-4.64(0.5)	$-6.16 \cdot 10^{-1}$(0.6)
3	$1.83 \cdot 10^{-3}$(2.2)	1.64(0.5)	-6.03(1.1)	$-8.18 \cdot 10^{-1}$(1.5)
4	$1.03 \cdot 10^{-3}$(3.9)	1.50(0.5)	-6.79(1.9)	$-9.06 \cdot 10^{-1}$(2.9)
5	$2.021 \cdot 10^{-3}$(2.2)	1.25(0.4)	-6.71(3.1)	-1.16(3.9)
6	$7.46 \cdot 10^{-1}$(2.0)	$5.34 * 10^{-1}$(0.2)	-2.41(3.1)	-2.44(1.3)

Table 3.2.: Parameters calculated from the angular distributions of particles with Z≥2 after fitting the data with a combination of two functions: g0$\cdot$ $\exp^{-0.5\cdot((x-g1)/g2)^2}$ (Gaussian fit) and $\exp^{e1+e2\cdot x}$ (exponential fit). The parameter $g1$ was fixed to 0 to center the Gaussian function at 0 degrees. Small angle data points were mirrored to improve the Gaussian fit. The relative error is given in parentheses.

	e1	e2	e3	e4
hydrogen	-5.99(0.3)	$-2.12 \cdot 10^{-1}$(1.0)		
neutron	-5.32(4.1)	$-3.12 \cdot 10^{-1}$(3.4)	-6.05(0.2)	$-1.26 \cdot 10^{-1}$(0.2)

Table 3.3.: Parameters calculated from fitting the hydrogen and neutron angular distributions with the function $\exp^{e1+e2\cdot x}$ and $\exp^{e3+e4\cdot x}$, respectively. The relative error is given in parentheses.

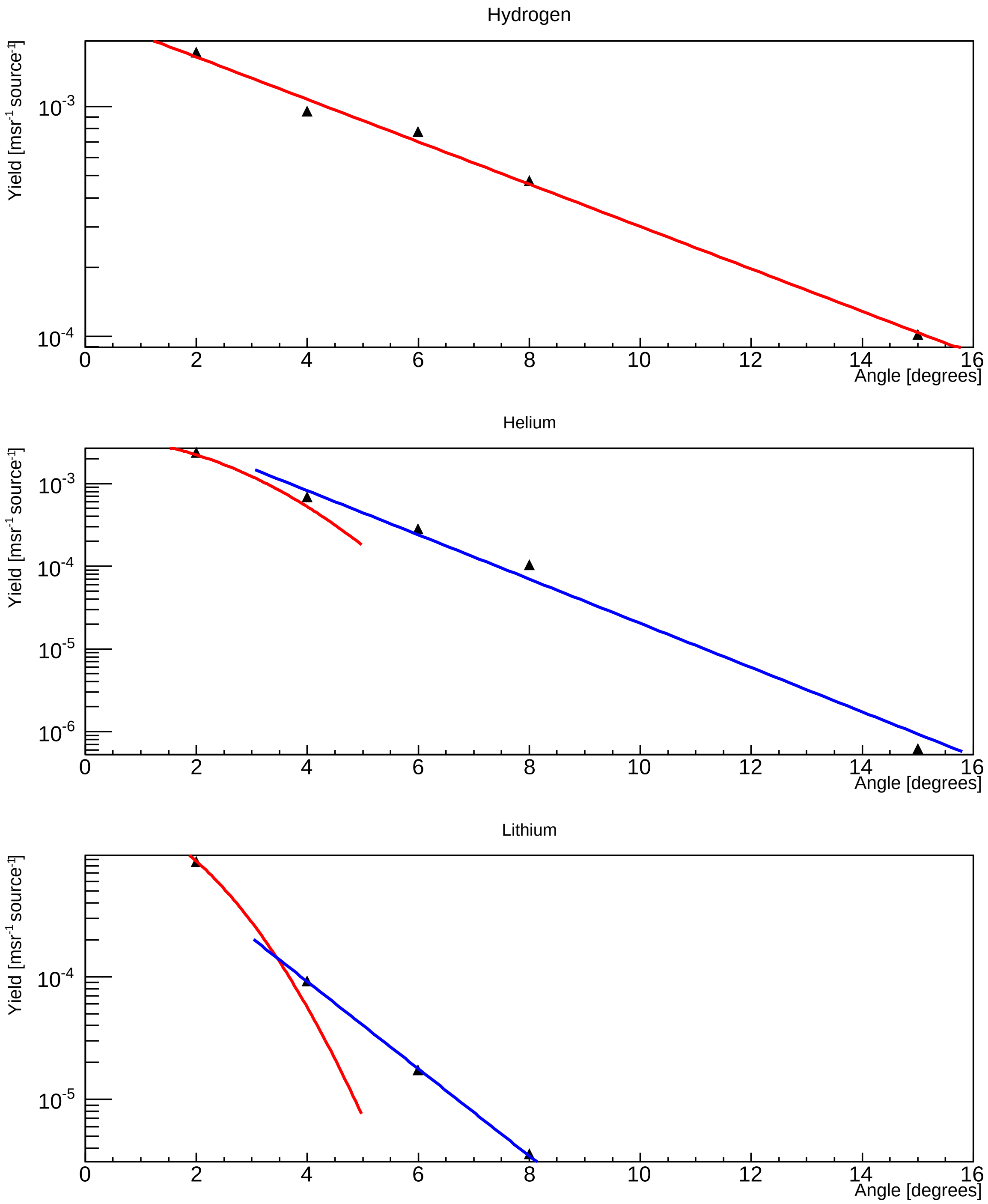

Figure 3.1.: Angular distributions of hydrogen, helium and lithium ions. As described by [29] the hydrogen distribution was fitted with a single exponential function whereas helium and lithium distributions were fitted with the combination of a gaussian and an exponential function [27]. Data points of small angles were mirrored in order to fit the gaussian part of the angular distribution.

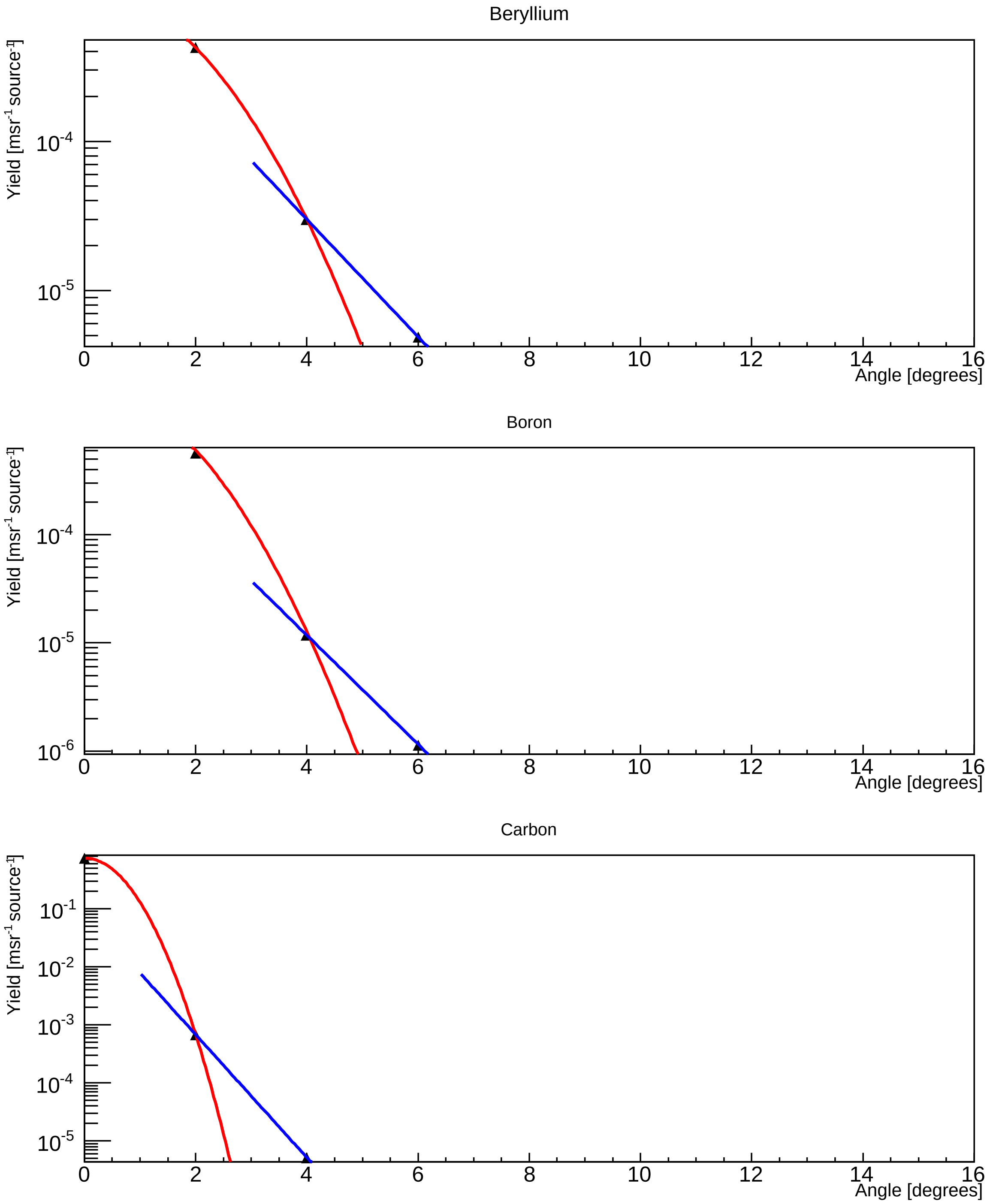

Figure 3.2.: Angular distributions of beryllium, boron and carbon ions. As proposed by [27] the heavier fragments were fitted with the combination of a gaussian and an exponential function. The data points of small angles were mirrored in order to fit the gaussian part of the angular distribution.

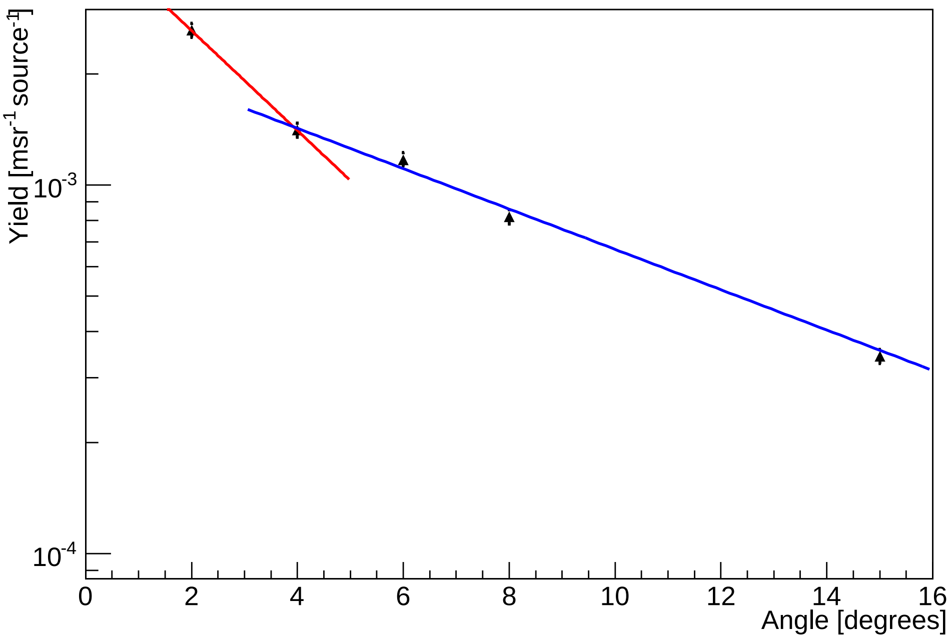

Figure 3.3.: Angular distribution of neutrons. The data points were fitted to two exponential functions [39].

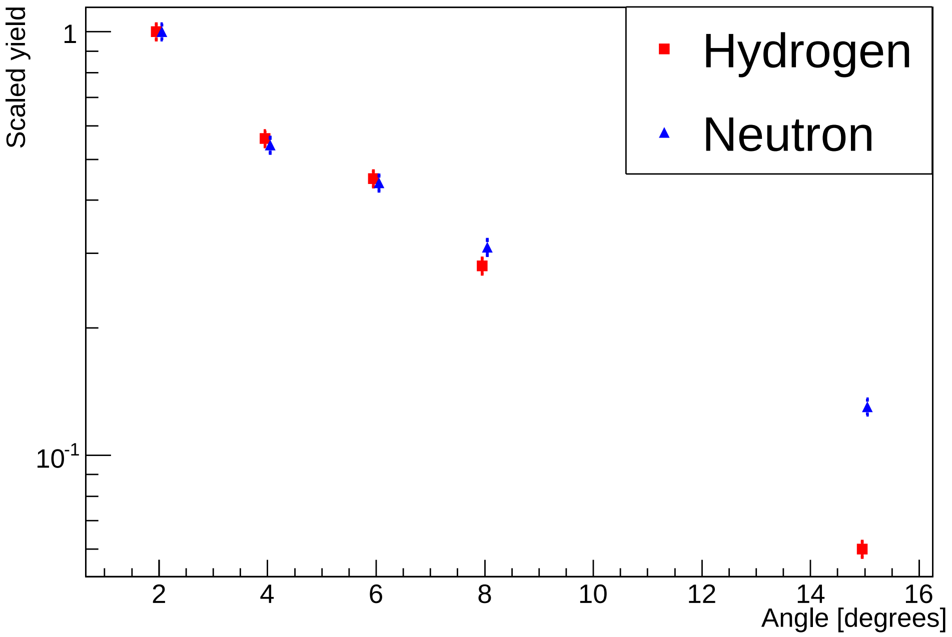

Figure 3.4.: Relative difference of the angular distributions of hydrogen and neutrons scaled to their respective 2 degrees values.

angle [degrees]	charge		
	neutron	1	2
0	$1.55 \cdot 10^{-1}(0.8)$	$1.30 \cdot 10^{-1}(0.9)$	$3.23 \cdot 10^{-2}(1.9)$
2	$2.56 \cdot 10^{-3}(1.1)$	$3.03 \cdot 10^{-3}(1.0)$	$2.38 \cdot 10^{-3}(1.1)$
4	$1.18 \cdot 10^{-3}(0.7)$	$1.44 \cdot 10^{-3}(0.7)$	$7.46 \cdot 10^{-4}(0.9)$
6	$7.01 \cdot 10^{-4}(0.5)$	$7.95 \cdot 10^{-4}(0.4)$	$1.56 \cdot 10^{-4}(1.0)$
8	$4.5 \cdot 10^{-4}(0.6)$	$4.74 \cdot 10^{-4}(0.6)$	$2.48 \cdot 10^{-5}(2.6)$
15	$1.99 \cdot 10^{-4}(0.7)$	$1.77 \cdot 10^{-4}(0.7)$	$2.92 \cdot 10^{-7}(18.3)$

angle [degrees]	charge			
	3	4	5	6
0	$2.40 \cdot 10^{-3}(7.0)$	$1.58 \cdot 10^{-3}(9.0)$	$3.02 \cdot 10^{-3}(6.0)$	$7.23 \cdot 10^{-1}(0.1)$
2	$1.95 \cdot 10^{-4}(4.1)$	$1.18 \cdot 10^{-4}(5.2)$	$2.35 \cdot 10^{-4}(3.6)$	$1.26 \cdot 10^{-3}(1.6)$
4	$4.53 \cdot 10^{-5}(3.8)$	$2.11 \cdot 10^{-5}(5.6)$	$1.13 \cdot 10^{-5}(7.6)$	$7.14 \cdot 10^{-6}(9.6)$
6	$2.72 \cdot 10^{-6}(6.9)$	$9.07 \cdot 10^{-7}(14.0)$	$3.78 \cdot 10^{-8}(44.7)$	$7.58 \cdot 10^{-8}(70.7)$
8	$1.25 \cdot 10^{-7}(40.8)$			

Table 3.4.: Particle yields calculated with PHITS Monte Carlo code in msr^{-1} source^{-1}. The relative error of the simulation is given in parentheses.

cm^3 elemental carbon target. The fragments and surviving carbon ions transverse an air gap before reaching the 10x10x0.9 cm^3 volume of BC400 material acting as VETO covering a cylindrical volume with a radius of 4.5 cm and a length of 14 cm representing the BaF$_2$. The output of the simulation includes the yield and kinetic energy of all particle species interacting with the VETO or BaF$_2$. Time-of-flight spectra are calculated for the path START-VETO and START-BaF$_2$. Detection efficiency for charged particles and neutrons is considered to be 100% and only particles below the BaF$_2$ detection threshold of $\approx$ 10 MeV are neglected. The impact of the thin aluminum beam-exit window (100 μm), the aluminum foil and the black tape covering the plastic scintillators is considered to be small and thus neglected. To estimate the effect of the cave geometry in the measurement, a dedicated simulation including the concrete walls, the optical stand used to align the beam line and the 1 mm aluminum case of the BaF$_2$ was run. The results are shown in appendix B. PHITS simulations cover all measured angles whereas, due to time-constraints and the significantly longer calculation times ($\approx$ 100000 events/day), GEANT4 simulations cover only a subset. The angular distributions are calculated using a similar set of ROOT functions as for the analysis of the experimental data. The simulated yields are reported in table 3.4 for PHITS and in table 3.5 for GEANT4. Further simulations have been performed to investigate the influence of small errors in the telescope positioning on the angular distributions at 2 and 4 degrees. To accomplish this goal, the position of the VETO-BaF$_2$ detectors in the simulation geometry was slightly varied and the corresponding particle yield calculated. The results of this test are reported in appendix B.

The angular distributions calculated with the PHITS Monte Carlo code are presented in figures 3.5 (hydrogen ions), 3.6 (particles with Z$\geq$2) and 3.7 (neutrons). The values for neutrons,

angle	charge		
[degrees]	neutron	1	2
0	$6.61 \cdot 10^{-2}$(0.8)	$1.10 \cdot 10^{-1}$(0.9)	$2.96 \cdot 10^{-2}$(1.6)
2	$1.44 \cdot 10^{-3}$(0.5)	$2.34 \cdot 10^{-3}$(0.4)	$2.01 \cdot 10^{-3}$(1.2)
4	$6.06 \cdot 10^{-4}$(7.3)	$1.02 \cdot 10^{-3}$(8.0)	$6.30 \cdot 10^{-4}$(9.8)
6	$3.90 \cdot 10^{-4}$(2.6)	$6.32 \cdot 10^{-4}$(2.9)	$1.97 \cdot 10^{-4}$(1.2)

angle	charge			
[degrees]	3	4	5	6
0	$5.90 \cdot 10^{-3}$(3.7)	$3.94 \cdot 10^{-3}$(4.5)	$8.35 \cdot 10^{-3}$(3.1)	$7.18 \cdot 10^{-1}$(0.3)
2	$4.68 \cdot 10^{-4}$(1.5)	$3.30 \cdot 10^{-3}$(3.7)	$5.42 \cdot 10^{-4}$(1.1)	$3.94 \cdot 10^{-4}$(0.8)
4	$1.09 \cdot 10^{-4}$(11.9)	$6.52 \cdot 10^{-5}$(5.6)	$5.49 \cdot 10^{-5}$(14.1)	$3.27 \cdot 10^{-5}$(13.9)
6	$1.82 \cdot 10^{-5}$(10.2)	$7.48 \cdot 10^{-6}$(22.0)	$1.79 \cdot 10^{-6}$(53.4)	$1.20 \cdot 10^{-6}$(82.2)

Table 3.5.: Particle yields calculated with GEANT4 Monte Carlo code in msr^{-1} source^{-1}.The relative error of the simulation is given in parentheses.

excluding the simulated point at 0 degrees, are well described by two exponential functions and are in agreement with literature [39]. The trend for hydrogen particles (figure 3.5) is not well reproduced by a single exponential function. Even excluding the data point at 0 degrees, the result for 15 degrees is too high compared to the expected behavior [29]. Particles with $Z \geq 2$ (figure 3.6) show in general a behavior closer to an exponential function than the measured distributions. This is especially evident for helium ions, whose distribution (excluding the point at 0 degrees) can be described well by a single exponential function. The Gaussian trend shown by the measured distributions at small angles is not observed in the simulated data with the exception of carbon ions ($Z=6$). A direct comparison of the measured and simulated results for neutrons, hydrogen and helium ions are shown in figures 3.9, 3.8 and 3.10, respectively. The agreement between experimental and Monte Carlo values is fair for neutrons at small angles, whereas the simulations underestimate the yield at larger angles and the angular behavior is steeper compared to the measured distribution. The simulation for hydrogen fragments (figure 3.8) predicts a lower yield for smaller angles and a higher value for larger angles. One possible explanation of this discrepancy is related to the analysis method (leading particle), which causes an underestimation of the amount of measured low-Z particles. Helium particles (figure 3.10) agree well for small angles with a steeper fall-off shown by simulation at bigger angles. The calculated yields using GEANT4 show a reasonable agreement for $Z \leq 3$ compared to the experimental data. The fragmentation yields for Beryllium isotopes are overestimated especially at 2 degrees, where GEANT4 predicts one order of magnitude higher values compared to the measurements. Boron yields show a high discrepancy at 4 degrees, whereas there is a reasonable agreement at 2 and 6 degrees. A similar behavior is observed for carbon particles at 4 degrees, where the measured and the simulated yields differ around one order of magnitude.

charge	e1	e2
2	$-4.65(8.2)$	$-6.83 \cdot 10^{-1}(12.6)$
3	$-4.37(0.4)$	$-1.41(0.3)$
4	$-4.46(1.1)$	$-1.57(0.8)$
5	$-9.78 \cdot 10^{-3}(3.7)$	$-2.85(0.4)$
6	$-1.81(1.0)$	$-2.43(0.5)$

Table 3.6.: Parameters calculated from the simulated angular distributions of particles with Z≥2 after fitting the data with $\exp^{e1+e2\cdot x}$ (exponential fit). The combination of a Gaussian function and an exponential one, used for the experimental data, is not able to describe the simulated data points.

	e1	e2	e3	e4
hydrogen	$-5.17(1.7)$	$-3.17 \cdot 10^{-1}(9.2)$		
neutron	$-5.33(2.5)$	$-3.29 \cdot 10^{-1}(9.1)$	$-6.15(0.2)$	$-1.72 \cdot 10^{-1}(0.1)$

Table 3.7.: Parameters calculated from fitting the simulated hydrogen and neutron angular distributions with the function $\exp^{e1+e2\cdot x}$ and $\exp^{e3+e4\cdot x}$, respectively. The relative error is given in parentheses. The intermediate angles starting from 2 degrees up to 8 degrees are well reproduced by a single exponential curve for the hydrogen case.

The comparison of GEANT4 and PHITS shows in general more agreement for smaller angles and smaller charges. The yields of e.g. helium are comparable up to 6 degrees, but the lithium yield at 6 degrees shows a deviation of one order of magnitude. The non-systematic behavior of the GEANT4 yield prediction was not expected. Bóhlen *et al.* [8] investigated the performance of GEANT4 and FLUKA by comparing it to experimental data of 400 MeV/u ^{12}C impinging on thick water targets [35]. It was shown that GEANT4 systematically underestimated the yield at small angles and it overestimated them at larger angles. Due to similar geometrical simplifications in the simulation setup (see appendix B for details), the discrepancy could be explained by a different performance of the physical models when applied to thin elemental targets compared to thick composite absorbers. Most experiments considered for benchmarking the physical models in the energy region used in particle therapy are mostly based on data for thick tissue-equivalent targets and therefore a better simulation accuracy can be expected.

Comparison with literature

In literature, only a few measurements for the fragmentation of light ions (1≤Z≥12) on different targets in the energy range of interest for radiotherapy (80 - 400 MeV/u) are available. They include:

- total charge-changing or individual charge-changing cross sections [28, 70, 55, 80, 21];
- angular differential cross sections on tissue-equivalent targets [32, 35, 67];

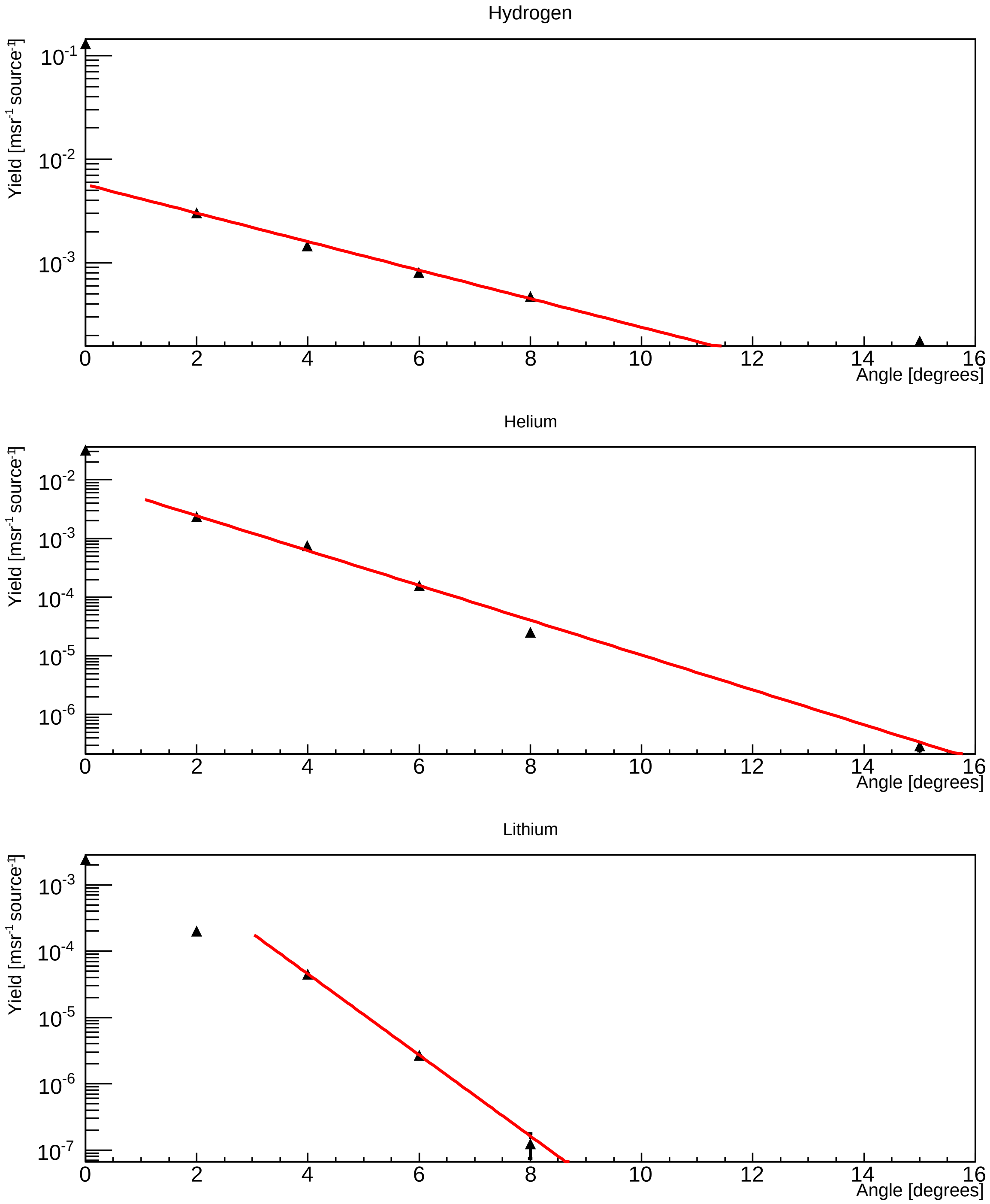

Figure 3.5.: Angular distributions for hydrogen, helium and lithium ions simulated with PHITS..

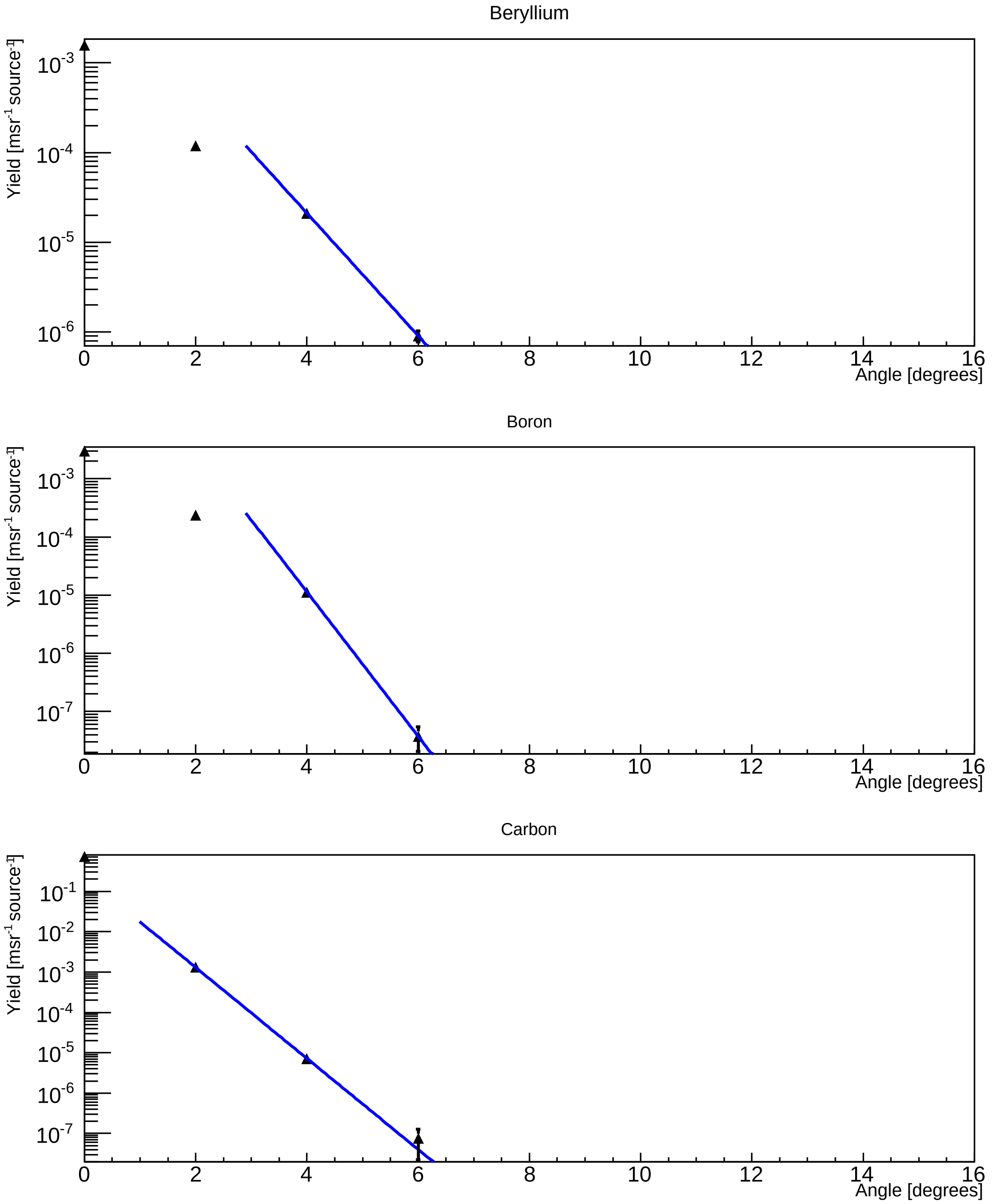

Figure 3.6.: Angular distributions of beryllium, boron and carbon ions simulated with PHITS.

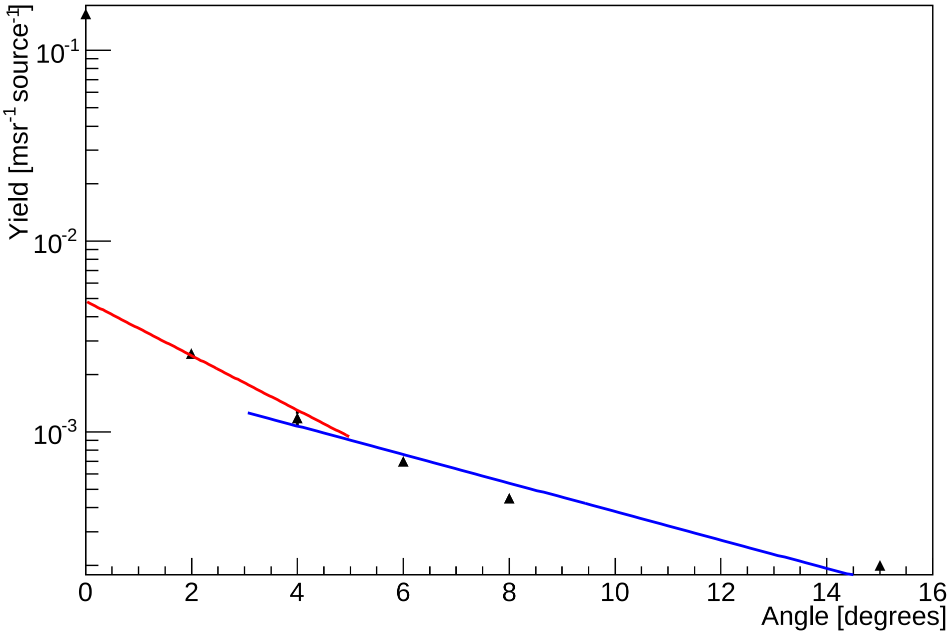

Figure 3.7.: Angular distribution of neutrons simulated with PHITS.

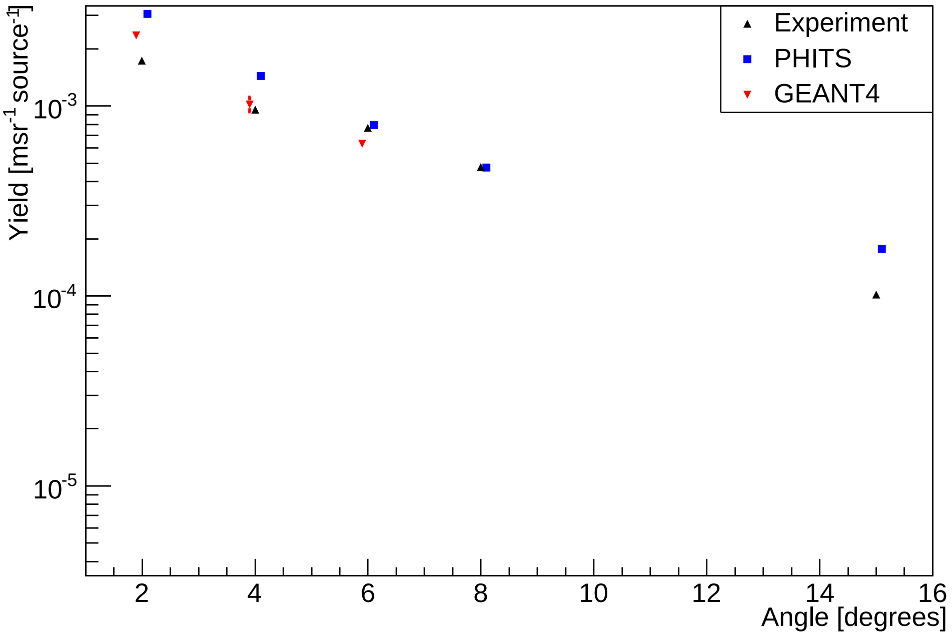

Figure 3.8.: Comparison of the angular distributions from experiment and Monte Carlo simulations (PHITS and GEANT4) for hydrogen ions.

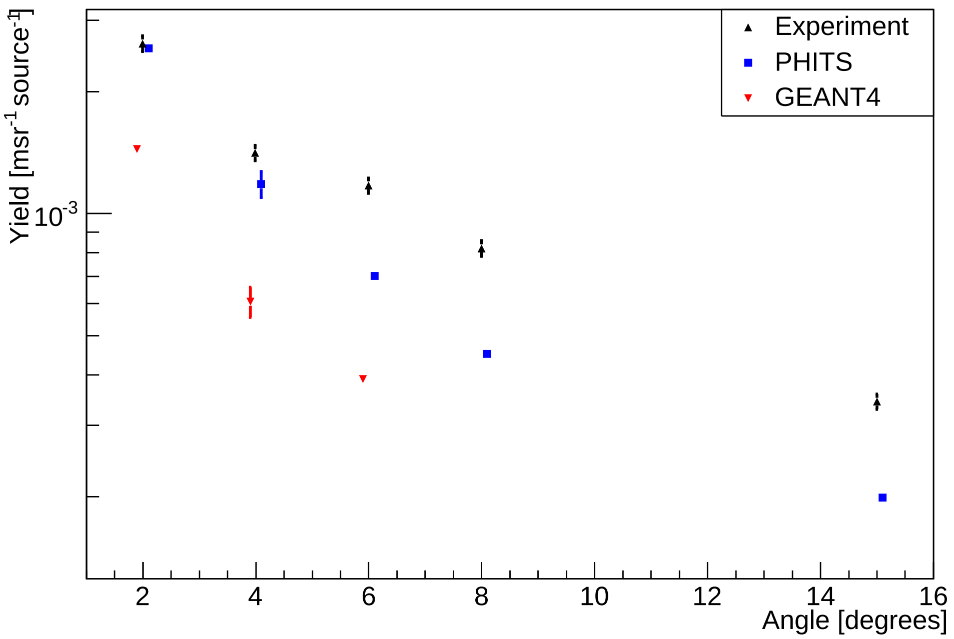

Figure 3.9.: Comparison of the angular distributions from experiment and Monte Carlo simulations (PHITS and GEANT4) for neutrons.

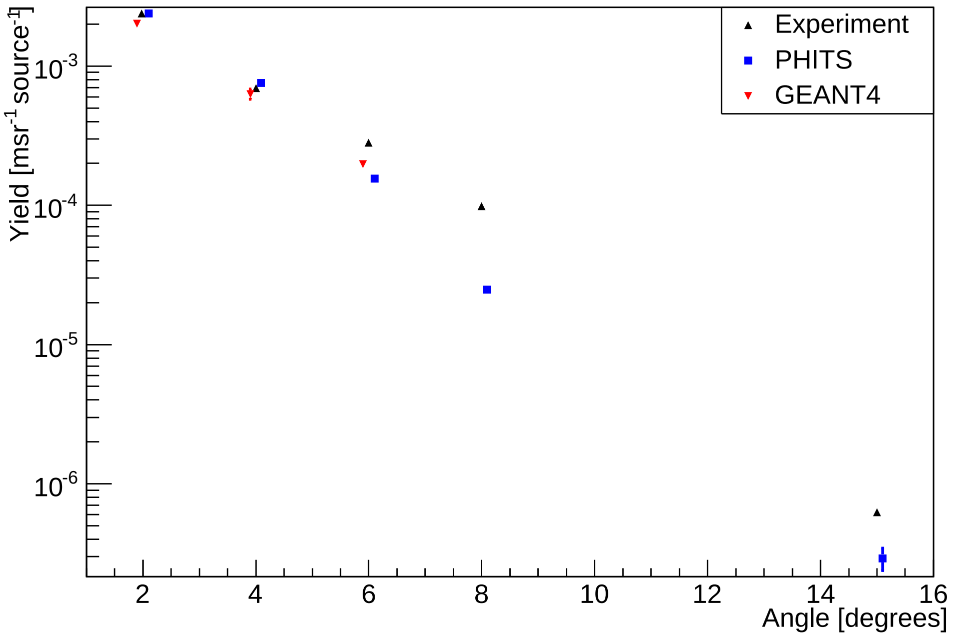

Figure 3.10.: Comparison of the angular distributions from experiment and Monte Carlo simulations (PHITS and GEANT4) for helium.

- double differential cross sections using thin elemental targets [12, 15].

The following reasons prevent a comparison between the results reported in section 3.1 and data from literature:

- absence of measurements at 0 degrees and the resulting high uncertainty in the integrated production rate;
- difference in the target composition e.g elemental target (carbon)versus tissue-like (water) target;
- large difference in target thickness e.g thin target versus thick absorber, where secondary processes like multiple scattering and secondary fragmentation have an impact on the cross section;
- strong energy dependence of the fragmentation cross section for beam energies around 100 MeV/u.

The FIRST experiment [60] measured a similar system than the one selected for this experiment but the data analysis is still in progress.

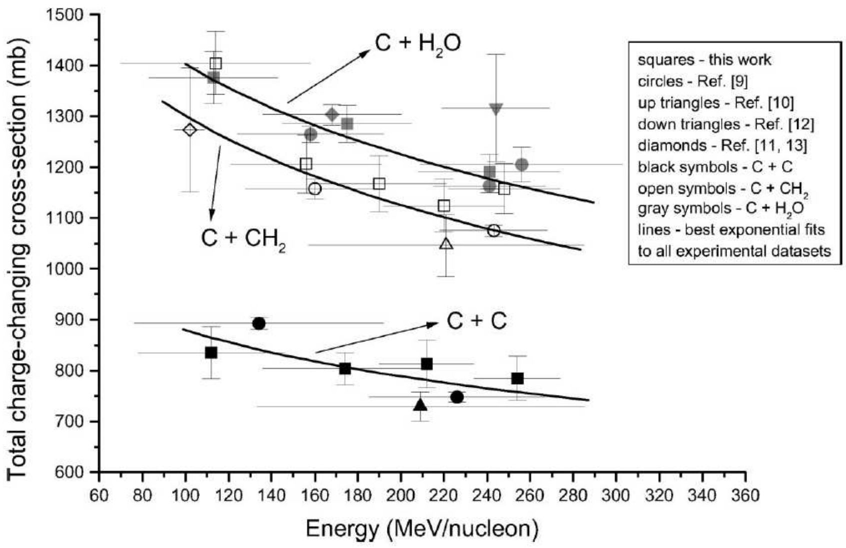

Figure 3.11.: Energy dependence of the total charge-changing cross section for carbon ions impinging on carbon, polyethylene and water targets [28].

The differential cross sections for charged and uncharged particles obtained in this experiment can only be compared with data presented in [85, 42, 40].

Zeitlin *et al.* [85] used a silicon-based telescope and a 400 MeV/u ^{12}C beam impinging on a 2 g cm^{-2} graphite target. The results of the comparison are presented in table 3.8. Even if the measured angles in the two experiments are not exactly the same, the data shows reasonable

	angle [degrees]	charge 1	2	3	4
This work	4	10.36(4.5)	7.5(4.5)	1(4.6)	0.32(5.0)
[85]	5	7.63(3.0)	4.22(3.1)	0.20(5.0)	0.054(9.3)
This work	6	8.33(4.5)	3.1(4.5)	0.19(4.9)	0.05(5.7)
This work	8	5.16(4.5)	1.1(4.5)	0.04(6.0)	
[85]	10	4.17(3.8)	0.61(6.6)	0.011(45.5)	0.003(66.7)

Table 3.8.: Comparison of differential cross sections measured in this work and by [85] given in b sr^{-1} . The relative error is given in parentheses.

	angle [degrees]	charge 3	4	5	6
[42]	1.7	6.19	5.19	15.73	6.64
This work	2	9.39(4.5)	4.61(4.6)	6.16(4.6)	7.38(4.5)
[42]	2.1	5.66	4.19	10.03	3.26

Table 3.9.: Comparison between differential cross sections measured in this work and by [42] given in b sr^{-1}. The relative error for this work is given in parentheses. The relative error for the data presented in [42] could not be derived from the plots.

agreement and follow the expected trend. The cross sections for hydrogen particles at 6 degrees observed in this experiment are higher compared to the 5 degrees measurements by Zeitlin *et al.*. As expected, both experiments show significantly higher values for helium ions compared to lithium particles. This behavior is due to the fact that the breakup of carbon ions into three alpha particles following a central collision is far more likely than producing lithium isotopes and thus more probable.

Kidd *et al.* [42] used a Cherenkov-CsI telescope, a primary beam energy of 250 MeV/u and a 1.15 g cm^{-2} graphite target. The isotope cross sections were summed up to get the differential cross sections per charge as measured in this experiment. The results of the comparison are presented in table 3.9. As the values from Kidd *et al.* were retrieved directly from the published plots using plot digitizer [14], they are prone to a significant readout error estimated to be around 10%. The agreement of the two datasets is not really good. Hydrogen cross sections are ≈50% higher in this experiment than reported in [42], which might be due to the different target density as well as a lower primary beam energy. The biggest difference is observed for boron isotopes. Small angular changes of the detector position can lead to deviations in the measured cross sections for small angles due to the high gradient of the angular distribution especially for heavier fragments. Nevertheless, this alone cannot explain the discrepancy of the data at 2 degrees compared to the values measured at 2.1 degrees.

Iwata *et al.* [40] used a telescope composed of a 5 mm NE102A plastic scintillator and a cylindrical NE213 liquid scintillator for measuring neutron yields and energy spectra. The dataset of interest for the comparison consists of two measurements, one using a 290 MeV/u ^{12}C beam and

	angle [degrees]	cross section [b sr^{-1}]
This work	4	15.28(4.5)
[40] 290 AMeV	4.4	7.38
[40] 400	4.6	3.31
This work	6	12.68(4.5)
This work	8	8.87(4.5)
[40] 290	9	3.31
[40] 400	9.88	1.2
This work	15	3.27(4.5)
[40] 290	20	0.96
[40] 400	19.75	0.8

Table 3.10.: Comparison between differential neutron cross sections measured in this work and measured by [40].The relative error for this work is given in parentheses. The relative error for the data presented in [40] could not be derived from the plots.

a 1.8 g cm^{-2} graphite target and the other a 400 MeV/u ^{12}C beam and a 9 g cm^{-2} graphite target. The results of the comparison are presented in table 3.10. The values for Iwata *et al.* were retrieved directly from plots using plot digitizer [14] and thus might be prone to a large uncertainty. The measured differential cross sections of this experiment are a factor ≈2.5 higher than the data presented in [40]. Comparing the relative difference between the measurements, the general behavior seems to indicate an overestimation of the neutron differential cross sections reported in this experiment. This hypothesis is supported by the results presented in section 3.1, where the PHITS simulation showed lower neutron yields especially for larger angles compared to this measurement.

3.2 Energy distributions

After identifying the different particle species and calculating their respective yields, the fragment kinetic energy is determined for all measured angles using the inverse time-of-flight technique described in section 2.3. The obtained double differential distributions at 2 degrees are reported in figure 3.12.

Hydrogen ions and neutrons show a likewise behavior. The energy spectra present a broad peak, a low energetic tail and an exponential fall-off to higher energies up to around twice the primary beam energy. Heavier particles, like boron, show a different trend, with a peak followed by a shorter tail for lower energies and a sharp fall-off for energies around the primary beam value. The peak position of light ions (e.g. helium) located at a significantly lower energy than the heavier fragments and the carbon ions indicates a problem in the energy calculation (as discussed in section 2.3). In order to investigate this behavior the calibrated time values for the measurements at 2 degrees are presented in table 3.11.

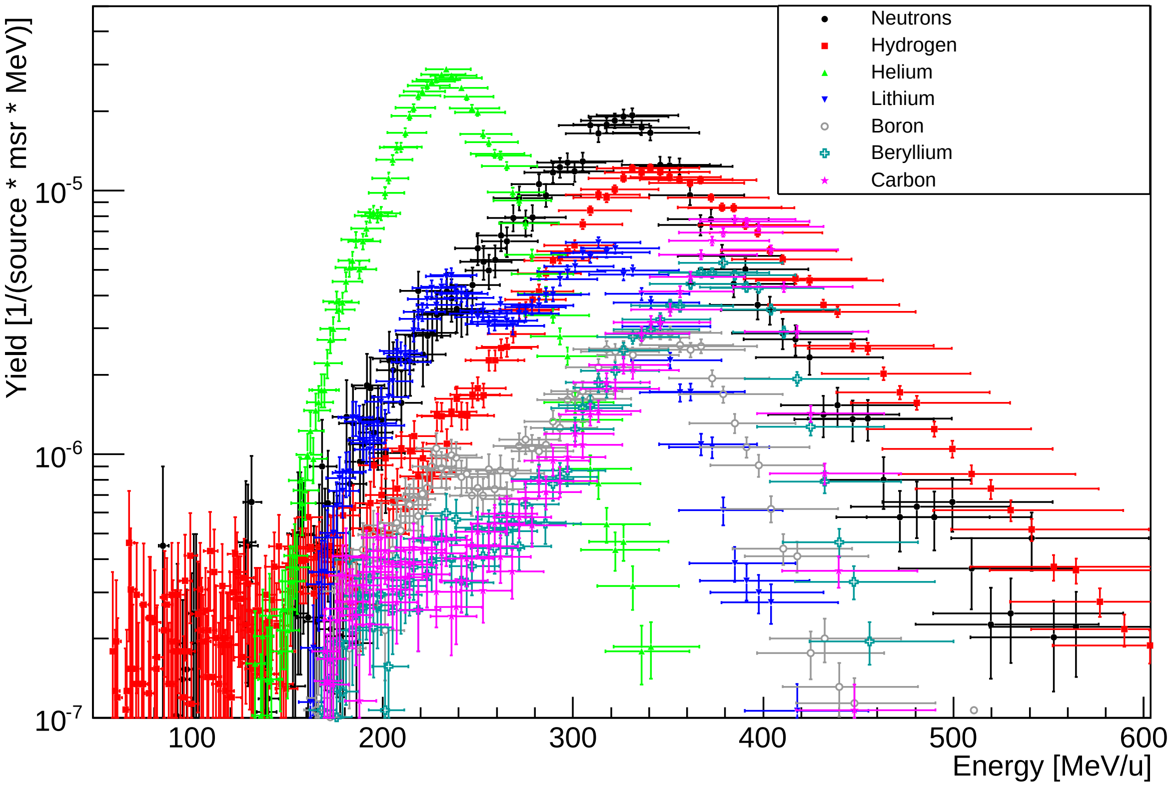

Figure 3.12.: Energy spectra measured for all fragments at 2 degrees. The vertical axis shows the number of fragments per msr and MeV normalized to the amount of primary ions impinging on the target.

charge	1	2	3	4	5	6
time [ns]	11.03	12.67	11.46	10.78	10.85	10.75

Table 3.11.: Calibrated and walk-corrected time-of-flight peak values for all measured charges at 2 degrees.

The kinetic energy spectra at small angles are expected to peak for all particle species close to the primary beam value neglecting small deviations due to different energy losses in the air gap. The differences in time-of-flight of hydrogen, beryllium, boron and carbon ions are close to the minimum timing error experimentally achievable with the used CFD (at least 200 ps as stated by the manufacturer and verified by tests with fast arbitrary function generators). Discrepancies in this time interval are due to experimental timing errors. Further information on the error of the energy calculation is given in appendix D.3. For helium and lithium ions, the arrival times are significantly lower implying an incorrect walk adjustment. The failure of this correction can be explained by taking into account the BaF_2 response to different particle species and the corresponding signal acquired in the short-gate QDC. The signals from which the walk correction was estimated are generated by two types of events: quasi- monoenergetic carbon ions at 0 degrees without target or prompt photons created during the fragmentation process. The adjustment is calculated from the signals acquired with the short-gate QDC information as a substitute for the amplitude to the measured time-of-flight under the assumption that the QDC contains, in an ideal case, only information about the peak of the detector signal. The reason for this assumption is the relation of amplitude and discriminator walk shown in figure 3.13. If instead the short-gate QDC includes part of the charge-dependent signal tail (peak-to-tail ratio smaller for bigger charges) the corrections derived from e.g. carbon ions will work worse for particles with increasing ΔZ as well as with increasing amount of tail recorded by the short-gate QDC and cannot be corrected without proper information on the amplitude. The reason for the usage of two different walk corrections based on photons (high peak-to-tail ratio) and carbon particles (low peak-to- tail ratio) was to mitigate the influence of the recorded tail in the short-gate QDC. For both walk correction methods helium and lithium ion have the largest ΔZ from the primary beam and therefore are more affected by the tail. Hence, the uncertainty on the energy measurements for helium and lithium particles is considered too large and the data are not discussed further. Another possible error introduced by an incorrect walk adjustment is a change in shape of the measured distributions due to wrongly applied time shifts based on faulty amplitude predictions. In order to investigate this effect several files where calculated with and without walk correction and the resulting distributions compared. The non walk corrected file is always shifted by hand so to match the position of the time peaks and thus achieve a better comparison of the distribution shapes. An example of this procedure is given in figure 3.14 for hydrogen ions and in figure 3.15 for boron ions. The comparison shows that the impact of the walk correction on the shape is, as expected, ΔZ dependent and results generally in a sharper central peak region as well as steeper fall-offs for low and high energies. As proven by figures 3.14 and 3.15, the difference is more severe for hydrogen particles compared to boron ions due to their wider distribution in the short-gate QDC.

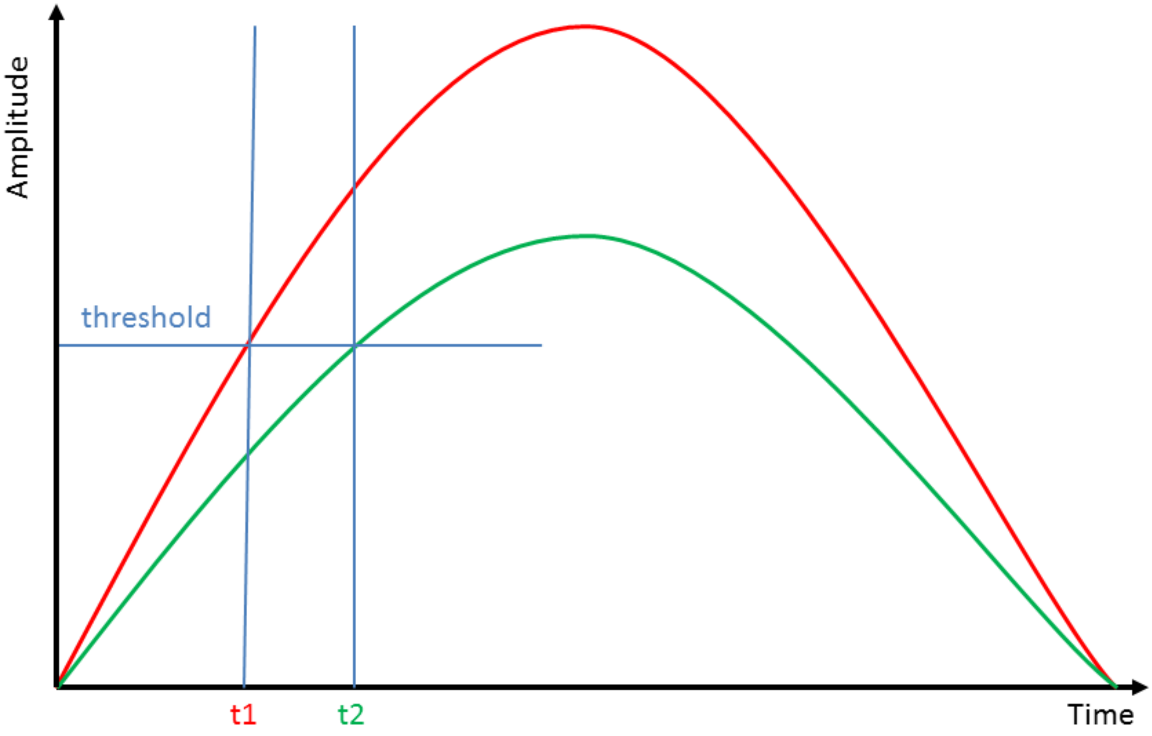

Figure 3.13.: Scheme of the amplitude-based discriminator walk. Even though a CFD was used during the experiment, tests with a fast arbitrary function generator (Agilent 81150A) showed that the time walk was not affected severly by the rise time of the detector signal but predominantly by the signal amplitude. This beahvior is quite uncommon for CFDs and more expected while using leading edge discriminators instead. Signals with constant rise time but different amplitudes will pass a certain discriminator threshold at different times. The amplitude-based discriminator walk is defined as this difference in time.

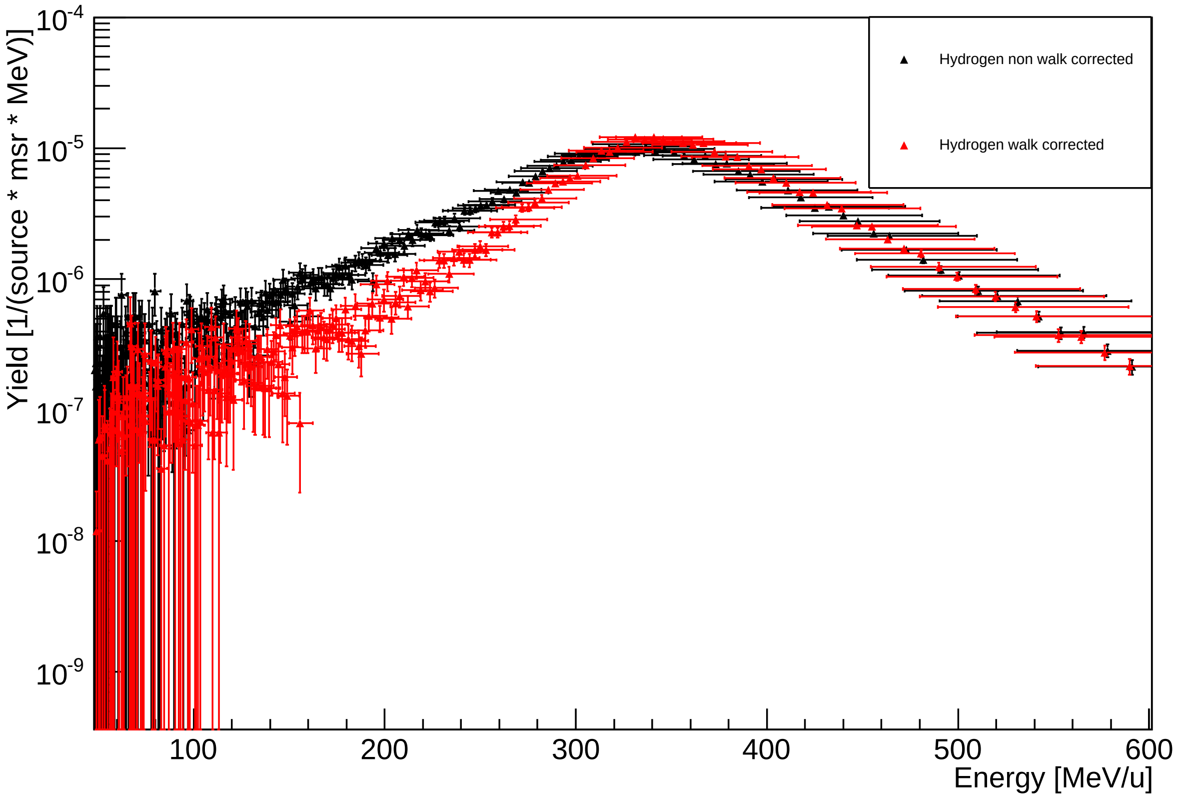

Figure 3.14.: Comparison of walk-corrected and non walk-corrected kinetic energy spectra of hydrogen particles at 2 degrees. For easier comparability of the shape of the energy distributions the non walk-corrected spectrum is shifted to match the peak energy of the corrected one. The vertical axis shows the number of fragments per msr and MeV normalized to the amount of primary ions impinging on the target.

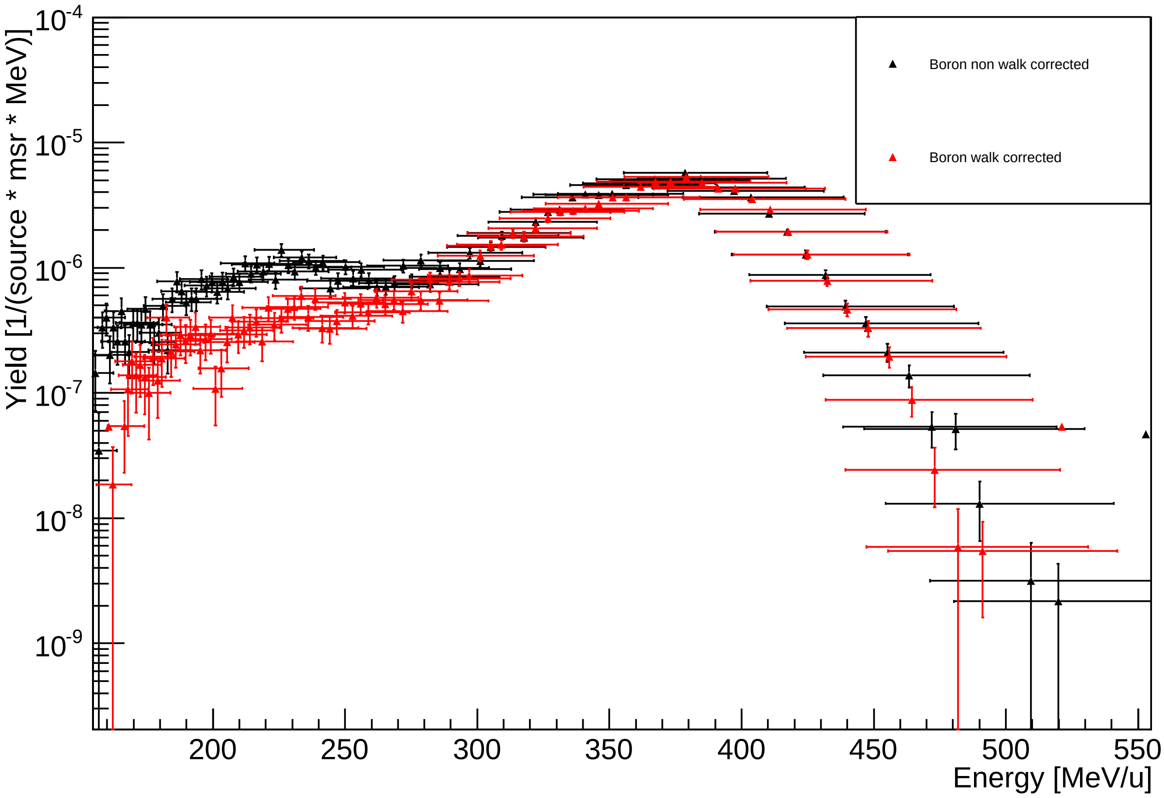

Figure 3.15.: Comparison of walk-corrected and non walk-corrected kinetic energy spectra of boron particles at 2 degrees. For easier comparability of the shape of the energy distributions the non walk-corrected spectrum is shifted to match the peak energy of the corrected one. The vertical axis shows the number of fragments per msr and MeV normalized to the amount of primary ions impinging on the target.

According to theoretical fragmentation models [6] the energy spectrum consists of three parts: a peak region around the primary beam energy created mainly by projectile abrasion, a low energy tail mainly produced by target evaporation and a high energy tail due to projectile evaporation. The high energy region for protons and neutrons is expected to extend up to two times the energy of the primary beam. The initial collision between projectile and target frees a nucleon from its binding forces and imparts energy to the latter up to the value per nucleon of the impinging projectile. If the direction of the nucleon is such that it can undergo a subsequent collision with the projectile nuclei ("hit from behind") additional energy is transferred. For heavier particles the amount of possible transferred energy drops significantly limiting their high energy tail to values closer to the primary beam value. In addition, the probability for creating heavier particles by evaporation is comparably lower and therefore their peak region is expected to be sharper than neutrons and protons, neglecting additional effects due to Coulomb interaction.

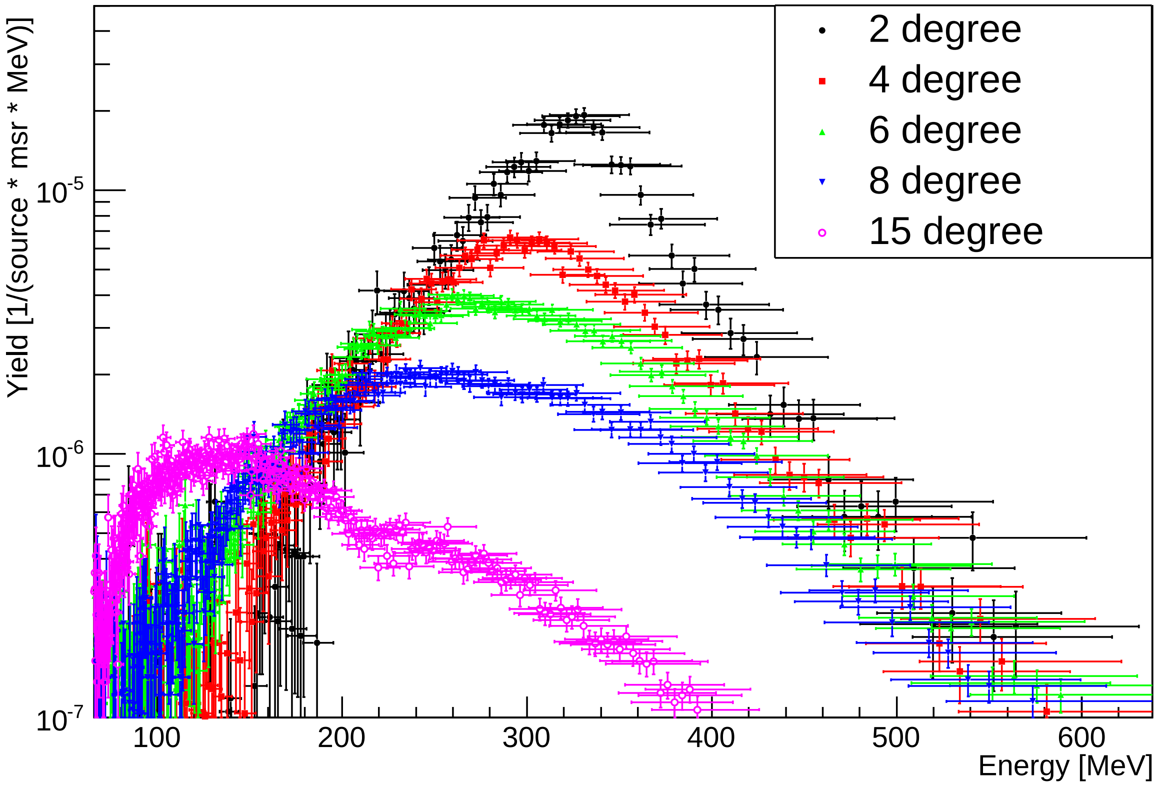

Figure 3.16.: Walk corrected energy spectra of neutrons for all angles. The vertical axis shows the number of fragments per msr and MeV normalized to the amount of primary ions impinging on the target.

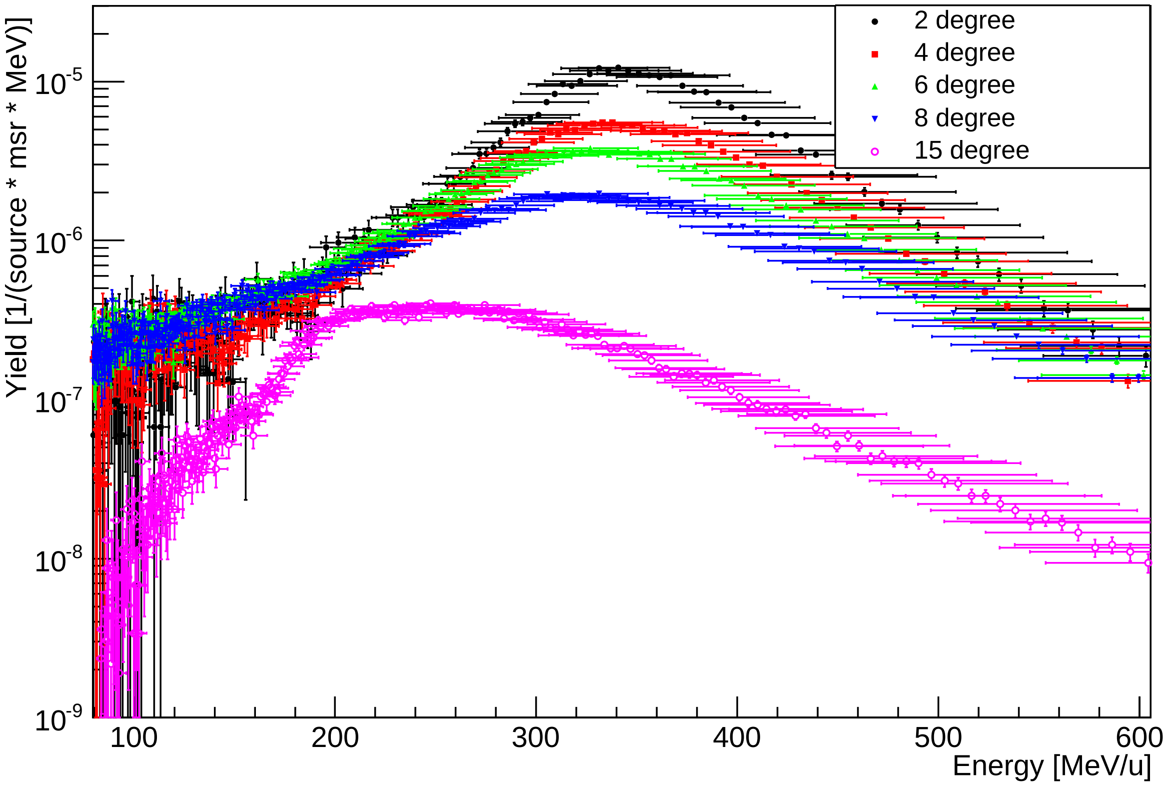

Figure 3.17.: Walk corrected energy spectra of hydrogen particles for all angles. The vertical axis shows the number of fragments per msr and MeV normalized to the amount of primary ions impinging on the target.

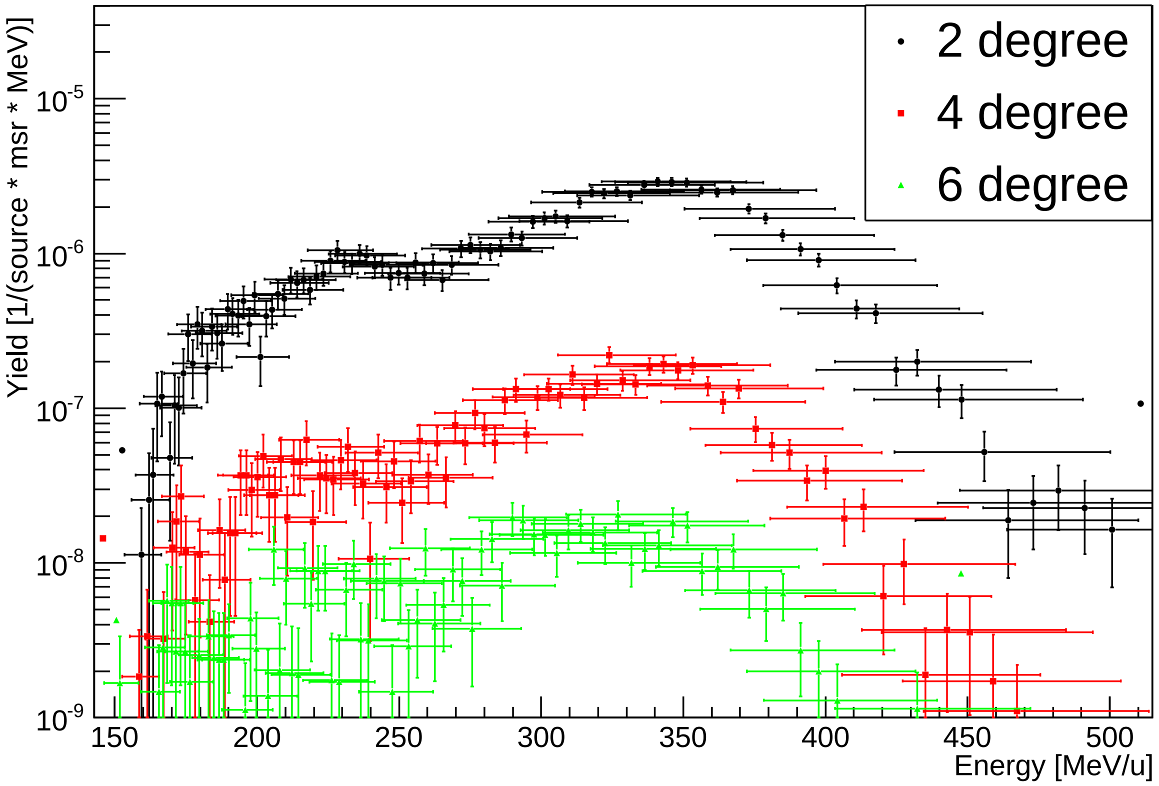

Figure 3.18.: Walk corrected energy spectra of beryllium ions for all angles. The vertical axis shows the number of fragments per msr and MeV normalized to the amount of primary ions impinging on the target.

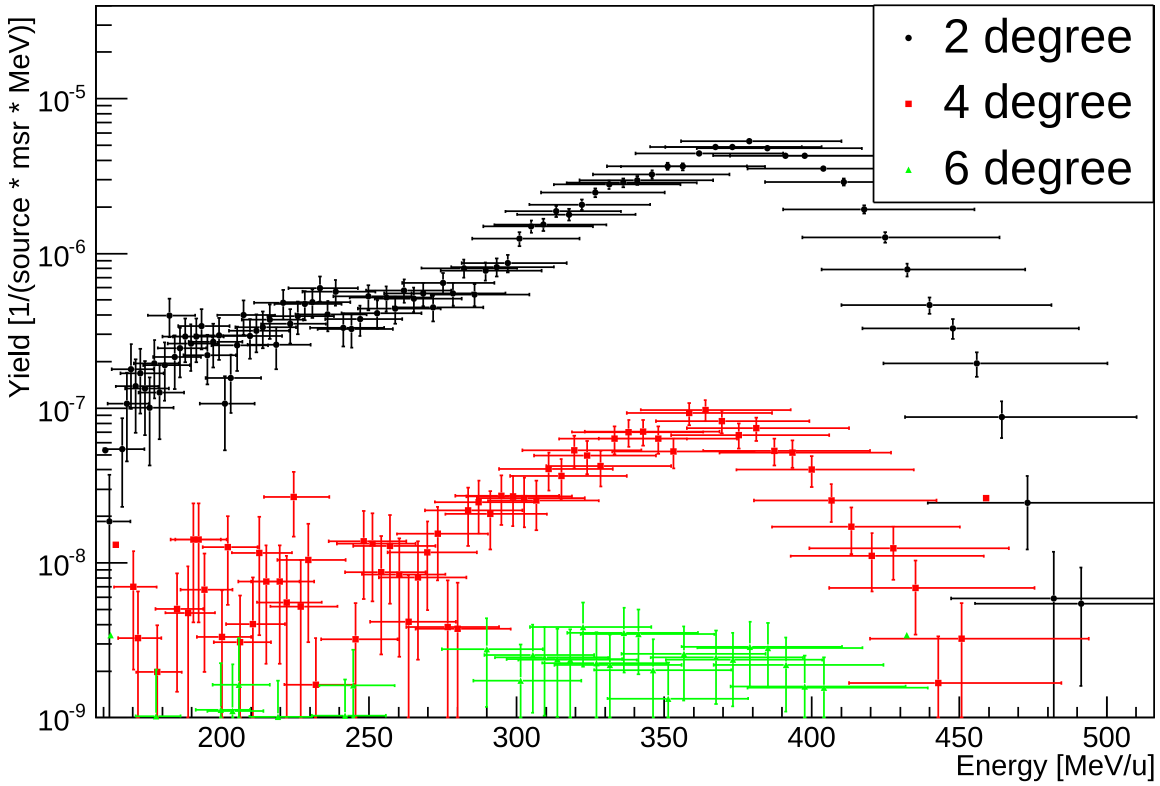

Figure 3.19.: Walk corrected energy spectra of boron ions for all angles. The vertical axis shows the number of fragments per msr and MeV normalized to the amount of primary ions impinging on the target.

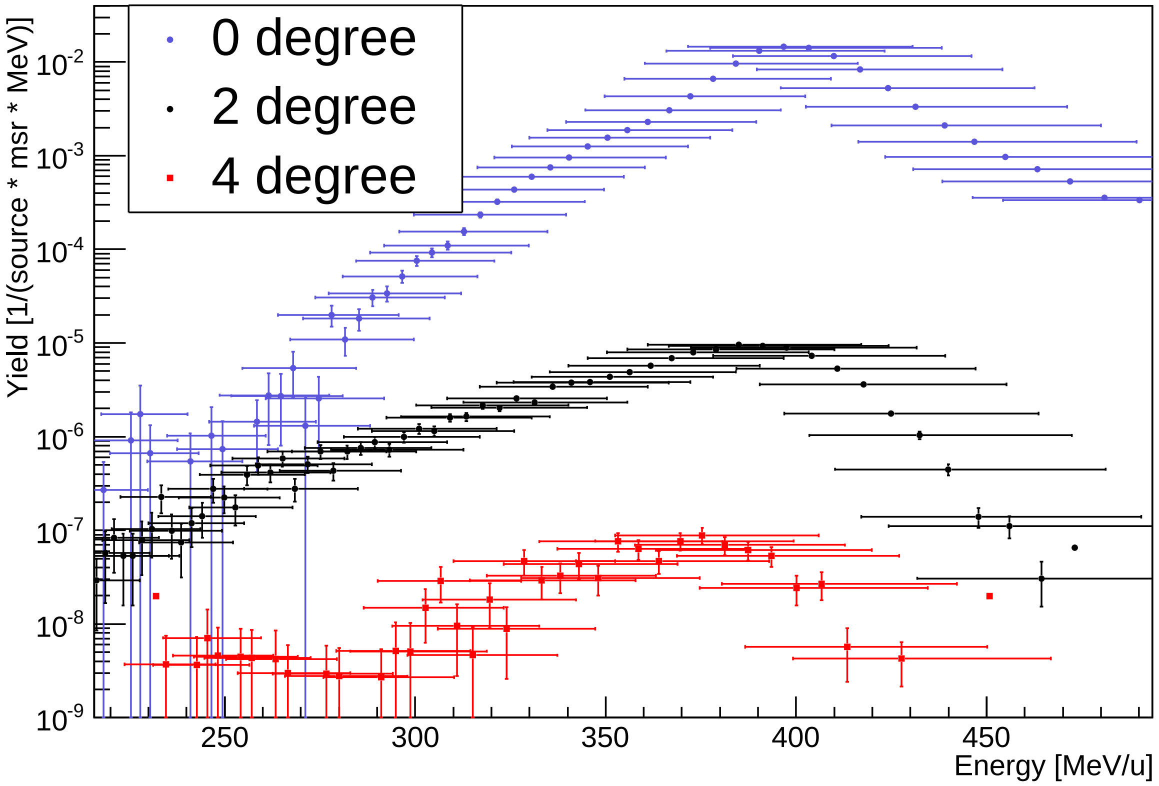

Figure 3.20.: Walk corrected energy spectra of carbon ions for all angles. The vertical axis shows the number of fragments per msr and MeV normalized to the amount of primary ions impinging on the target.

The walk corrected experimental results for all particle species (except helium and lithium particles as discussed above) are presented in figures 3.16-3.20.

Hydrogen ions and neutrons show similar characteristics at all angles as both follow similar production processes. The theoretical spectrum shape described above is well reproduced by the experimental results, which show energies up to approximately two times the incident primary beam energy could be detected. For both particle species, the main peak broadens at increasing angle and moves to lower energies. Furthermore, the distribution shape changes at increasing angle, losing its symmetry and getting increasingly tilted toward lower energies. As expected, at 2 degrees the width of the neutron energy peak is narrower than hydrogen ions because the former is not influenced by Coulomb interaction. The spectrum at 15 degrees presents a long exponential tail for high energies above 200 MeV/u for hydrogen fragments and 150 MeV/u for neutrons. Most particles detected at this angle are produced by isotropic evaporation of the target nuclei and from the overlapping zone between target and projectile (fireball). The difference in the peak observed at 15 degrees between neutrons and hydrogen particles is not expected. With increasing angle, the influence of the Coulomb interaction should increase and thus hydrogen ions should be characterized by a lower energy peak than to neutrons. A possible explanation for this behavior is that the neutron distribution peaks at a value which is clearly shifted to the lower energies between 100 and 200 MeV/u, where the estimated efficiencies of [79] and [31] show significant deviations (figure 2.13). An efficiency overestimation in this energy range is the most probable explanation for the experimental data behavior as well as the higher neutron cross sections compared to literature as discussed in section 3.1.

The predicted behavior of fragments with $Z \geq 4$ is well reproduced. The center of the energy distribution decreases with increasing angle starting at 2 degrees around the primary beam energy for boron and carbon ions and at $\approx$ 350 MeV/u for beryllium particles; the distribution width increases with increasing angle. The peak is followed by a sharp fall-off to higher energies which gets less steep at increasing angle. The strong forward momentum of the fragments is indicated by the sharp yield drop for increasing energy and increasing charge. The shift of the peak towards lower energies at increasing angles is rather small due to the high primary beam energy. The differences in shape for the carbon spectrum at 0 degrees compared to the other particles is related to the experimental setting. In order to achieve an accurate primary beam calibration it is crucial to keep all the detectors and electronic settings consistent over the complete measurement campaign. The setup was optimized for angular measurements and thus direct in-beam measurements are prone to several problems like detector saturation, etc.

Comparison with Monte Carlo simulations

The experimental energy distributions are compared to simulations from the PHITS Monte Carlo code. Figures 3.21 and 3.23 shows the comparison for hydrogen ions at 2 and 4 degrees, respectively, while the distributions measured for carbon ions at 2 degrees with and without walk correction as well as the simulation results are plotted in figure 3.22.

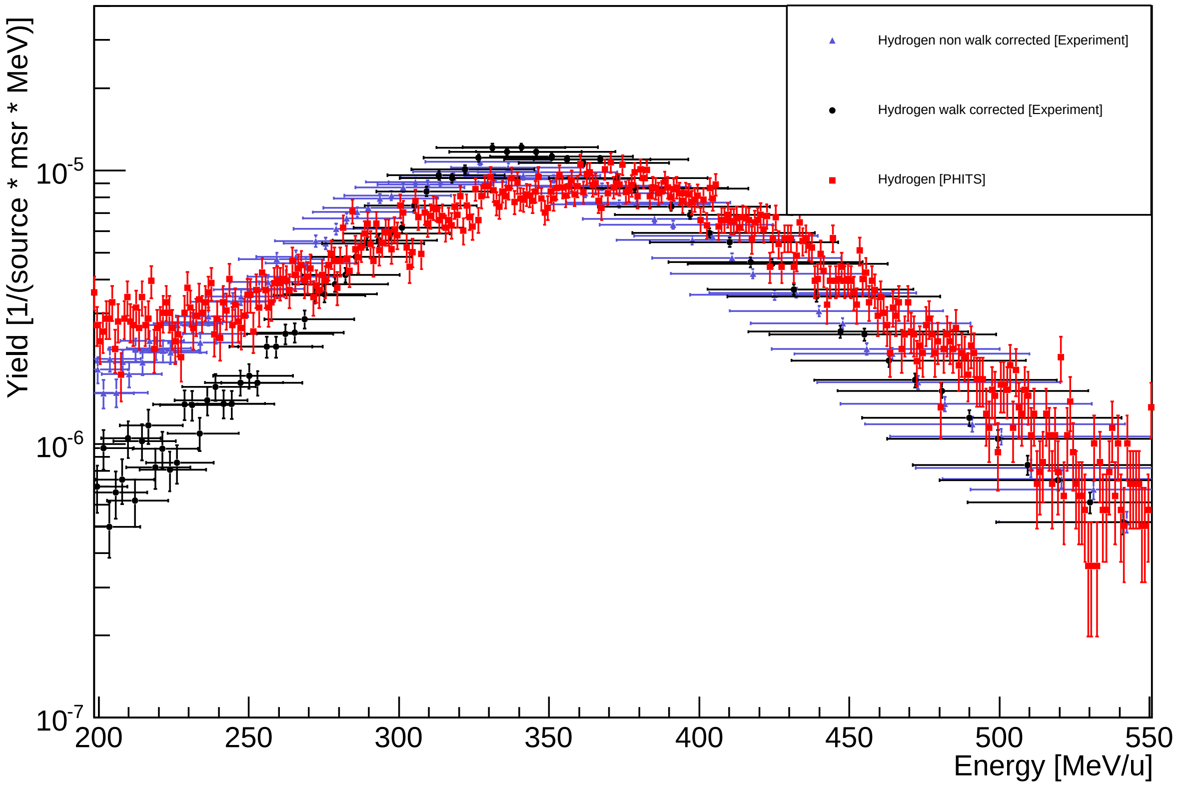

Figure 3.21.: Measured and simulated energy spectra of hydrogen ions at 2 degrees. The vertical axis shows the number of fragments per msr and MeV normalized to the amount of primary ions impinging on the target.

For hydrogen ions, the shape of the peak region and the high energy tail is reproduced fairly well even comparing the absolute yields. The low energy tail shows a maximum discrepancy in yield of more than one order of magnitude for 2 degrees and slightly less for 4 degrees. In both angles the center of the simulated energy distribution is approximately shifted by 50 MeV/u towards higher values compared to the measured ones. A small underestimation of the hydrogen ions energy is not unlikely considering the used walk correction as well as the comparably high intrinsic experimental error due to the limited time-of-flight distance. The simulation for carbon ions at 2 degrees presents a narrow sharp peak centered around 380 MeV/u with a width of approximately 5 MeV/u whereas the experimental distribution has a broader peak and a short tail at lower energies. Considering that the corrections applied as well as the calibration were performed with primary carbon ions the significant qualitative deviations in shape between simulation and experiment are unlikely to be wrong on the experimental side. Nevertheless it has to be noted that the experimental setup, as currently used, cannot measure

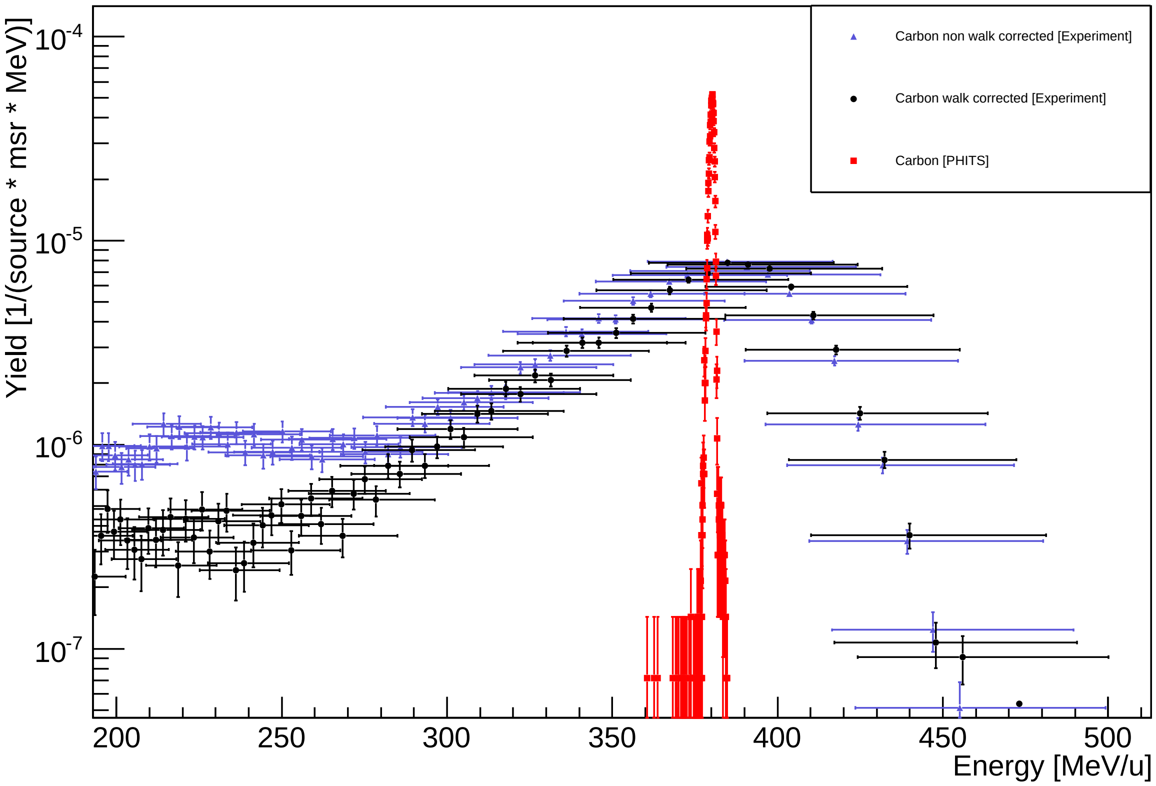

Figure 3.22.: Measured and simulated energy spectra of carbon ions at 2 degrees. The vertical axis shows the number of fragments per msr and MeV normalized to the amount of primary ions impinging on the target. The experimental spectra are reported with and without the walk correction.

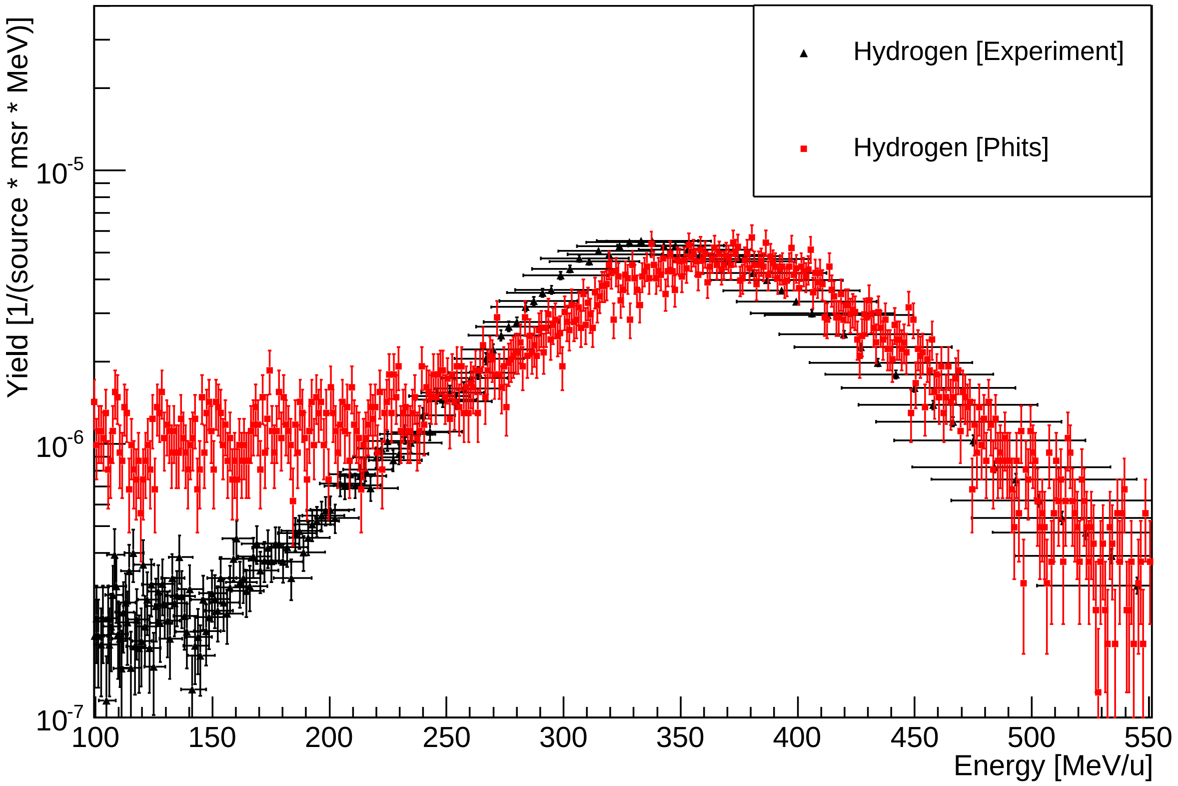

Figure 3.23.: Measured and simulated energy spectra of hydrogen ions at 4 degrees. The vertical axis shows the number of fragments per msr and MeV normalized to the amount of primary ions impinging on the target.

with an energy resolution high enough to sample the simulated peak and therefore a broader measured distribution is expected.

4 Conclusion and future outlook

The experiment described in this thesis provides a dataset of yields, angular distributions and energy spectra of fragments produced from the interaction of 400 MeV/u ^{12}C with a thin carbon target as well as a brief comparison with results from PHITS and GEANT4 Monte Carlo codes. Even if the general trend of the yields and angular distributions for most fragments is reproduced fairly well by the codes, deviations up to one order of magnitude can be observed. A qualitative comparison of the energy spectra is hindered by the high experimental error due to excessive discriminator time walk and limited time-of-flight distance. The results presented in this work can be used as base-data for unidimensional treatment planning systems or for the benchmarking of codes used in radiotherapy or space radioprotection.

Up to now, tens of thousands of patients have been irradiated in particle therapy centers around the world using a variety of treatment modalities [61]. Ongoing research includes benchmarking and optimization of different delivery techniques [41] and biological models [23] as well as the application of particle therapy for the treatment of moving targets [4] and non-cancer diseases [5].

A recent paper [49] investigated the influence of inelastic nuclear interactions on the delivered physical and RBE-weighted dose using the Monte Carlo code SHIELDHIT10A [37] for calculating the input dataset (i.e. depth-dose distributions and particle spectra) and a combination of TRiP98 [44] and LEM [18] to calculate the delivered dose and biological effects and thus estimate the RBE. The data showed that while the physical dose is significantly sensitive to changes in the inelastic nuclear cross sections, the RBE shows a relatively weak dependence, in most cases below 1% in the target volume, on the modeling of the nuclear interactions. Furthermore, the lateral penumbra of the optimized fields seems to be more influenced by electromagnetic interactions (multiple Coulomb scattering) than by nuclear fragmentation. All these results imply that the radiation quality is not strongly ruled by nuclear fragmentation, suggesting that further experiments for improving the accuracy of fragmentation cross sections might not be required. To understand these findings several things must be noted:

- TRiP98 [44] is a unidimensional treatment planning system based on experimental data and neglects certain physical processes which have an impact on the composition of the radiation field, the dose or the lateral spreading of the planned field like fragmentation of the target material or the neutrons contribution to the dose profile.
- Mairani *et al.* [50] coupled the FLUKA Monte Carlo code [22] for particle transport with the local effect model [18] to estimate the RBE and compared it to the results of

TRiP98/LEM. FLUKA is a three-dimensional transport code propagating particles event-by-event and modeling all relevant physical interaction processes. Deviations in the absorbed dose and RBE are shown especially at high penetration depths where the radiation field is dominated by light fragments.

- One advantage of heavy ion cancer treatment compared to conventional photon therapy is the possibility to irradiate target volumes close to Organ-At-Risks (OAR) (e.g. spinal chord) because of the particles favorable depth dose profile and the precise knowledge of the Bragg peak position. Nevertheless, the tail region dominated by fragmentation products deposits a non negligible dose (figure 4.1) at the lateral and distal end of the planned field and thus must be taken into account.
- The risk of secondary cancer after radiotherapy is a controversially discussed topic but there is evidence to support the hypothesis that it is beneficial to spare as much healthy tissue as possible even from receiving low amounts of dose [36]. Compared to modern photon irradiation techniques, like Intensity Modulated RadioTherapy (IMRT), the significantly lower amount of irradiation angles greatly decreases the dose delivered to the healthy tissue in the entrance channel region. Nevertheless, charged and uncharged fragments produced during the treatment will irradiate regions outside the target volume and therefore treatment planning should physically be as precise as possible in order to decrease the delivered dose to normal tissue and therefore the risk of secondary cancer or other radiation induced late health effects.

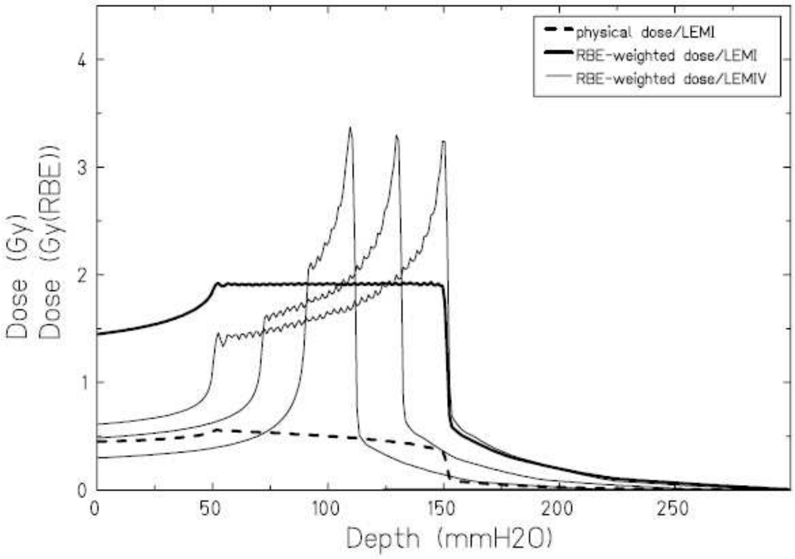

Figure 4.1.: Calculated dose tail after a spread-out Bragg peak [30].

Besides an optimization of the RBE-predictions, all aforementioned considerations support the needs of precise fragmentation cross section measurements of thin elemental targets as well as tissue-like absorbers for the assessment and improvement of the received out-field dose and benchmarking of nuclear interaction models.

In space radioprotection the omnidirectional mixed radiation field created by SPE, GCR and trapped particles and the predominant behavior of ions and neutrons covering a wide energy range must be taken into consideration. The significantly different composition of SPEs compared to the GCR as well as their differences in flux are of great importance for the assessment of the astronauts health risk. Heavy ions with energy above 100 MeV/u impinging on thin targets show a strong forward momentum and the impact of angular deflection can be considered low, whereas light charged particles and neutrons are emitted in broad angular distributions. Low energy evaporation products as high LET particles are of direct interest in radioprotection due to their high biological effectiveness (high quality factors) but fast projectile-like low LET fragments cannot be neglected either due to e.g. the potential to create further high LET particles.

A low-LET light ion while not stopping in the human body and thus with generally lower energy deposition will nevertheless deposit dose and can e.g. during a SPE, become a serious health risk. The possible combination of reparable DNS damages induced by a single proton to more complex and lethal damages leading to acute health risks. The accumulation of low-doses of e.g the GCR over a longer time period can lead to malignant tumors and diseases of e.g. the heart or digestive system.

Together with the estimation, the prevention of radiation-induced risk is a second main task in space radioprotection. The strategies applied nowadays include [16]:

- *Selection of astronauts:* genetic preconditions play a role in the individual human sensitivity to radiation [53] and therefore it might be beneficial if crew selection strategies involve predictions of the individual susceptibility to radiation.

- *Mission planning:* a low SPE probability in conjunction with a rapid alert system for SPEs are key points in minimizing possible acute health risks and a hence an important part in mission planning.

- *Food and drugs:* dietary factors [82] and radioprotective agents [52] might be able to considerably reduce acute radiation risk for e.g. SPEs as well as decrease the probability for statistical long term effects induced by radiation.

- *Shielding:* a general approach in radioprotection to reduce excessive dose is the usage of shielding materials which is unfortunately difficult in the space radiation environment. The High Z and high Energy particles (HZE) of the GCR are very penetrating and, as a general rule, the shielding effectiveness usually drops with increasing thickness due to the production of secondary fragments which can have a higher quality factor than the incident HZE particle. On the other hand, the acute effects from a SPE can be greatly mitigated with the use of a highly shielded 'storm shelter' (estimated shielding thickness > 7 g cm^{-2} aluminum) [48].

Problems regarding space radiation will be most likely solved by combining all the above mentioned strategies. Shielding properties and the related characterization of the mixed radiation field is achieved through measurements in space [13], by using particle transport codes or ground based accelerator experiments. Unidimensional transport codes like HZETRN [84] rely mainly on total yields and secondary energy spectra while three-dimensional transport codes uses double-differential fragmentation cross sections in angle and energy to calculate the particles propagation. The complex composition of e.g. the hull of a space ship and the 'dual use' of components for mechanical and shielding purposes puts additional constrains on the performances required to the transport codes and therefore on the base-data and the physical models.

Ground based experiments include the ROSSINI project [66] and the FIRST (Fragmentation of Ions Relevant Space and Therapy) experiment [60]. The ROSSINI project tests shielding properties of in-situ resources and innovative materials exposing them to 1 GeV/u heavy ion beams with a special emphasis on the creation of high energy protons and neutrons.

The FIRST experiment performed at GSI (Cave C) in 2011 aims to provide high quality double-differential fragmentation cross section measurements by combining the existing ALADIN magnet [72], the MUSIC IV TPC [72], the LAND neutron detector [7] and the TOFWALL [72] with newly designed detectors in the interaction region [1]. A breakdown of the MUSIC IV TPC during the measurement delayed the presentation of results but double-differential cross sections are expected to be published in the near future.

The need of high quality fragmentation cross section data for charged and uncharged particles shows the usefulness of the experimental setup described in this work. Based on the experience gathered in the FIRST experiment and the ROSSINI project, the setup described in this thesis was improved and optimized so to be applied to particles ranging from hydrogen to iron with energies between 100 and 1000 MeV/u without losing the benefits of comparatively small experimental setup. The main changes are described in detail in appendix C.

A Scintillation principles

The detection of ionizing radiation using the scintillation process of certain materials is one of the most versatile methods available and applied to a variety of different experimental scenarios. The scintillator properties are:

- Efficient conversion of charged particle kinetic energy into detectable light.
- Light yield proportional to deposited energy.
- Transparent to own emission wavelength (low self absorption).
- Short decay time.
- Low cost and easy to manufacture in different shapes and sizes.

No known material meets all criteria and the choice strongly depends on the specific experimental requirements. There are two commonly used types of scintillation material: fast, organic liquid- or plastic light-Z materials and rather slow inorganic high-Z materials. The density plays a major role in the scintillator selection depending on the specific radiation type of interest. The two main creation processes of scintillation light are prompt fluorescence (immediate emission of light following excitation) and phosphorescence (characterized by longer wavelengths and slower decay times).

A.1 Plastic scintillator

Plastic scintillators are commercially available in different shapes, sizes and optimized in different characteristics e.g. light output, decay time, etc.. The precise properties of a plastic scintillator depend on the host material as well as on the type of organic activator and are reported in [69] for BC-400. The energy loss of a charged particle impinging on a plastic scintillator is partially converted into fluorescent light, dissipated via lattice vibrations or heat. As a simplification it can be assumed that excitation occurs instantly and only prompt fluorescence is observed, which leads to a fast signal leading edge followed by an exponential decay.

A.2 BaF_2

BaF_2 is an inorganic scintillation material with a density of $\rho = 4.88$ g cm^{-3}. It offers a good mechanical and radiation hardness, is non-hygroscopic, chemically stable and can be produced in large volumes but is brittle [77]. It shows two emission lines: a short component with a decay time of ≈ 0.6 ns and a long component with a decay time of ≈ 630 ns. The former can be explained by core-valence luminescence. Incident radiation produces a hole in the upper core band, which recombines with a valence electron producing a photon. This corresponds to a radiative transition of an electron from a fluorine ion to a hole in a barium ion [63]. The long component is related to the emission of self-trapped excitons, where excitation can lead to a deformation of the crystal lattice resulting in the immobilization of the exciton [83]. $\mathrm{BaF_2}$ is the only known scintillator with a high atomic number($Z = 56$) in combination with a fast decay time ideal for precise timing measurements. Detailed description of the scintillation properties can be found in [68]. The low self-absorption of the material itself allows for large crystals, like the 14 cm long used in this work. The different emission bands require photomultipliers with a quartz entrance window (e.g. Thorn EMI 9821 QB) to avoid the loss of he fast component, which produces ≈ 15% of the total light yield. One major drawback of BaF_2 compared to e.g. NaI(TI) is the low total light output of ≈ 20%, leading to considerably lower energy resolution. However, in time-of-flight measurements a fast timing capability has a higher priority than a high total light output making Barium Fluoride the optimal detector material for this application.

B Simulations

B.1 Simplified geometry vs. full geometry

The building characteristics of the site where the experiment is conducted can have a non-negligible influence on the results.

The two main sources are excitation of materials exposed to the spread-out radiation field (e.g. concrete walls) created mainly by target fragments and unwanted fragmentation by material close to the beam axis (e.g. optical stand). The former results in a detector noise increase, which can be corrected most times by dedicated noise runs or stricter trigger rules. The later can induce visible and overlapping structures in the energy spectra due to the different origins of secondary fragmentation, especially for uncharged particles. Due to the more uncorrelated behavior of these events a correction is usually not possible. A schematic drawing of the cave including the concrete walls used for shielding can be found in [64]. Possible sources of unwanted fragmentation inside the experimental site are shown in picture B.1. To mark a particle as charged or uncharged the VETO signal is crucial. Particles created by secondary fragmentation can hit the BaF_2 crystal not only from forward direction, traversing the VETO, but also e.g. along the detector side. In this case particle identification will fail and the event will be wrongly marked as uncharged contaminating the spectra.

The simulation of a fully modeled experimental site increases the needed calculation time drastically. Thus, the input geometry has been simplified as much as possible without missing any important factors that might influence the results. The effects of the chosen approximations were estimated by performing simulations with both geometries at 15 degrees and comparing the results. The low number of secondary particles produced by the target itself at this angle will lead to a bigger impact of fragments created by the experimental environment and therefore can be considered as a worst case scenario. The differences in the modeled geometry are shown in figure D.2 and a comparison of the results is reported in table B.1.

The neutron yield shows a significant difference of approximately one order of magnitude, whereas the disparity for hydrogen ions is approximately a factor two. The complete absence of helium particles in the full simulation is a consequence of the lower statistics due to the dramatically increased simulation time in combination with the expected low helium production rate at the investigated angle. Based on this comparison it can be deduced that the structure of the experimental site can have a severe impact on the results and it can translated into large differences between measurements and Monte Carlo simulations. Nevertheless, the expected

Figure B.1.: The closed beamdump (left) covered by a plastic cover and the optical stand (right), used for beamline alignment are resonable canditates for backscattering as well as an additional source of fragmentation.

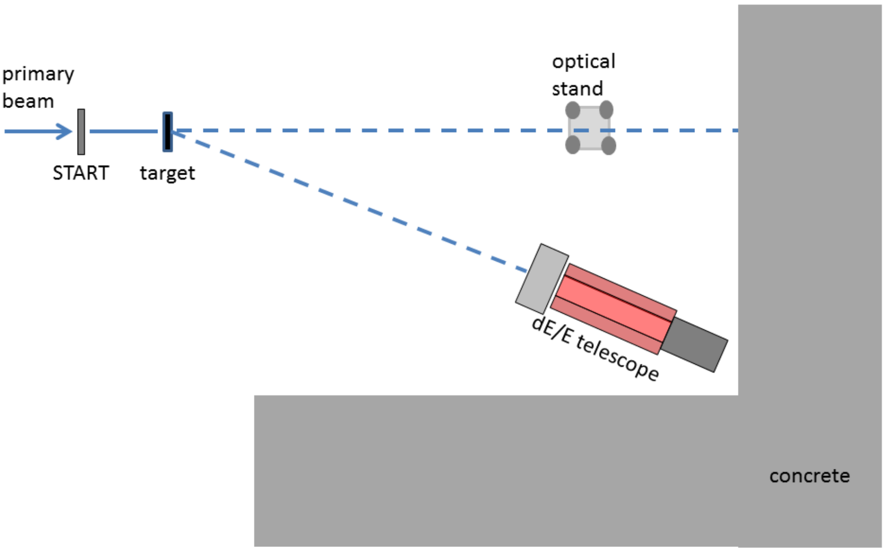

Figure B.2.: The "full" simulation geometry including part of the concrete walls and the optical stand

Type	charge neutrons	1	2
Simple	$1.99 \cdot 10^{-4}(0.7)$	$1.77 \cdot 10^{-4}(0.7)$	$2.92 \cdot 10^{-7}(18.3)$
Full	$4.05 \cdot 10^{-3}(2.4)$	$2.28 \cdot 10^{-4}(2.2)$	

Table B.1.: Comparison of the simulated fragment yields at 15 degrees in msr^{-1} $source^{-1}$ using simplified and full geometry. The relative error of the simulation is given in parentheses.

deviations for angles ≤8 degrees as well as for ions heavier than hydrogen are small due to the relatively higher fragmentation production rate of the target compared to the experimental environment.

B.2 Neutron efficiency

As stated in Section 2.4, the neutron efficiencies for the used detector geometry are not covering the entire energy range of neutrons observed in this experiment. Values reported in [79] can not be applied immediately due to different detector properties (especially its thickness). In order to calculate the efficiency scaling factors per energy, two sets of simple PHITS simulations were performed. A monoenergetic neutron beam impinged on a cylindrical target-area of BaF_2-like material. For one set of simulations the target-area thickness was set to 14 cm representing the detector used in this experiment. The other set used a target-area thickness of 25 cm representing the detector geometry used in [79]. The simulations were repeated for a wide range of neutron energies between 100 and 800 MeV. The ratio of the mean deposited energy per incident neutron is reported in table B.2 and has been used as a scaling factor for the conversion of different detector geometries.

The ratios reported in table B.2 are fitted with the following function

$$y = p_0 + p_1 * x + exp(p2 + p3 * x). \tag{B.1}$$

as shown in figure B.3. The parameter values obtained from the fit are reported in table B.3.

Based on the values reported in [79] the corresponding calculated and rescaled neutron efficiencies for this setup and for an electronic threshold of 10 MeV_{PE} are reported in table B.4.

As expected, the detector thickness plays a major role in the neutron efficiency due to the higher probability to deposit enough energy to exceed the electronic threshold.

Incident neutron energy [MeV]	14 cm BaF_2 [MeV/source]	25 cm BaF_2 [MeV/source]	Ratio
100	$2.25 \cdot 10^{-1}(0.2)$	$3.30 \cdot 10^{-1}(0.1)$	$6.82 \cdot 10^{-1}(0.3)$
150	$3.30 \cdot 10^{-1}(0.1)$	$5.06 \cdot 10^{-1}(0.1)$	$6.52 \cdot 10^{-1}(0.3)$
200	$4.28 \cdot 10^{-1}(0.2)$	$6.71 \cdot 10^{-1}(0.2)$	$6.38 \cdot 10^{-1}(0.4)$
250	$5.14 \cdot 10^{-1}(0.1)$	$8.25 \cdot 10^{-1}(0.9)$	$6.23 \cdot 10^{-1}(1.0)$
300	$5.90 \cdot 10^{-1}(0.2)$	$9.66 \cdot 10^{-1}(0.2)$	$6.11 \cdot 10^{-1}(0.4)$
350	$6.75 \cdot 10^{-1}(0.1)$	1.10(0.1)	$6.14 \cdot 10^{-1}(0.2)$
400	$7.75 \cdot 10^{-1}(0.2)$	1.25(0.1)	$6.20 \cdot 10^{-1}(0.3)$
450	$8.79 \cdot 10^{-1}(0.1)$	1.42(0.1)	$6.19 \cdot 10^{-1}(0.2)$
500	$9.91 \cdot 10^{-1}(0.2)$	1.60(0.1)	$6.19 \cdot 10^{-1}(0.3)$
550	1.10(0.1)	1.78(0.1)	$6.18 \cdot 10^{-1}(0.2)$
600	1.20(0.1)	1.96(0.1)	$6.12 \cdot 10^{-1}(0.2)$
700	1.38(0.1)	2.27(0.1)	$6.08 \cdot 10^{-1}(0.2)$
800	1.55(0.1)	2.53(0.1)	$6.13 \cdot 10^{-1}(0.2)$

Table B.2.: Simulated energy deposition of monoenergetic neutrons impinging on different BaF_2 detector geometries. The ratio of the mean deposited energy is used as a conversion factor for the neutron efficiency of a 14 cm BaF_2 and a 25 cm BaF_2. The relative error is given in parentheses.

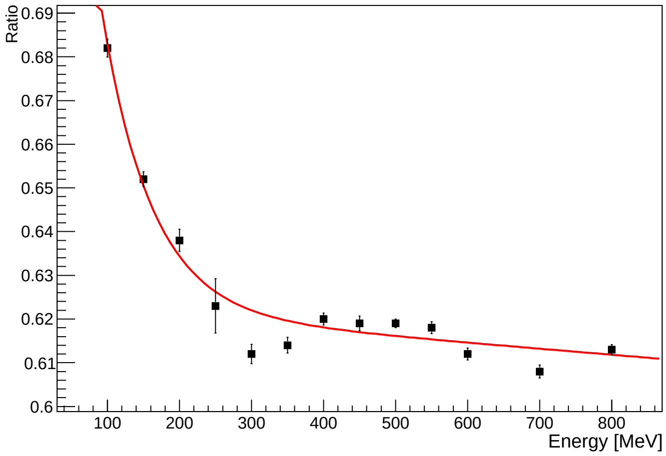

Figure B.3.: Calculated neutron efficiency conversion factors for different BaF_2 geometries.

p_0	p_1	p_2	p_3
0.62(0.3)	$-9.76 \cdot 10^{-6}(26.1)$	$-1.34(9.2)$	$-1.41 \cdot 10^{-2}(8.5)$

Table B.3.: Parameters obtained from the fit of the neutron efficiency conversion factors (table B.2) with Eq. (B.1).The relative error of the fitting parameters is given in parentheses.

neutron energy [MeV]	neutron efficiency ϵ
100	$1.46 \cdot 10^{-1}$
200	$1.30 \cdot 10^{-1}$
300	$1.33 \cdot 10^{-1}$
400	$1.35 \cdot 10^{-1}$
500	$1.48 \cdot 10^{-1}$
700	$1.66 \cdot 10^{-1}$

Table B.4.: Calculated neutron efficiencies (ϵ) based on the simulated conversion factors and the data presented in [79] and [31]

	angle [degrees]				
charge	1.8	1.9	2	2.1	2.2
1	$3.27 \cdot 10^{-3}(1.2)$	$3.15 \cdot 10^{-3}(1.4)$	$3.03 \cdot 10^{-3}(1.0)$	$2.92 \cdot 10^{-3}(0.9)$	$2.96 \cdot 10^{-3}(0.9)$
2	$2.62 \cdot 10^{-3}(1.4)$	$2.45 \cdot 10^{-3}(1.6)$	$2.38 \cdot 10^{-3}(1.1)$	$2.25 \cdot 10^{-3}(1.0)$	$2.31 \cdot 10^{-3}(0.9)$
3	$2.22 \cdot 10^{-4}(4.7)$	$2.05 \cdot 10^{-4}(5.5)$	$1.95 \cdot 10^{-4}(4.1)$	$1.93 \cdot 10^{-4}(3.4)$	$1.88 \cdot 10^{-4}(3.4)$
4	$1.12 \cdot 10^{-4}(6.6)$	$1.24 \cdot 10^{-4}(7.0)$	$1.18 \cdot 10^{-4}(5.2)$	$1.15 \cdot 10^{-4}(4.4)$	$1.17 \cdot 10^{-4}(4.3)$
5	$2.49 \cdot 10^{-4}(4.4)$	$2.24 \cdot 10^{-4}(5.2)$	$2.35 \cdot 10^{-4}(3.6)$	$2.29 \cdot 10^{-4}(3.1)$	$2.33 \cdot 10^{-4}(3.1)$
6	$1.36 \cdot 10^{-3}(1.9)$	$1.29 \cdot 10^{-3}(2.2)$	$1.26 \cdot 10^{-3}(1.6)$	$1.12 \cdot 10^{-3}(1.4)$	$1.12 \cdot 10^{-3}(1.4)$

Table B.5.: Impact of small geometrical misplacements around 2 degrees. Yield is given in msr^{-1} source^{-1}. The relative error of the simulation is given in parentheses.

B.3 Impact of small geometrical misplacements

Due to the strong forward momentum of the produced fragments slight geometrical positioning errors might have a significant impact on the observed particle yields, especially if the misplacement occurs where the angular distributions show a big gradient. This issue was investigated using a set of simulations with slightly varied detector positions. The simulated yields for small variations are presented in tables B.5 and B.6 for 2 and 4 degrees, respectively.

As expected, small angular misplacements toward lower angles will lead to a higher yield with the biggest relative deviation shown by helium particles around 2 degrees. Based on the simulation results (table 3.4) this behavior is not expected due to the steeper gradient of the hydrogen particles in the range between 0 and 2 degrees. One possible explanation could be the higher probability to create 'magic nuclei' [26] in the fragmentation process. In a study of carbon ion fragmentation in thick water targets [31] it was reported that ^{4}He as the lightest one of these was more abundant and showed a sharper peak in the forward direction than hydrogen particles. Nevertheless, this behavior cannot explain the lower abundance of helium ions compared to hydrogen particles at 0 degrees. Data reported in table B.6 in general do not follow the expected trend, due to the fact that the deviations in yield are overshadowed by statistical errors introduced by the Monte Carlo simulation itself. This behavior is stronger for

	angle [degrees]		
charge	3.9	4.0	4.1
1	$1.42 \cdot 10^{-3}(0.7)$	$1.44 \cdot 10^{-3}(0.7)$	$1.44 \cdot 10^{-3}(0.7)$
2	$7.41 \cdot 10^{-4}(1.0)$	$7.46 \cdot 10^{-4}(0.9)$	$7.41 \cdot 10^{-4}(1.0)$
3	$4.41 \cdot 10^{-5}(4.1)$	$4.53 \cdot 10^{-5}(3.8)$	$4.47 \cdot 10^{-5}(3.9)$
4	$2.02 \cdot 10^{-5}(6.1)$	$2.11 \cdot 10^{-5}(5.6)$	$2.07 \cdot 10^{-5}(5.7)$
5	$1.28 \cdot 10^{-5}(7.7)$	$1.13 \cdot 10^{-5}(7.6)$	$1.25 \cdot 10^{-5}(7.4)$
6	$6.95 \cdot 10^{-6}(10.4)$	$7.14 \cdot 10^{-6}(9.6)$	$6.37 \cdot 10^{-6}(10.3)$

Table B.6.: Impact of small geometrical misplacements around 4 degrees. Yield is given in msr^{-1} source^{-1}. The relative error of the simulation is given in parentheses.

Z≥3 particles because of their significantly lower yields and can only be overcome by increasing considerably the run-time of the simulation. In summary, small positioning errors, as reported for this experiment in table 2.1, only play a role at small angles and for light ions and are negligible for heavier ions and larger angles.

C Experimental setup - limitations and solutions

As described shortly in section 2.1 the setup used for monitoring fragmentation in the experimental site Cave A at GSI offers some advantageous characteristics but also shows several drawbacks. The main disadvantages are the lack of real-time monitoring of the primary beam position, the limited single-ion-counting capabilities of the START detector, the limited rate of the CAMAC-based DataAQuisition (DAQ) and the leading-charge analysis. During the course of this work an effort was made to eliminate the drawbacks of the experimental setup without compromising its favorable sides. The optimizations and current status of the implementations are described below.

- CMOS-tracker: The integration of a CMOS-based particle tracker consisting of several planes of MIMOSA-28 sensors is in progress and a stand-alone version has been recently tested [3]. A primary particle monitor consisting of 2 planes positioned after the START counter for monitoring the primary beam spot is planned in addition to a 4 plane fragment tracker placed close after the target (similar to [1]). The combination of beam monitor and fragment tracker offers several advantages:
  - By combining the primary particles track with that of the fragments the interaction point inside the target can be deduced.
  - By using the multiplicity and the track information given by the fragmentation tracker the amount of detector double hits can be estimated and thus the impact of the leading-charge analysis, especially for small angles, can be investigated and corrected.
  - By using the different clustering-behavior of charged particles, it might be possible to increase the charge separation abilities of the system and therefore limit the systematic error of charge separation as well as the impact of the leading-charge analysis.
- VME-based DAQ system: A VME-based DAQ system based on an CAEN V2718 optical link bridge was implemented and tested successfully at the end of 2012 [58]. In the typical configuration described in chapter 2.2 the system could handle an acquisition rate of approximately 10kHz. Even if more VME-boards are included, the new DAQ will offer an acquisition rate 10 times higher than the CAMAC-based DAQ.
- Diamond start counter: As a substitute for the plastic START counter a segmented diamond detector (Mosaic) was acquired. The detector consists of 3 x 3 sCVD diamonds with an

active area of 4.0 x 4.0 mm^2 each and offers excellent time resolution (≈ tens of ps) as well as high single ion counting capabilities [59]. Together with the high acquisition rate of the VME-based DAQ the measurement time of future experiments should be significantly reduced especially at large angles. The detector is currently being tested with several sources and tests with ion beams are planned for the near future.

Further improvements are planned or have been already implemented in the experimental site Cave A. To increase the energy resolution the time-of-flight distance has to be increased. As shown in figure C.1 this goal can be achieved by removing the front-part of the beamline, resulting in a START-Telescope distance for forward angles of about 300 cm. Due to the requirements of other users as well as the rather long rebuilding time this solution might not be always available. To reduce secondary fragmentation of the optical stand (figure. B.1) a new mechanical stand is being designed to decrease the closeness of the stand to the beam axis while still guaranteeing the original purpose of the device. Additionally a new rail system for precise alignment and positioning of targets and detectors was mounted in Cave A to further reduce positional uncertainties.

Figure C.1.: The removal of part of the beam line results in an larger time-of-flight distance and therefore better energy resolution.

D Error calculation and corrections

The experimental uncertainties of the data are discussed in the following paragraphs. Each step of the analysis is prone to different kind of errors and therefore is handled independently. Particle yields and angular distributions are most influenced by statistical errors such as dead time and the fragmentation in the experimental devices, whereas kinetic energy spectra are more strongly influenced by systematical errors introduced by the walk correction and geometrical uncertainties.

D.1 Particle yields

The main contribution to the error of the measured yields are the uncertainties on the observed number of fragments, given partially by the statistical nature of the measurement, and the systematical errors on the particle selection. The number of events for each particle type is assumed to follow a Poisson distribution and therefore the uncertainty is defined as

$$\epsilon_{counts} = \sqrt{counts}. \tag{D.1}$$

The measured counts are corrected for the dead time dt

$$counts_{dtcor} = \frac{counts}{1-dt} \tag{D.2}$$

with an uncertainty of

$$\epsilon_{counts_{dtcor}} = counts_{dtcor}\sqrt{\left(\frac{\epsilon_{dt}}{dt}\right)^2 + \left(\frac{\epsilon_{counts}}{counts}\right)^2} \tag{D.3}$$

and ϵ_{dt} given by

$$\epsilon_{dt} = dt\sqrt{\left(\frac{\epsilon_{freetrig}}{freetrig}\right)^2 + \left(\frac{\epsilon_{acctrig}}{acctrig}\right)^2} \tag{D.4}$$

where free triggers ($freetrig$) is the number of counts given by the START counter and accepted triggers ($acctrig$) the number of events recorded by the data acquisition system. The error of the corrected number of events per incident primary Φ_{cor} is then defined as

$$\epsilon_{\Phi_{cor}} = \Phi_{cor}\sqrt{\left(\frac{\epsilon_{counts_{dt_{corrected}}}}{counts_{dt_{corrected}}}\right)^2 + \left(\frac{\epsilon_{in}}{incidentions}\right)^2}. \tag{D.5}$$

Therfore $\Delta Yield_{stat}$ is given by

$$\Delta Yield_{stat} = Yield\sqrt{\left(\frac{\epsilon_{counts_{dtcor}}}{\Phi_{cor}}\right)^2 + \left(\frac{\epsilon_A}{A}\right)^2} \tag{D.6}$$

with ϵ_A given by

$$\epsilon_A = \sqrt{(\epsilon_{\Phi_{cor}}\Omega)^2 + (\epsilon_\Omega \Phi_{cor})^2}. \tag{D.7}$$

To estimate the systematical error $\Delta Yield_{sys}$, introduced by the 2d-cuts used in each dataset for particle identification, the VETO-TOF cuts were compared to VETO-BAFS cuts as well as fixed 1d-cuts performed only on the VETO with all experimental files merged. The problem of using different selection methods for particle identification is shown in figure D.1. The maximum deviation obtained file by file and charge by charge can be seen as a worst case scenario and therefore is used to approximate the systematical error. Usually the deviations between the different methods are less than 1% but can go up to 3% in some cases.

The total error on the particle yield is then defined as

$$\Delta Yield_{tot} = \sqrt{\Delta Yield_{sys}{}^2 + \Delta Yield_{stat}{}^2}. \tag{D.8}$$

D.2 Neutrons

An additional source of error for neutron yield, angular distribution and kinetic energy spectra is the correction for the detection efficiency. As described in section B.2 and section 2.4, neutron efficiency values based on data presented in [31] and [79] are used to calculate an energy-dependent efficiency curve. The uncertainty on the neutron efficiency values was included in the fitting process. The errors calculated on the fit parameters represent an estimate of the uncertainty on the neutron efficiency.

D.3 Energy

The time resolution of the complete experimental setup and hence the energy resolution can be calculated by using error propagation and is defined as

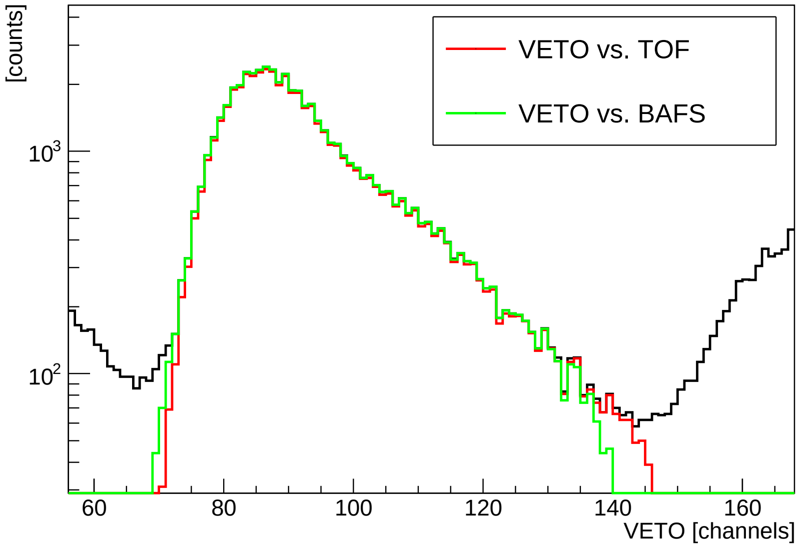

Figure D.1.: Effect of different 2d-cuts on the particle numbers of a given charge.

$$\Delta t = \sqrt{\Delta\tau^2 + \left(\frac{\Delta y}{v}\right)^2 + \left(\frac{\Delta x}{v}\right)^2} \tag{D.9}$$

where $\Delta\tau$ is the timing characteristic of the used electronics, the TDC module and the employed detectors, $\frac{\Delta y}{v}$ is defined by the different interaction points inside the target and $\frac{\Delta x}{v}$ is defined by the timing difference between particles interacting at the beginning of the detector or at its end.

Charged particles will interact continuously inside the detector and the thin target makes the influence of $\frac{\Delta x}{v}$ and $\frac{\Delta y}{v}$ negligible. The time characteristics can be assessed with the Full Width at Half Maximum (FWHM) of the calibration peaks. The latter are assumed to contain either monoenergetic primary ions or photons with constant speed of light and thus should correspond to a precise and well defined time. Every deviation of this time and therefore of the distribution width must be influenced by the electronics modules, settings or detectors.

Neutrons, not undergoing continuous Coulomb interaction inside the detector material, are prone to $\frac{\Delta x}{v}$ due to the unknown interaction point inside the detector. Assuming a Gaussian-shaped distribution and one sigma of the tdc peak the time resolution was calculated to be ±0.22 ns for the photon calibration and ±0.17 ns for the carbon ion calibration after walk correction.

Acknowledgments

I would like to thank all the people that helped me, actively or passively, during the course of this thesis.

First I would like to thank Prof. Dr. Marco Durante for the opportunity to work in the Biophysics department at GSI, for all the support, the countless beam times and for the nice atmosphere in the group. In addition I would like Prof. Dr. Joachim Enders for writing the second evaluation of this thesis.

Many thanks to all current and former members of Dieters group: Dieter, Marie, Robert, Radek, Luca, Elko and especially Marta and Chiara for all the nice scientific discussions, the general help with the thesis, the fun during nightshifts and for their never ending quest to teach me proper social skills.

Thanks to the 11.30 lunch and coffee group for all the fun and rather bold unscientific discussions (yes I am looking at you Sebi).

I would like to thank all the members of the FIRST collaboration especially: Alessio, Vincenzo, Eleuterio, Marzio, Concettina and Christian. I learnt a lot from all of you and even with all the problems concerning the MUSIC it was an amazing experience.

Special thanks to my wakeboarding and climbing friends especially to Nadine, the best climbing partner and overall friend in the known universe. You never let me down! ... Unless I was attached to a rope and asked for it, of course.

Last but not least, I would also like to extend my deepest gratitude to my family. Without their encouragement, trust and overall support this thesis would not have been possible.

Finally, I would like to thank all the people I forgot.

Curriculum vitae

Personal information

Name	Christoph Schuy
Date of Birth	24.04.1983
Location of Birth	Hadamar

Education

02/10-present	Conferral of doctorate TU Darmstadt (GSI)
14.01.2010	Diploma
08/08-09/09	Diploma thesis TU Darmstadt (GSI) Title: Intensity controlled mechanical scanning for heavy ion experiments
04/06-07/08	Main study period in physics at TU Darmstadt
10/02-03/06	Basic study period in physics at TU Darmstadt
06.06.2002	Abitur
07/93-06/02	Fürst-Johann-Ludwig school, Hadamar
07/89-06/93	Primary school, Langendernbach

Bibliography

[1] Z Abou-Haidar, C Agodi, M a G Alvarez, M Anelli, T Aumann, G Battistoni, A Bocci, T T Boehlen, A Boudard, A Brunetti, M Carpinelli, G a P Cirrone, M a Cortes-Giraldo, G Cuttone, M De Napoli, M Durante, J P Fernández-García, C Finck, M I Gallardo, B Golosio, E Iarocci, F Iazzi, G Ickert, R Introzzi, D Juliani, J Krimmer, N Kurz, M Labalme, Y Leifels, A Le Fèvre, S Leray, F Marchetto, V Monaco, M C Morone, P Oliva, A Paoloni, V Patera, L Piersanti, R Pleskac, J M Quesada, N Randazzo, F Romano, D Rossi, V Rosso, M Rousseau, R Sacchi, P Sala, A Sarti, C Schuy, A Sciubba, C Sfienti, H Simon, V Sipala, E Spiriti, L Stuttge, S Tropea, and H Younis. Performance of upstream interaction region detectors for the FIRST experiment at GSI. *J. Instrum.*, 7:1–15, 2012.

[2] S Agostinelli, J Allison, K Amako, J Apostolakis, H Araujo, P Arce, M Asai, D Axen, S Banerjee, G Barrand, F Behner, L Bellagamba, J Boudreau, L Broglia, A Brunengo, H Burkhardt, S Chauvie, J Chuma, R Chytracek, G Cooperman, G Cosmo, P Degtyarenko, A Dell'Acqua, G Depaola, D Dietrich, R Enami, A Feliciello, C Ferguson, H Fesefeldt, G Folger, F Foppiano, A Forti, S Garelli, S Giani, R Giannitrapani, D Gibin, J J Gómez Cadenas, I González, G Gracia Abril, G Greeniaus, W Greiner, V Grichine, A Grossheim, S Guatelli, P Gumplinger, R Hamatsu, K Hashimoto, H Hasui, A Heikkinen, A Howard, V Ivanchenko, A Johnson, F W Jones, J Kallenbach, N Kanaya, M Kawabata, Y Kawabata, M Kawaguti, S Kelner, P Kent, A Kimura, T Kodama, R Kokoulin, M Kossov, H Kurashige, E Lamanna, T Lampén, V Lara, V Lefebure, F Lei, M Liendl, W Lockman, F Longo, S Magni, M Maire, E Medernach, K Minamimoto, P Mora de Freitas, Y Morita, K Murakami, M Nagamatu, R Nartallo, P Nieminen, T Nishimura, K Ohtsubo, M Okamura, S O'Neale, Y Oohata, K Paech, J Perl, A Pfeiffer, M G Pia, F Ranjard, A Rybin, S Sadilov, E Di Salvo, G Santin, T Sasaki, N Savvas, Y Sawada, S Scherer, S Sei, V Sirotenko, D Smith, N Starkov, H Stoecker, J Sulkimo, M Takahata, S Tanaka, E Tcherniaev, E Safai Tehrani, M Tropeano, P Truscott, H Uno, L Urban, P Urban, M Verderi, A Walkden, W Wander, H Weber, J.P Wellisch, T Wenaus, D C Williams, D Wright, T Yamada, H Yoshida, and D Zschiesche. Geant4 - a simulation toolkit. *Nucl. Instr. Meth. A*, 506:250–303, 2003.

[3] J Baudot, G Bertolone, A Brogna, G Claus, C Colledani, R De Masi, A Dorokhov, G Dozi, W Dulinski, M Gelin, M Goffe, A Himmi, F Guilloux, K Jaaskelainen, M Koziel, F Morel, F Orsini, M Specht, I Valin, G Voutsinas, and M Winter. First test results of MIMOSA26, A fast CMOS Sensor With Integrated Zero Suppression And Digitized Output. Technical report, 2007.

[4] C Bert and M Durante. Motion in radiotherapy: particle therapy. *Phys. Med. Biol.*, 56:113–44, 2011.

[5] C Bert, R Engenhart-Cabillic, and M Durante. Particle therapy for noncancer diseases. *Med. Phys.*, 39:1716–27, 2012.

[6] H W Bertini, R T Santoro, and O W Hermann. Calculated nucleon spectra at several angles from 192-, 500-, 700-, and 900-MeV C^{12} on Fe^{56}. *Phys. Rev. C*, 14:590–5, 1976.

[7] T Blaich, T W Elze, and H Emling. A large area detector for high-energy neutrons. *Nucl. Instrum. Meth.*, 314:136–54, 1992.

[8] T T Boehlen, F Cerutti, M Dosanjh, A Ferrari, I Gudowska, A Mairani, and J M Quesada. Benchmarking nuclear models of FLUKA and GEANT4 for carbon ion therapy. *Phys. Med. Biol.*, 55:5833–47, 2010.

[9] J D Bowman. Abrasion and ablation of Heavy ions. Technical report, 1973.

[10] R Brun and F Rademakers. ROOT—an object oriented data analysis framework. *Nucl. Instrum. Meth.*, 389:81–6, 1997.

[11] G A P Cirrone and G Cuttone. Hadrontherapy: A GEANT4-based tool for proton/iontherapy studies. *Prog. Nucl. Sci. Technol.*, 2:207–12, 2011.

[12] M De Napoli, C Agodi, G Battistoni, A A Blancato, G A P Cirrone, G Cuttone, F Giacoppo, M C Morone, D Nicolosi, L Pandola, V Patera, G Raciti, E Rapisarda, F Romano, D Sardina, A Sarti, A Sciubba, V Scuderi, C Sfienti, and S Tropea. Carbon fragmentation measurements and validation of the Geant4 nuclear reaction models for hadrontherapy. *Phys. Med. Biol.*, 57:7651–71, 2012.

[13] J Dettmann, G Reitz, and G Gianfiglio. MATROSHKA—The first ESA external payload on the International Space Station. *Acta Astronaut*, 60:17–23, 2007.

[14] DIGITIZER. Plot digitizer V2.6.3. `http://plotdigitizer.sourceforge.net`, 2013.

[15] J Dudouet, D Juliani, M Labalme, D Cussol, J C Angélique, B Braunn, J Colin, Ch Finck, J M Fontbonne, H Guérin, P Henriquet, J Krimmer, M Rousseau, M G Saint-Laurent, and S Salvador. Double-differential fragmentation cross-section measurements of 95 MeV/nucleon ^{12}C beams on thin targets for hadron therapy. *Phys. Rev. C*, 88:024606–1–16, 2013.

[16] M Durante. Physical and biomedical countermeasures for space radiation risk. *Z. Med. Phys.*, 18:244–52, 2008.

[17] M Durante and F A Cucinotta. Physical basis of radiation protection in space travel. *Rev. Mod. Phys.*, 83:1245–81, 2011.

[18] T Elsaesser, M Kraemer, and M Scholz. Accuracy of the local effect model for the prediction of biologic effects of carbon ion beams in vitro and in vivo. *Int. J. Radiat. Oncol.*, 71:866–72, 2008.

[19] ESD. An introduction to camac. `http://www-esd.fnal.gov/esd/catalog/intro/introcam.htm`, 2010.

[20] H G Essel and N Kurz. The general purpose data acquisition system MBS. *IEEE Trans. Nucl. Sci.*, 47:337–9, 2000.

[21] P Ferrando, W R Webber, P Goret, J C Kish, and D A Schrier. Measurement of 12C, 16O, and 56Fe charge changing cross sections in helium at high energy, comparison with cross sections in hydrogen, and application to cosmic-ray propagation. *Phys. Rev. C*, 37:1490–501, 1988.

[22] A Ferrari, P R Sala, A Fasso, and J Ranft. FLUKA: a multi-particle transport code. Technical Report October, 2005.

[23] T Friedrich, U Scholz, T Elsaesser, M Durante, and M Scholz. Calculation of the biological effects of ion beams based on the microscopic spatial damage distribution pattern. *Int. J. Radiat. Biol.*, 88:103–7, 2012.

[24] M Giacomelli, L Sihver, and N Yasuda. Projectilelike fragment emission angles in fragmentation reactions of light heavy ions in the energy region 200 MeV / nucleon : Modeling and simulations. *Phys. Rev. C*, 69:064601–1–11, 2004.

[25] L G Glazov, P Sigmund, and A Schinner. Statistics of heavy-ion stopping. *Nucl. Instr. Meth. B*, 195(April):183–7, 2002.

[26] M Goeppert Mayer. Das Schalenmodell des Atomkerns. *Die Chemie*, 551(17):729–37, 1964.

[27] A S Goldhaber. Statistical models of fragmentation processes. *Phys. Lett.*, 53:306–8, 1974.

[28] A Golovchenko, J Skvarč, N Yasuda, M Giacomelli, S Tretyakova, R Ilić, R Bimbot, M Toulemonde, and T Murakami. Total charge-changing and partial cross-section measurements in the reactions of 110–250 MeV/nucleon 12C in carbon, paraffin, and water. *Phys. Rev. C*, 66:014609–1–8, 2002.

[29] M Golovkov. Fragmentation of 270 AMeV carbon ions in water. `http://bio.gsi.de/PUBS/1997/1997f.conf.ps`, 1997.

[30] R Gruen, T Friedrich, T Elsaesser, M Kraemer, K Zink, C P Karger, M Durante, R Engenhart-Cabillic, and M Scholz. Impact of enhancements in the local effect model (LEM) on the

predicted RBE-weighted target dose distribution in carbon ion therapy. *Phys. Med. Biol.*, 57:7261–74, 2012.

[31] K Gunzert-Marx. *Nachweis leichter Fragmente aus Schwerionenreaktionen mit einem BaF 2 – Teleskop – Detektor*. PhD thesis, 2003.

[32] K Gunzert-Marx, H Iwase, D Schardt, and R S Simon. Secondary beam fragments produced by 200 MeV/u 12 C ions in water and their dose contributions in carbon ion radiotherapy. *New J. Phys.*, 10:1–21, 2008.

[33] K Gunzert-Marx, D Schardt, R S Simon, F Gutermuth, T Radon, V Dangendorf, and R Nolte. Response of a BaF2 scintillation detector to quasi-monoenergetic fast neutrons in the range of 45 to 198MeV. *Nucl. Instr. Meth. A*, 536:146–53, 2005.

[34] T Gyo and K M Watson. Scattering of fast neutrons and protons by atomic nuclei. *Phys. Rev.*, 97:1337–43, 1955.

[35] E Haettner, M Kraemer, G Kraft, and D Schardt. Experimental study of nuclear fragmentation of 200 and 400 MeV/u C^{12} ions in water for applications in particle therapy. *Phys. Med. Biol.*, 58:8265–79, 2013.

[36] E J Hall and C Wuu. Radiation-induced second cancers: the impact of 3D-CRT and IMRT. *Int. J. Radiat. Oncol.*, 56:83–8, 2003.

[37] D C Hansen, A Luehr, R Herrmann, N Sobolevsky, and N Bassler. Recent improvements in the SHIELD-HIT code. *Int. J. Radiat. Biol.*, 88:195–9, 2012.

[38] L Heilbronn, Y Iwata, and H Iwase. Off-line correction for excessive constant-fraction-discriminator walk in neutron time-of-flight experiments. *Nucl. Instr. Meth. A*, 522:495–503, 2004.

[39] L Heilbronn, R Madey, M Elaasar, M Htun, K Frankel, W G Gong, B D Anderson, A R Baldwin, J Jiang, D Keane, M A Mcmahan, W H Rathbun, A Scott, Y Shao, J W Watson, G D Westfall, S Yennello, and W Zhang. Neutron yields from 435 MeV / nucleon Nb stopping in Nb and 272 MeV / nucleon Nb stopping in Nb and Al. *Phys. Rev. C*, 58:3451–61, 2000.

[40] Y Iwata, T Murakami, H Sato, H Iwase, T Nakamura, T. Kurosawa, L. Heilbronn, R Ronningen, K Ieki, Y Tozawa, and K Niita. Double-differential cross sections for the neutron production from heavy-ion reactions at energies E/A=290–600 MeV. *Phys. Rev. C*, 64:054609–1–10, 2001.

[41] R Kaderka. *Out-of-field dose measurements in radiotherapy*. PhD thesis, 2011.

[42] J M Kidd. Fragmentation of carbon ions at 250 MeV/nucleon. *Phys. Rev. C*, 37:2613–24, 1988.

[43] G Knoll. *Radiation Detection and Measurement*. Wiley, 3rd edition, 2000.

[44] M Kraemer. Swift ions in radiotherapy – Treatment planning with TRiP98. *Nucl. Instr. Meth. B*, 267:989–92, 2009.

[45] S Kubota, T Motobayashi, M Ogiwara, H Murakami, Y Ando, J R Gen, S Shirato, and T Murakami. RESPONSE OF BaF2 , BaF2-PLASTIC , AND BGO SCINTILLATORS TO NEUTRONS WITH ENERGIES BETWEEN 15 AND 45 MeV. *Nucl. Instr. Meth. A*, 285:436–40, 1989.

[46] C La Tessa. *Fragmentation cross sections : measurements , systematics and model development*. PhD thesis, 2007.

[47] W R Leo. *Techniques for Nuclear and Particle Physics Experiments*. Springer, 2nd edition, 1994.

[48] J R Letaw, R Silberberg, and C H Tsao. Radiation hazards on space missions outside the magnetosphere. *Adv. Space Res.*, 9:285–91, 1989.

[49] A Luehr, D C Hansen, R Teiwes, N Sobolevsky, O Jaekel, and N Bassler. The impact of modeling nuclear fragmentation on delivered dose and radiobiology in ion therapy. *Phys. Med. Biol.*, 57:5169–85, 2012.

[50] A Mairani, S Brons, F Cerutti, A Fassò, A Ferrari, M Kraemer, K Parodi, M Scholz, and F Sommerer. The FLUKA Monte Carlo code coupled with the local effect model for biological calculations in carbon ion therapy. *Phys. Med. Biol.*, 55:4273–89, 2010.

[51] S Majewski and C Zorn. *Fast scintillators for high radiation levels*. World Scientific, 1992.

[52] S McDonald and C Meyerowitz. Preliminary results of a pilot study using WR-2721 before fractionated irradiation of the head and neck to reduce salivary gland dysfunction. *Int. J. Radiat. Oncol.*, 29(4):747–54, 1994.

[53] P J McKinnon. Ataxia-telegiectasia: an inherited disorder of ionizing-radiation sensetivity in man. *Hum. Genet.*, 75:197–208, 1987.

[54] K Niita, T Sato, H Iwase, H Nose, H Nakashima, and L Sihver. PHITS—a particle and heavy ion transport code system. *Radiat. Meas.*, 41:1080–90, 2006.

[55] J W Norbury, J Miller, A M Adamczyk, L H Heilbronn, L W Townsend, S R Blattnig, R B Norman, S B Guetersloh, and C J Zeitlin. Nuclear data for space radiation. *Radiat. Meas.*, 47:315–63, 2012.

[56] R Novotny. The BaF2 Photon Spectrometer TAPS. *IEEE Trans. Nucl. Sci.*, 38:379–85, 1991.

[57] G Peilert. Physics of high-energy heavy-ion collisions. *Rep. Prog. Phys.*, 57:533–602, 1994.

[58] L Piersanti, C Schuy, C La Tessa, M Durante, Rome Sapienza, and Infn Laboratori. Development of a VME data acquisition system. *GSI Sci. Rep.*, page 479, 2012.

[59] R Pleskac. Mosaic: a new start (scvd) detector for nuclear fragmentation measurements. *GSI Sci. Rep.*, page 484, 2012.

[60] R Pleskac, Z Abou-Haidar, C Agodi, M A G Alvarez, T Aumann, G Battistoni, A Bocci, T T Boehlen, A Boudard, A Brunetti, M Carpinelli, G A P Cirrone, M a Cortes-Giraldo, G Cuttone, M De Napoli, M Durante, J P Fernández-García, C Finck, B Golosio, M I Gallardo, E Iarocci, F Iazzi, G Ickert, R Introzzi, D Juliani, J Krimmer, N Kurz, M Labalme, Y Leifels, A Le Fevre, S Leray, F Marchetto, V Monaco, M C Morone, P Oliva, A Paoloni, L Piersanti, J M Quesada, G Raciti, N Randazzo, F Romano, D Rossi, M Rousseau, R Sacchi, P Sala, A Sarti, C Scheidenberger, C Schuy, A Sciubba, C Sfienti, H Simon, V Sipala, E Spiriti, L Stuttge, S Tropea, H Younis, and V Patera. The FIRST experiment at GSI. *Nucl. Instr. Meth. A*, 678:130–8, 2012.

[61] PTCOG. PTCOG. `http://ptcog.web.psi.ch/`, 2013.

[62] C Robert, G Dedes, G Battistoni, T T Boehlen, I Buvat, F Cerutti, M P W Chin, A Ferrari, P Gueth, C Kurz, L Lestand, A Mairani, G Montarou, R Nicolini, P G Ortega, K Parodi, Y Prezado, P R Sala, D Sarrut, and E Testa. Distributions of secondary particles in proton and carbon-ion therapy: a comparison between GATE/Geant4 and FLUKA Monte Carlo codes. *Phys. Med. Biol.*, 58:2879–99, 2013.

[63] P A Rodnyi. Core-valence luminescence in scintillators. *Radiat. Meas.*, 38:343–52, 2004.

[64] S Rollet, S Agosteo, G Fehrenbacher, C Hranitzky, T Radon, and M Wind. Intercomparison of radiation protection devices in a high-energy stray neutron field, Part I: Monte Carlo simulations. *Radiat. Meas.*, 44:649–59, 2009.

[65] B Rossi. *High-Energy Particles*. Prentice-Hall, 1952.

[66] ROSSINI. ROSSINI project. `http://www.esa.it/Our_Activities/Space_Engineering/ROSSINI_for_space_radiation_protection_testing`, 2012.

[67] M Rovituso. Fragmentation of 200 and 400 MeV / u ions in bone-like materials, 2012.

[68] Saint Gobain. Barium Fluoride Scintillation Material. Technical report, 2014.

[69] Saint Gobain. Premium Plastic Scintillators. Technical report, 2014.

[70] I Schall, D Schardt, H Geissel, H Irnicha, E Kankeleit, G Kraft, A Magel, M F Mohar, G Miinzenberg, F Nickel, C Scheidenberger, and W Schwab. Charge-changing nuclear reactions of relativistic light-ion beams < Z - < 10) passing through thick absorbers *. *Nucl. Instr. Meth. B*, 117:221–34, 1996.

[71] D Schardt, T Elsaesser, and D Schulz-Ertner. Heavy-ion tumor therapy: Physical and radiobiological benefits. *Rev. Mod. Phys.*, 82:383–425, 2010.

[72] A Schuettauf and W D Kunze. Universality of spectator fragmentation at relativistic bombarding energies. *Nucl. Phys. A*, 607:457–86, 1996.

[73] D Schulz-Ertner, A Nikoghosyan, C Thilmann, T Haberer, O Jaekel, C Karger, G Kraft, M Wannenmacher, and J Debus. Results of carbon ion radiotherapy in 152 patients. *Int. J. Radiat. Oncol.*, 58:631–40, 2004.

[74] L Sihver, D Mancusi, T Sato, K Niita, H Iwase, Y Iwamoto, N Matsuda, H Nakashima, and Y Sakamoto. Recent developments and benchmarking of the PHITS code. *Adv. Space Res.*, 40:1320–31, 2007.

[75] L Sihver, T Sato, K Gustafsson, D Mancusi, H Iwase, K Niita, H Nakashima, Y Sakamoto, Y Iwamoto, and N Matsuda. An update about recent developments of the PHITS code. *Adv. Space Res.*, 45:892–9, 2010.

[76] J A Simpson. Elemental and Isotopic Composition of the Galactic Cosmic Rays. *Ann. Rev. Nucl. Part. Sci.*, 33:323–82, 1983.

[77] E Slunga, B Cederwall, E Ideguchi, A Kerek, W Klamra, J Van Der Marel, D Novak, and L Norlin. Scintillation response of BaF 2 and YAlO 3 : Ce (YAP : Ce) to energetic ions. *Nucl. Instr. Meth. A*, 469:70–6, 2001.

[78] O Tarasov and D Bazin. LISE++ : design your own spectrometer. *Nucl. Phys. A*, 746:411–4, 2004.

[79] V Wagner. Detection of relativistic neutrons by BaF2 scintillators. *Nucl. Instr. Meth. A*, 394:332–40, 1997.

[80] W R Webber. Individual charge changing fragmentation cross sections of relativistic nuclei in hzdrogen, helium, and carbon targets. *Phys. Rev. C*, 41:533–46, 1990.

[81] U Weber and G Kraft. Comparison of carbon ions versus protons. *Cancer J.*, 15:325–32, 2009.

[82] J F Weiss and M R Landauer. Protection against ionizing radiation by antioxidant nutrients and phytochemicals. *Toxicology*, 189:1–20, 2003.

[83] R T Williams. The self-trapped exciton. *J. Phys. Chem. Solids*, 51:679–716, 1990.

[84] J W Wilson, F F Badavi, and F A Cucinotta. HZETRN: description of a free-space ion and nucleon transport and shielding computer program. Technical report, 1995.

[85] C Zeitlin, S Guetersloh, L Heilbronn, J Miller, A Fukumura, Y Iwata, and T Murakami. Fragmentation cross sections of 290 and 400 MeV/nucleon C12 beams on elemental targets. *Phys. Rev. C*, 76:014911–1–21, 2007.